NASA Contractor Report 189544

LASER RAMAN DIAGNOSTICS IN SUBSONIC AND SUPERSONIC TURBULENT JET DIFFUSION FLAMES

T. S. Cheng, J. A. Wehrmeyer, and R. W. Pitz

VANDERBILT UNIVERSITY
Nashville, Tennessee

NASA

National Aeronautics and
Space Administration

Langley Research Center
Hampton, Virginia 23665-5225

SUMMARY

UV spontaneous vibrational Raman scattering combined with laser-induced predissociative fluorescence (LIPF) is developed for temperature and multi-species concentration measurements. For the first time, simultaneous measurements of temperature, major species (H_2, O_2, N_2, H_2O), and minor species (OH) concentrations are made with a "single" narrowband KrF excimer laser in subsonic and supersonic lifted turbulent hydrogen-air diffusion flames.

The UV Raman system is calibrated with a flat-flame diffusion burner operated at several known equivalence ratios from fuel-lean to fuel-rich. Temperature measurements made by the ratio of Stokes-to-anti-Stokes signals and by the ideal gas law are compared. Based on the probability density functions measured in the flat flame burner, the single-shot measurement precision for concentration and temperature measurement is 5-10%. Shot-noise from the photoelectron emission process in the photomultiplier detectors is the major contributor to the noise. Calibration constants and bandwidth factors are determined from the flat flame burner measurements and used in a data reduction program to arrive at temperature and species concentration measurements.

First UV Raman measurements are made in an axisymmetric subsonic lifted turbulent diffusion flame mixing in still air (Reynolds number of 13,600 based on the jet exit diameter). In the lift region of the turbulent flame (7 diameters downstream), the fuel and oxidizer are in a rich, premixed, and unignited condition in the center core of flame. Combustion occurs in an intermittent annular turbulent flame brush with strong finite-rate

chemistry effects resulting in nonequilibrium values of major species concentrations, OH concentration, and temperature. At 50 diameters downstream in the jet flame, the major species are in equilibrium but slow three-body recombination reactions cause superequilibrium OH concentrations and subequilibrium temperatures. Further downstream (175 diameters), superequilibrium OH radical concentrations decay toward equilibrium.

Next UV Raman measurements are made in a co-flowing axisymmetric lifted turbulent supersonic flame. A sonic jet of hydrogen mixes with a co-flowing annular jet of Mach 2 vitiated air. In the supersonic lifted flame, a little reaction occurs upstream of the flame base, due to shock wave interactions and mixing with hot vitiated air. The strong turbulent mixing and total enthalpy fluctuations lead to temperature, major species concentrations, and OH concentration with nonequilibrium values. Combustion occurs farther downstream of the lifted region. Slow three-body recombination reactions result in superequilibrium OH concentrations that depress the temperature below the equilibrium values. Near the equilibrium region, ambient air entrainment contaminates flame properties. These simultaneous measurements of temperature and multi-species concentrations allow a better understanding of the complex turbulence-chemistry interactions in supersonic flames and provide information for the input and validation of CFD models.

TABLE OF CONTENTS

LIST OF TABLES

LIST OF FIGURES

CHAPTER I

INTRODUCTION

Motivation

The development of appropriate computer models for practical combustors holds the potential for their computer-aided design with lower development costs, higher fuel efficiencies, lower emissions, and wider fuel specifications. However, to be reliable over a wide range of conditions, such models should be based upon a fundamental, quantitative understanding of the complex interaction of fuel/air mixing and chemical reaction. Considerable progress has been made in modeling the fuel/air mixing process using assumed shape probability density functions (PDFs) of two scalars (mixture fraction and progress reaction variable) to account for turbulence-chemistry interactions in both subsonic and supersonic reacting flows (Janicka and Kollmann, 1979; Chen, 1987; Villasenor et al., 1990, 1991). However, these codes have not been validated due to lack of good, quantitative, experimental data. Experiments are needed in subsonic and supersonic flames that test finite-rate chemistry models.

In turbulent diffusion flames, when a critical exit velocity is exceeded, the flame lifts off the nozzle and acquires a new configuration of stabilization in which combustion begins in an intermittent annular turbulent flame brush at a number of

nozzle diameters downstream. The physical mechanisms responsible for flame stabilization have been the subject of considerable confusion and controversy (Pitts, 1988). One of the important aspects in the lifted region is the fuel/air mixing process as well as finite-rate chemistry effects. This important aspect has received little attention in the past and has seen limited quantitative study. Simultaneous measurement of temperature, major, and minor species concentrations in subsonic lifted flames would lead to a better understanding of turbulence-chemistry interactions.

Hypersonic propulsion research has been underway for a number of years to develop advanced aerospace propulsion systems for hypersonic aircraft that are propelled by air-breathing supersonic ramjet (scramjet) engines fueled with hydrogen (Northam and Anderson, 1986). Hydrogen is the preferred fuel because of its short ignition delay time, its higher energy per unit weight, and its better cooling ability. In supersonic reacting flows, the gas residence time is comparable to the chemical reaction time. Incomplete combustion due to slow chemical kinetics may affect combustion efficiency dramatically. Simultaneous measurement of temperature and multi-species concentrations is needed not only to study turbulence-chemistry interactions but also to provide information for the input and validation of combustion models.

In both supersonic and subsonic turbulent reacting flows, the fluctuations in velocity lead to fluctuations in the scalars such as temperature and species concentrations. In subsonic turbulent flows, these fluctuations usually have

Kolmogorov time and length scales less than ~1 ms and ~1 mm, respectively. The Kolmogorov scales are even smaller in supersonic flows. In turbulent flames the measurement temporal and spatial resolutions are adequate if they are less than ~3 times the Kolmogorov scales (Goulard et al., 1976). Physical sampling probes usually lack both the spatial and temporal resolutions at these scales. Moreover, these probes produce shocks that accelerate reactions approaching the probe and make concentration measurements difficult in supersonic reacting flows. It is therefore desirable to apply a non-intrusive optical measurement system that avoids the need for physical probes in the flow and can measure temperature and species concentration with adequate temporal and spatial resolution.

The objectives of this research are: 1) to develop the ultraviolet (UV) Raman scattering and laser-induced predissociative fluorescence (LIPF) techniques for temperature and multi-species concentration measurements, and 2) to apply the developed techniques to the study of the complex turbulence-chemistry interactions in subsonic and supersonic lifted turbulent hydrogen diffusion flames. In addition, the Raman measurements will provide information for the input and validation of computational fluid dynamics (CFD) codes. Although velocity is not measured in this work, the complete simultaneous measurement of temperature, major species concentrations (H_2, O_2, N_2, H_2O), and intermediate radical (OH) can lead to a better understanding of fuel/air mixing and chemical reaction in turbulent reacting flows.

Background

To study the complex turbulence-chemistry interactions, simultaneous measurement of temperature and multi-species concentration is a desirable feature for the measurement system. Temperature can be used to calculate a reaction scalar that describes the extent of reaction. All major species concentrations can be used to calculate the local state of fuel/air mixing (i.e., mixture fraction). In addition, the measurement of combustion products (H_2O) is a primary measure of combustion efficiency. Simultaneous measurement of OH radical is an important aspect, because the presence of superequilibrium OH radical is due to slow three-body recombination reactions and it is an indication of finite-rate chemistry effects in turbulent reacting flows. Also the OH measurement can provide useful information for combustion models to predict the flame length at which OH radicals become equilibrated. In supersonic ramjet engine designs, the combustor length is required to be long enough for OH radicals to recombine and to release their chemical energy inside the combustor rather than in the exhaust plume. All of these measurements must be made with adequate temporal and spatial resolution when applied to turbulent reacting flows.

Laser-based non-intrusive techniques, with adequate temporal and spatial resolution, have been applied to measure the state properties of gases in combustion environments for many years (Eckbreth, 1988). One laser-based technique, spontaneous Raman scattering, has the capability of providing simultaneous measurements of temperature and all major species concentrations in hydrogen diffusion flames. Thus Raman scattering is chosen in this work to study turbulence-

chemistry interactions.

In subsonic turbulent flames, there have been a number of studies of turbulence-chemistry interactions. Simultaneous measurements of temperature and major species concentrations have been performed in turbulent H_2-air diffusion flames using a flashlamp-pumped dye laser operating at 488 nm (Drake et al., 1981). Comparison of the experimental results to adiabatic equilibrium calculations and differential diffusion theories showed that at low Reynolds number (Re = 1500) the primary source of the deviation from adiabatic equilibrium is differential diffusion (Bilger, 1982). Extensive measurements were compared with predictions using the conserved scalar κ - ϵ - g turbulence model (Drake et al., 1982a). Quantitative disagreement was found between the measurements and predictions at intermediate Reynolds numbers (Re = 4500 and 8500). It was concluded that the model poorly predicted the scalar fluctuations and needed to be modified. Detailed measurements, using the same Raman system, of conserved scalar PDFs have been analyzed for intermittency and conditional averages to arrive at a better understanding of turbulent mixing-chemistry interactions (Pitz and Drake, 1986) and finite-rate chemistry effects (Drake et al., 1986). Experimental results were in good agreement with second-order closure models using intermittency and conditional averaging (Chen et al., 1987).

The first saturated laser-induced fluorescence measurement of OH radicals in subsonic turbulent diffusion flames was reported by Drake et al. (1984). This OH concentration measurement was made separately from Raman measurements of

temperature and major species concentrations. Substantial superequilibrium OH was found near the jet exit due to finite-rate chemistry effects.

Finite chemical kinetic effects in a subsonic turbulent hydrogen-diluted flame were reported by Magre and Dibble (1988). Simultaneous measurements of major species, density, and temperature were performed by Raman and Rayleigh scattering techniques for three different Reynolds numbers. Departures from the limit of chemical equilibrium were achieved through increasing the rate of mixing or by decreasing the rate of chemical reaction.

Recently, Barlow et al. (1990) applied Raman scattering with laser-induced fluorescence (LIF) techniques to simultaneously measure temperature, major species, and OH radical in subsonic attached turbulent argon-diluted hydrogen flames. Collisional quenching from all major species was taken into account in the LIF measurement to obtain OH concentration. The experimental results showed that substantial superequilibrium OH (2.5-3 times greater than the peak equilibrium OH mole fraction) exists near the jet exit. Barlow et al. concluded that the ratio of the local convective time to the three-body reaction time (a Damköhler number) is the primary parameter influencing the measured OH concentration departure from the equilibrium values.

For higher exit velocity, the attached flame lifts above the nozzle exit. Liftoff characteristics for turbulent jet diffusion flames are of long-standing interest due to both the practical implications and their relationship to more fundamental aspects of combustion. Extensive experimental and theoretical studies have been made by

a number of researchers (Scholefield and Garside, 1949; Vanquickenborne and van Tiggelen, 1966; Peters and Williams, 1983; Kalghatgi, 1984; Eickhoff et al., 1984; Peters, 1984; Broadwell et al., 1984; Miake-Lye and Hammer, 1988; Pitts, 1988, 1989). However, the important aspect of turbulence-chemistry interactions has been neither quantitatively studied nor modeled in the previous works.

Instantaneous planar images of the CH_4 concentration in a lifted turbulent jet flame were reported by Schefer et al. (1988). In that report only one major species concentration was measured. Although a series of studies on flame/flow interactions and flame structures (including liftoff height and velocity measurements) in lifted propane and methane jet diffusion flames has been reported (Chen and Goss, 1989a; Chen et al., 1989; Chen and Goss, 1989b; Chen and Goss, 1990; Chen et al., 1990), no quantitative studies on the interactions of mixing and chemical reaction as well as finite-rate chemistry effects in lifted hydrogen jet diffusion flames have been accomplished. Simultaneous measurement of temperature and multi-species concentrations in a lifted hydrogen diffusion flame has been reported by Barlow et al. (1989). However, only one location was studied at the base of the lifted flame.

In previous studies of supersonic reacting flow, temperature and concentration measurements were usually made with thermocouples and other probes (Ferri, 1962; Beach, 1972). These intrusive techniques perturb the flowfield and lack both spatial and temporal resolution. The first OH concentration measurement, using an UV absorption technique, in an exhaust nozzle that simulates Mach 6 flight with subsonic combustion was performed by Lezberg and Franciscus (1963). Recently, Jarrett et

al. (1988) applied coherent anti-Stokes Raman spectroscopy (CARS) and laser Doppler velocimetry (LDV) techniques separately in a NASA Mach 2 combustor. Their results for temperature, species concentrations (O_2, N_2), and velocity were compared with a CFD model. However, the spatial resolution (~4 mm) of the CARS system was poor for analysis of supersonic reacting flows. Also only two major species concentrations were measured because of the system complexity. Therefore, in order to study the complex turbulence-chemistry interactions in supersonic reacting flows, it is more desirable to use the spontaneous Raman scattering measurement technique which has a much simpler experimental setup, a much better spatial resolution (~0.4 mm), and is capable of measuring many more species concentrations (O_2, N_2, H_2O, H_2, OH).

In review of previous studies on the subject of turbulence-chemistry interactions, little work has been done in subsonic and supersonic lifted turbulent diffusion flames. In addition, previous Raman systems used visible flashlamp-pumped dye lasers that have a number of shortcomings such as low repetition rate (1-5 Hz), poor spatial (~1 mm) and temporal (~2 μs) resolutions that make these systems inadequate for analysis of supersonic flows. The combination of Raman with conventional LIF systems have proven the ability of simultaneous measurements of temperature and multi-species concentrations, but the conventional LIF technique for OH measurement suffers from collisional quenching uncertainties and an additional laser is needed. Therefore, it is desirable to develop UV Raman scattering with LIPF techniques which have a much simpler experimental setup, a

much better spatial resolution (~0.4 mm), and no collisional quenching problem.

The usage of an ultraviolet (UV) narrowband tunable excimer laser for spontaneous Raman scattering measurements has several advantages over visible flashlamp-pumped dye lasers. A UV KrF narrowband excimer laser Raman system gives an increased signal due to the fourth power scaling of the Raman cross section with light frequency. Also the UV Raman system has the following improvements: repetition rate (~100 Hz); temporal resolution (~20 ns); and spatial resolution (~0.4 mm). In addition, KrF excimer laser-induced predissociative fluorescence (LIPF) allows quantitative minor species measurement of the OH radical because the quenching correction is unnecessary. Thus for the first time, it is shown that a "single" KrF excimer laser can measure instantaneously and simultaneously major species (H_2, O_2, N_2, H_2O), minor species (OH), and temperature in subsonic and supersonic lifted turbulent hydrogen diffusion flames.

Organization

In pursuit of these goals, Chapter II reviews the application of spontaneous Raman scattering and other laser-based techniques to measure subsonic and supersonic flows. The background theory of spontaneous Raman scattering is briefly described. In Chapter III, the UV Raman scattering system which includes a narrowband tunable KrF excimer laser, a single-grating spectrometer, a double monochromator, two light collection Cassegrain mirrors, and data acquisition system is described.

In Chapter IV, the procedures for the determination of the optimal laser wavelength and for calibration and data reduction prior to turbulent flame measurements are described. The UV Raman system is calibrated with the flat-flame "Hencken" burner operated at several known equivalence ratios from lean to rich (Hencken, 1987). Experimentally determined calibration constants and bandwidth factors are used in the data reduction program to arrive at temperature and species concentrations measurements. The local mixture fraction (a measure of fuel/air mixing) is calculated from the Raman scattering measurements of the major species concentrations for each laser shot. Experimental results from the calibration burner are compared with theoretical equilibrium curves.

In Chapter V, a lifted turbulent H_2-air diffusion flame with Re = 13600 is studied. UV Raman/LIPF measurements of temperature, major species, and OH are made in the radial direction at seven downstream locations. At each data point 1000 independent laser shots are taken. Results demonstrate that in the center core of the lifted flame base, fuel and oxidizer are rich, premixed, and unignited. Combustion occurs in an intermittent annular turbulent flame brush with strong finite-rate chemistry effects. The OH radical exists in sub-equilibrium and superequilibrium concentrations. Further downstream the superequilibrium OH radicals decay toward equilibrium concentrations through slow three-body recombination reactions.

In Chapter VI, the conventional mean and fluctuating rms profiles of mixture fraction, temperature, major species concentrations, and minor species concentration are presented for a supersonic co-flowing lifted jet diffusion flame. The UV Raman

scattering system developed at Vanderbilt University was transported to the NASA Langley Research Center where the supersonic burner is located. The supersonic flame is formed by a Mach 1 hydrogen fuel central jet mixing with an annular Mach 2 vitiated air stream. UV Raman measurements are made in the radial direction at seven downstream locations. The high speed flow of the fuel jet results in liftoff behavior which is similar to that in a subsonic lifted flame. Shock wave interactions may cause ignition in the mixing shear layer. Highly turbulent mixing affects the chemical reaction so it causes all scalars such as temperature and species concentration to depart from equilibrium values near the nozzle exit. The co-presence of H_2 and O_2, nonequilibrium OH concentration, and sub-equilibrium temperature indicate that in a supersonic flame the turbulent mixing rates are competitive with chemical reaction rates. Finally, conclusions and future efforts are summarized in Chapter VII.

CHAPTER II

LASER-BASED MEASUREMENT TECHNIQUES

Applications

For temperature and species concentration measurements three laser-based techniques have been widely used: coherent anti-Stokes Raman spectroscopy (CARS), laser-induced fluorescence (LIF), and spontaneous Raman scattering. The first two techniques, CARS and LIF, are briefly discussed. Spontaneous Raman scattering is used in this work and is described in detail.

Coherent anti-Stokes Raman spectroscopy (CARS) is a nonlinear light scattering processes applied to combustion diagnostics. With the strong signal and excellent temporal resolution (~10 ns) it has been applied to practical combustion situations such as jet engine exhausts (Eckbreth et al., 1984; Bedue et al., 1984), and internal combustion engines (Allessandretti and Violino, 1983). Simultaneous measurements of temperature and two major species concentrations (N_2 and O_2) with CARS in subsonic and supersonic turbulent reacting flows have also been reported (Antcliff et al., 1986; Jarrett et al., 1988). However, accurate measurements in turbulent flames are difficult due to poor spatial resolution (2-4 mm), highly nonlinear response, nonresonant background, and turbulence-induced steering of the multiple laser beams. Also, the data reduction is complicated and CARS generally

12

requires additional probe beams for multi-species concentration measurements.

Laser-induced fluorescence (LIF) has been widely used because of its strong signal and simplicity. It can be used to measure temperature (Laurendeau, 1988; Gross and McKenzie, 1985; Laufer and McKenzie, 1988; Fletcher and McKenzie, 1991), species concentration (Wang and Davis, 1974), turbulent mixing (Hartfield et al., 1989), and velocity (Miles et al., 1987; Hiller and Hanson, 1988; Paul et al., 1989). The LIF technique, when applied to measure species concentration in flames, is normally limited to the measurement of a single species and the signal is often dependent on collisional quenching that can vary in the flame. As a result, the LIF technique does not normally provide quantitative species concentration measurement.

Spontaneous Raman scattering can provide quantitative simultaneous measurements of temperature and species concentration with a single laser source (Lederman, 1974). Hillard et al. (1974) demonstrated the first simultaneous measurements of time-averaged temperature, density, and velocity using spontaneous Raman scattering combined with LDV in a Mach 5 low temperature wind tunnel. Although the weakness of the spontaneous Raman scattering hinders its application to practical devices, its simple experimental setup, straightforward data reduction, and potential for good spatial and temporal resolution make it attractive for the analysis of non-sooting turbulent reacting flows.

Several different lasers (e.g. ruby, argon-ion, Nd-YAG, and flashlamp-pumped dye) have been used to produce spontaneous Raman scattering. The flashlamp-pumped dye laser is the most popular one used to study turbulent flames. This laser

is tunable over the visible region and has a high pulse energy of 1 J with a ~2 μs duration and repetition rate of 1-5 Hz.

Simultaneous measurements of temperature and major species concentrations have been performed in subsonic turbulent H_2-air diffusion flames using a flashlamp-pumped dye laser by Drake et al. (1981). Extensive studies of the PDFs, the correlations of the scalar variables (temperature and species mole fractions), the differential diffusion effects, the turbulent mixing-chemistry interactions, and the finite-rate chemistry effects have been reported (Drake et al., 1982a; Pitz and Drake, 1986; Drake et al., 1986). To investigate syngas flames the same system was combined with LDV to simultaneously measure temperature, concentration, and velocity (Lapp et al., 1983).

In addition to point measurement, instantaneous two-dimensional maps of species concentration can also be obtained using the Raman scattering technique. Quantitative, two-dimensional imaging of CH_4 concentrations in a turbulent, nonreacting, CH_4 jet issuing into air was demonstrated by Long et al. (1983).

Another spontaneous Raman scattering system, using the dye laser source, has been applied to study finite chemical kinetic effects in a subsonic turbulent hydrogen-diluted flame (Magre and Dibble, 1988) and a series of hydrocarbon flames (Dibble et al., 1987; Masri et al., 1987a, b, c). This flashlamp-pumped dye laser Raman system was also combined with LDV to obtain velocity-scalar correlations (Dibble et al., 1984; Schefer and Dibble, 1985).

Recently, simultaneous measurements of temperature, major species

concentrations, and OH radicals were made in attached and lifted turbulent hydrogen flames using spontaneous Raman scattering coupled with LIF (Barlow et al., 1989, 1990). Although the OH concentration measurement suffered from the collisional quenching problem and two different lasers were used, these works demonstrated the utility of combining spontaneous Raman scattering and LIF to obtain both major and minor species.

Previous flashlamp-pumped dye laser systems have demonstrated the capability of such lasers for Raman scattering work, but these lasers have a number of shortcomings such as low repetition rate (1-5 Hz), poor spatial resolution (~1 mm), and marginal temporal (~2 μs) resolution particularly for supersonic flow. Although these lasers produce high pulse energy (1 J), the poor spatial and temporal resolution make these systems inadequate for analysis of supersonic flows due to much smaller Kolmogorov scales in these flows. The intensity of Raman scattering is approximately proportional to the first power of the laser pulse energy and the inverse fourth power of the laser wavelength. Thus, decreasing the wavelength of the laser source greatly increases the resulting Raman signal. To improve the repetition rate, the spatial resolution and the temporal resolution of a Raman system, another laser source which can produce a much higher repetition rate, a much shorter pulse length and a much shorter wavelength must be considered: the commercially available ultraviolet (UV) excimer laser.

The UV excimer lasers include both ArF (193 nm) and KrF (248 nm) versions according to excimer molecules formed in the laser. An ArF excimer is not

considered for this work, because its output wavelength resonates with the rotational lines of the Schumann-Runge absorption band of O_2 and produces strong O_2 fluorescence that obscures the O_2 Raman signal (Kobayashi et al., 1987). Also, a broadband KrF excimer laser is excluded from the consideration, since it produces OH and O_2 fluorescence that seriously interferes with the H_2O and the O_2 Raman signals, respectively (Pitz et al., 1990). A narrowband tunable KrF excimer that has a typical pulse length of ~20 ns, a linewidth of ~0.001 nm, a maximum pulse energy of ~250 mJ, and a maximum repetition rate of ~250 Hz is chosen for this work.

Background Theory

Spontaneous Raman scattering is an inelastic process in which the oscillating polarizability of the molecule modulates the scattered light, thereby leading to the appearance of two side-band frequencies. If a molecule gains energy from the incident light, the resulting lower frequency shift is termed Stokes Raman scattering; the opposite process is termed anti-Stokes Raman scattering. The elastic scattering process produces no frequency shift between incident and emitted light and is termed Rayleigh scattering. These three light scattering processes are shown in Fig. 1. For a molecule possessing zero angular momentum around the internuclear axis, the selection rules for Raman scattering are given by $\Delta v = 0, \pm 1$ and $\Delta J = 0, \pm 2$. Hence, the pure rotational Raman spectrum ($\Delta v = 0$) is characterized by a series of Stokes and anti-Stokes rotational lines. The vibrational Raman spectrum also consists of a Stokes ($\Delta v = +1$) and an anti-Stokes ($\Delta v = -1$) component, each with three branches:
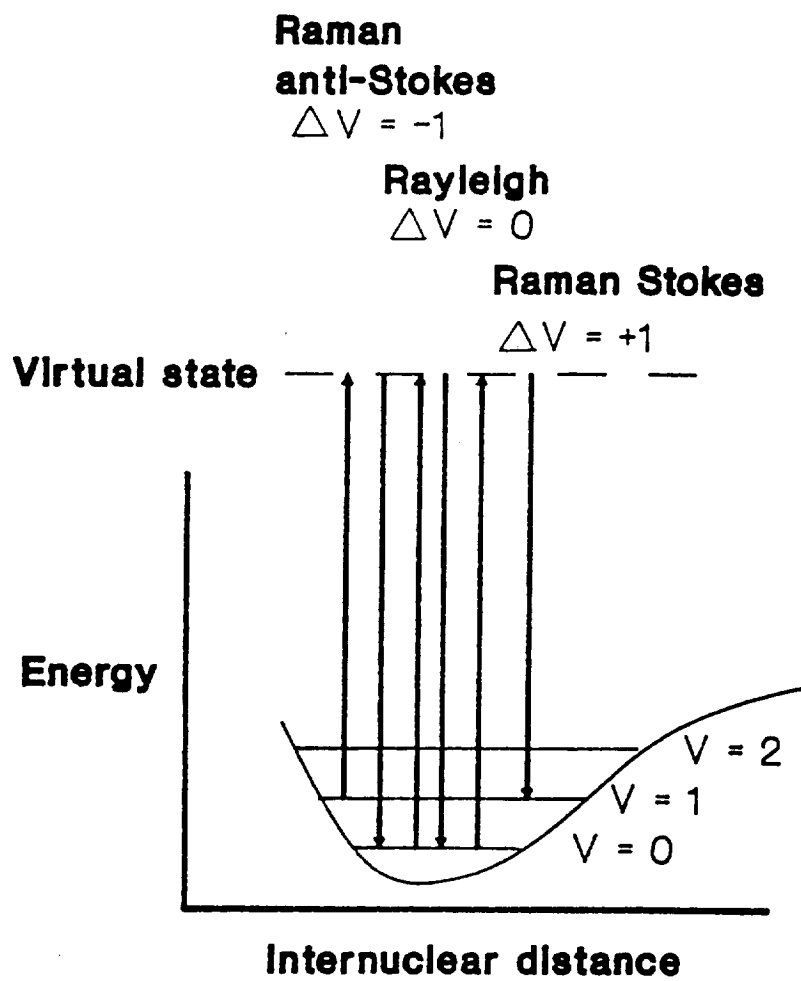
Fig. 1 Light scattering process.

O (ΔJ=-2), Q (ΔJ=0), and S (ΔJ=+2). Since the rotational lines in the Q branch are not normally resolved, this branch is usually two orders of magnitude more intense than the S and O branches, and is thus the most characteristic feature of the Stokes and anti-Stokes components of the vibrational Raman spectrum.

The intensity of the Stokes Q branch (v→v+1) is given by (Herzberg, 1950):

$$I_s(v,J) \propto \frac{g(2J+1)(v+1)v_s^4 S_J}{Q_{rot}Q_{vib}} \exp[-\frac{hcG(v,J)}{kT}] \qquad (2\text{-}1)$$

Here g is the nuclear spin degeneracy, J is the rotational quantum number, v is the vibrational quantum number, and v_s is the Stokes frequency of the Raman scattering. The molecular partition functions for rotation and vibration are Q_{rot} and Q_{vib}, respectively. Also h is Planck's constant, k is Boltzmann's constant, T is temperature, c is the speed of light, and G(v,J) is the molecular term value which includes contributions from harmonic and anharmonic oscillator terms, rigid and anharmonic rotor terms, and vibration-rotation interaction terms. The (v+1) factor is a result of Placzek's polarizability theory; the anti-Stokes (v+1→v) radiant flux is also given by Eq. (2-1) except the term (v+1) is replaced by (v). The factor S_J is the rotational line strength. For ΔJ = 0, the S_J can be calculated by (Placzek and Teller, 1933):

$$S_J = a_0(2J+1) + \frac{J(J+1)(2J+1)}{(2J-1)(2J+3)} \qquad (2\text{-}2)$$

where a_0 is a constant corresponding to the so-called trace-scattering. For high J values the influence of S_J can usually be neglected.

The intensity of the measured Stokes Raman signal can be expressed in terms of the number of detected photoelectrons and is given by (Lapp et al., 1973):

$$N_s = n\eta\, QeL\Omega\, \sigma E_L\, f(T)/(h v_s) \qquad (2\text{-}3)$$

where n is the number density of molecules, η is the efficiency of the spectrometer, Q is the quantum efficiency of the photomultiplier tube (PMT), ϵ is the optical efficiency, L is the sample length, Ω is the solid angle of the optics, σ is the Raman cross section, E_L is the laser pulse energy, and f(T) is the bandwidth factor.

All vibrational level populations contribute to the Stokes Raman signal of the gas species while only excited vibrational levels contribute to the anti-Stokes signal. Assuming an equilibrium Boltzmann distribution, a vibrational temperature measurement can be made using the ratio of the Stokes intensity, I_s, to the anti-Stokes intensity, I_a. The expression is:

$$\frac{I_s}{I_a} = C \left(\frac{v_s}{v_a}\right)^4 \exp\left(\frac{hc}{kT}\Delta G\right) \qquad (2\text{-}4)$$

where C is the ratio of the optical efficiency at the Stokes and anti-Stokes wavelength and ΔG is the Raman shift for the fundamental band (i.e., the energy level difference in cm^{-1} between the ground and first excited vibrational level). Eq. (2-4) can also be expressed in terms of the number of detected photons:

$$\frac{N_s}{N_a} = C \left(\frac{v_s}{v_a}\right)^3 \exp\left(\frac{hc}{kT}\Delta G\right) \qquad (2\text{-}5)$$

Normally, the N_2 Raman signals are used for temperature measurement because of

the omnipresence of N_2 in air-fed flames.

The background theory of Raman scattering provides a better understanding of the light scattering process and its applications for species concentration and temperature measurements. Chapter III describes the UV Raman scattering system that is used to obtain Raman scattering measurements.

CHAPTER III

UV RAMAN SCATTERING SYSTEM

Introduction

A schematic diagram of the UV Raman scattering system is shown in Fig. 2. The configuration of the experimental setup is similar for both subsonic and supersonic flame measurements. However, in the supersonic experiments due to space limitations, a 45° reflector directs the focused laser beam into the supersonic flame. A plano-convex 2000 mm focal length lens made of Corning 7940 synthetic fused silica focuses the 20 mm by 5 mm laser beam into a small sample volume. The long focal length lens prevents air breakdown in the sample volume. Scattered light from the sample volume is collected at 90° to the laser beam to improve the spatial resolution of the system and reduce Mie scattering interference (Lapp et al., 1973). A photomultiplier tube (PMT) mounted behind neutral density filters measures the relative pulse energy by sampling the light scattered by the focusing lens. Two Cassegrain mirrors collect the scattered light. The reflective optics avoids chromatic aberrations that occur in a singlet lens. A single-grating spectrometer disperses this collected light according to wavelength, allowing measurement of the various Raman and fluorescence signals. A filter that blocks out Rayleigh scattering must be used with the single grating spectrometer due to the poor stray light rejection of the
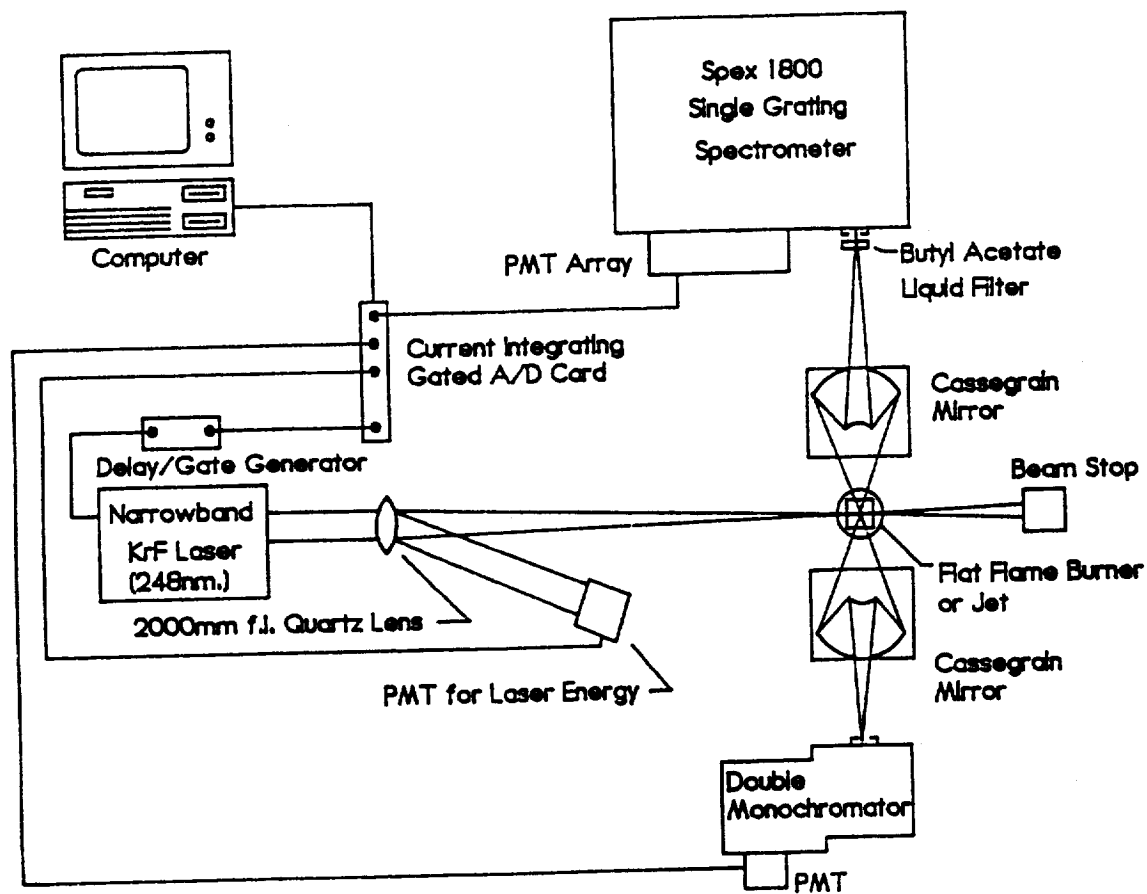
Fig. 2 Schematic diagram of UV Raman scattering system.

spectrometer. Another double monochromator which has better stray light rejection measures the N_2 anti-Stokes signal for temperature measurement. Intensities of the Raman and fluorescence signals measured by the PMTs are stored in a personal computer for data reduction and analysis.

<u>Laser Source</u>

The narrowband, injection-locked, tunable excimer laser is a Lambda-Physik EMG-160T-MSC. It has a linewidth of ~0.001 nm (0.2 cm^{-1}), a divergence of ~0.2 mrad, a pulse duration of ~20 ns, and a maximum repetition rate of 250 Hz. A schematic diagram of the narrowband laser is shown in Fig. 3. It is composed of separate oscillator and amplifier cavities. The composition of the gas mixture is: helium 1930 mbar, fluorine 120 mbar, krypton 150 mbar to make a total of 2200 mbar for the oscillator and the same amount of fluorine and krypton with 2480 mbar helium to make a total of 2750 mbar for the amplifier. The KrF excimer laser produces light around 248 nm which is in the ultraviolet (UV) region. The oscillator output is line narrowed by using dispersive prisms coupled with a grating. By rotating the grating with a micrometer, the laser wavelength is tunable from 248 to 249 nm. The grating and prisms preferentially transmit horizontally polarized output, but for Raman scattering, vertically polarized light is needed. To improve the Raman signal level, a 90° polarization rotator is placed between laser cavities. Typical pulse energy is 200 mJ with 70% vertical polarization.

The narrowband laser output is composed of narrowband emission with a
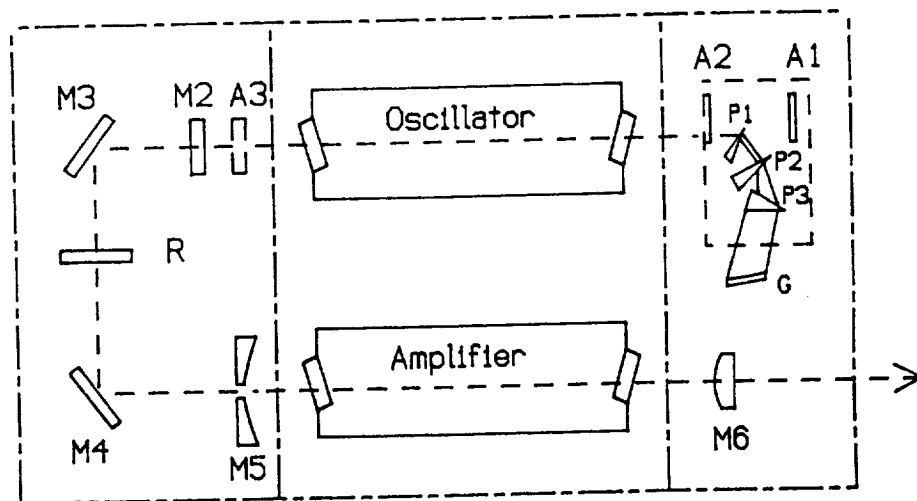
A1, A2: apertures

A3: iris aperture

M2: output coupler (R=10%)

M3, M4: deflecting mirrors (R=100%)

M5: concave mirror

M6: meniscus lens

P1, P2, P3: prisms

G: grating

R: 90°polarization rotator

Fig. 3 Schematic diagram of narrowband KrF excimer laser.

small amount of broadband emission. The ratio of the intensity of the narrowband output to the total output is termed the locking efficiency of the laser. Various factors such as the length of service of the gas mixture, cavity gas pressure, and optical alignment affect the locking efficiency. The laser locking efficiency is qualitatively monitored by examining the brightness of the fringe pattern that is produced from a factory-supplied etalon. Based on high resolution spectrometer measurements, typical laser locking efficiency under optimum conditions is about ~95%. The 95% locked emission excites the Raman scattering. The 5% unlocked broadband emission excites OH predissociative fluorescence which is used for concentration measurement and is described later.

The cross section of the focused beam is determined by placing a glass slide at the sample volume location and the laser is fired once. The damage area for the glass is examined under a microscope, and the dimensions are approximately 0.25 mm by 0.75 mm for the width and height, respectively. The length of the sample is about 0.4 mm which is determined by the opened entrance slit width of the spectrometer and the magnification ratio of the Cassegrain mirror. Thus, the sample volume of the Raman system is 0.4mm x 0.75mm x 0.25mm.

Light Collection and Measurement Devices

Scattered light for the Stokes Raman signals and fluorescences is collected and focused by a Cassegrain mirror which consists of a primary and a secondary mirror (see Fig. 4). The primary concave mirror collects the scattered light and a hole at
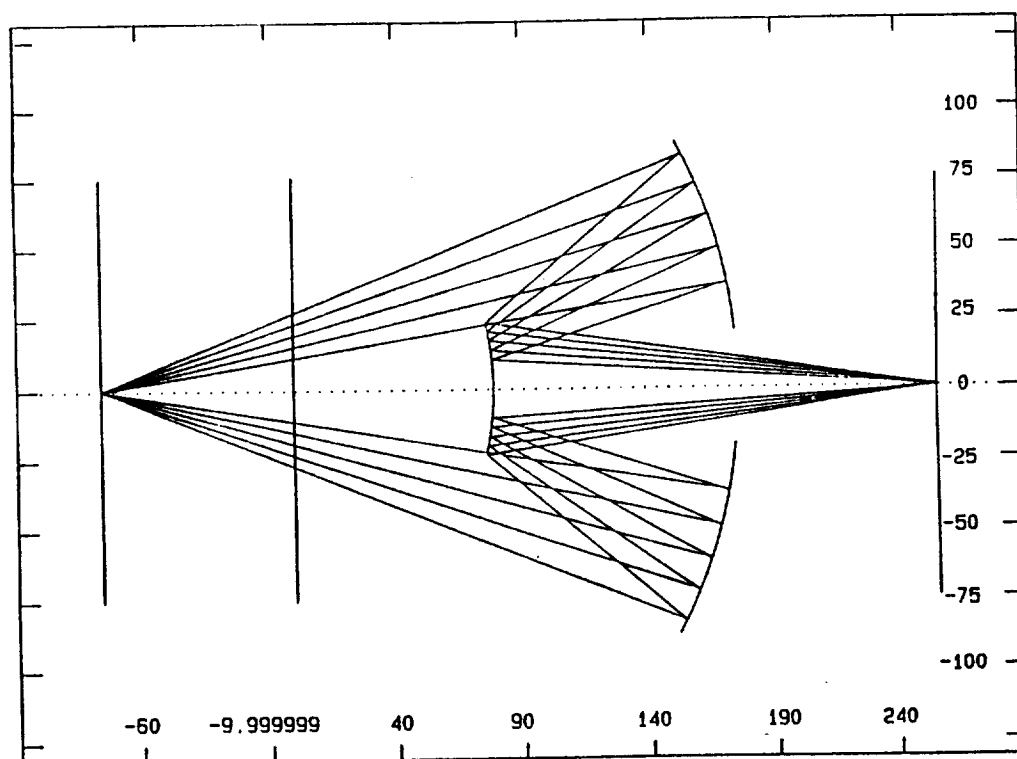
Fig. 4 Schematic diagram of Cassegrain mirror for the f/4 spectrometer. (The object and image planes are at -75.0 mm and 255.8 mm, respectively. All dimensions are in mm.)

the center transmits the light focused by the secondary convex mirror. The two mirrors are mounted on a custom machined cylinder. The primary mirror is fixed while the secondary mirror is adjustable. The Cassegrain mirrors are designed using an OPTEC II/87 PC based program (Sciopt, 1988). This program provides several functions such as paraxial analysis, real-ray analysis, and optimization for the Cassegrain optics design. Two sets of Cassegrain mirrors are designed, one for the f/7 single grating spectrometer and the other for the f/4 double monochromator. The dimensions and specifications of the Cassegrain mirrors are given in Table 1.

A long-pass liquid butyl acetate filter is placed in front of the single grating spectrometer to eliminate intense Rayleigh and Mie scattering from entering the spectrometer and causing stray light problems. The absorption coefficient of butyl acetate together with its quartz cell is measured by a spectrophotometer. The result is shown in Fig. 5. Since the spectrophotometer cannot measure absorption coefficient higher than 2.5 cm^{-1}, the curve is flat below 250 nm. Butyl acetate acts as a filter with a steep transition region from 250 to 260 nm (Alfa Products, 1988). The transmission of the filter can be calculated by $T = exp(-\alpha l)$ where α is the absorption coefficient and l is the thickness of the filter with a unit of cm. The 1 cm thick filter attenuates the intensity at 248 nm by a factor of over 1000. The O_2 Stokes Raman signal at 258 nm is reduced ~10% by the butyl acetate filter.

Since the N_2 anti-Stokes Raman signal at 235 nm is attenuated by the filter, a second spectrometer at 180° measures this signal (see Fig. 2). The second spectrometer is an Instruments SA DH-10 double monochromator which has

Table 1. Cassegrain mirror specifications.

	For f/7 spectrometer		For f/4 spectrometer	
	Calculated	Actual	Calculated	Actual
Primary mirror				
Radius of curvature	-172.5 mm	-174.7 mm	-172.5 mm	-174.7 mm
Mirror diameter	175.0 mm	200.0 mm	175.0 mm	200.0 mm
Diameter of hole	40.0 mm		40.0 mm	
Secondary mirror				
Radius of curvature	-80.3 mm	-80.0 mm	-89.0 mm	-89.1 mm
Mirror diameter	44.3 mm		44.3 mm	
Specifications				
RMS spot size in image plane	0.27 mm		0.10 mm	
Magnification	4.59	5.0	2.67	2.5
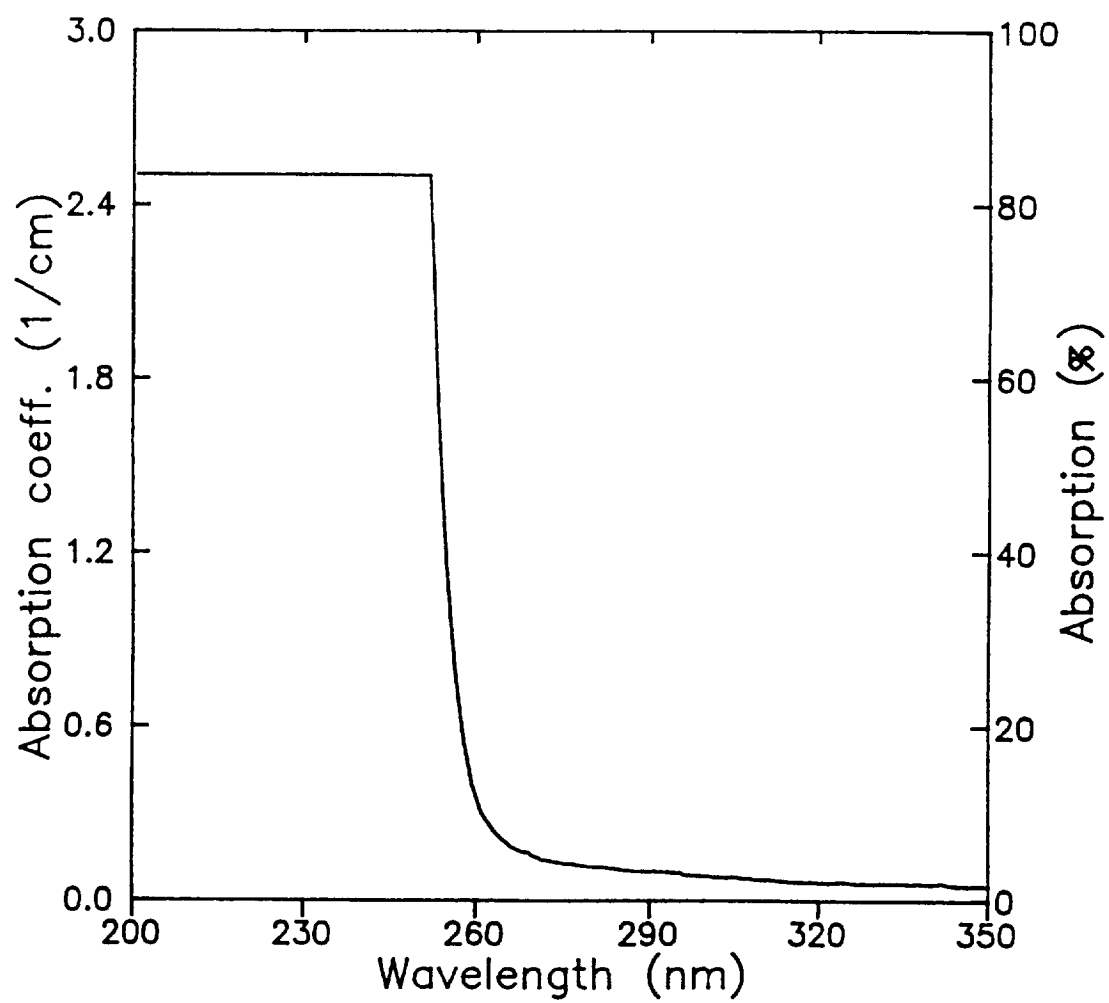
Fig. 5 Absorptance of butyl acetate filter.

excellent stray light rejection (10^{-8}) but can only measure one spectral line. With the 1200 grooves/mm grating (blazed at 250 nm), 0.833 mm entrance and exit slits (1.0 mm intermediate slit), the spectral resolution is 3.33 nm which is sufficient to reject the Rayleigh light. As a result the measured sample length is 0.33 mm which is slightly smaller than that measured by the single grating spectrometer.

The single grating spectrometer is a SPEX 1800 3/4 meter with a Czerny-Turner configuration and a polychromator. For simultaneous measurement, several slits and Hamamatsu PMTs are mounted in the polychromator housing and aligned along the exit plane of the single grating spectrometer corresponding to the Stokes Raman signals and fluorescence signals (see Fig. 6). Three R166UH PMTs detect O_2, N_2, and H_2 Raman signals. Two 1P28 PMTs measure the OH (at 297.5 nm) and O_2 (at 337.5 nm) fluorescence signals which are used to correct the residual interference on the H_2O and O_2 Raman signals, respectively. In addition to interference correction for the H_2O Raman signal, the OH fluorescence signal is used for OH concentration measurement. Due to space limitation between N_2 and H_2 PMTs, a miniature R1893 PMT is used to detect the H_2O Raman signal. These three types of PMTs are operated at different voltages to provide good linearity and dynamic range.

Currents produced by the PMTs are directed into a current integrating A/D card which is contained within a Kinetic System CAMAC standard chassis that interfaces to a personal computer. The A/D card is a LeCroy Model 2249W 11-bit integrating card with a peak capacity of 512 pC and digitizing increment of 0.25 pC.
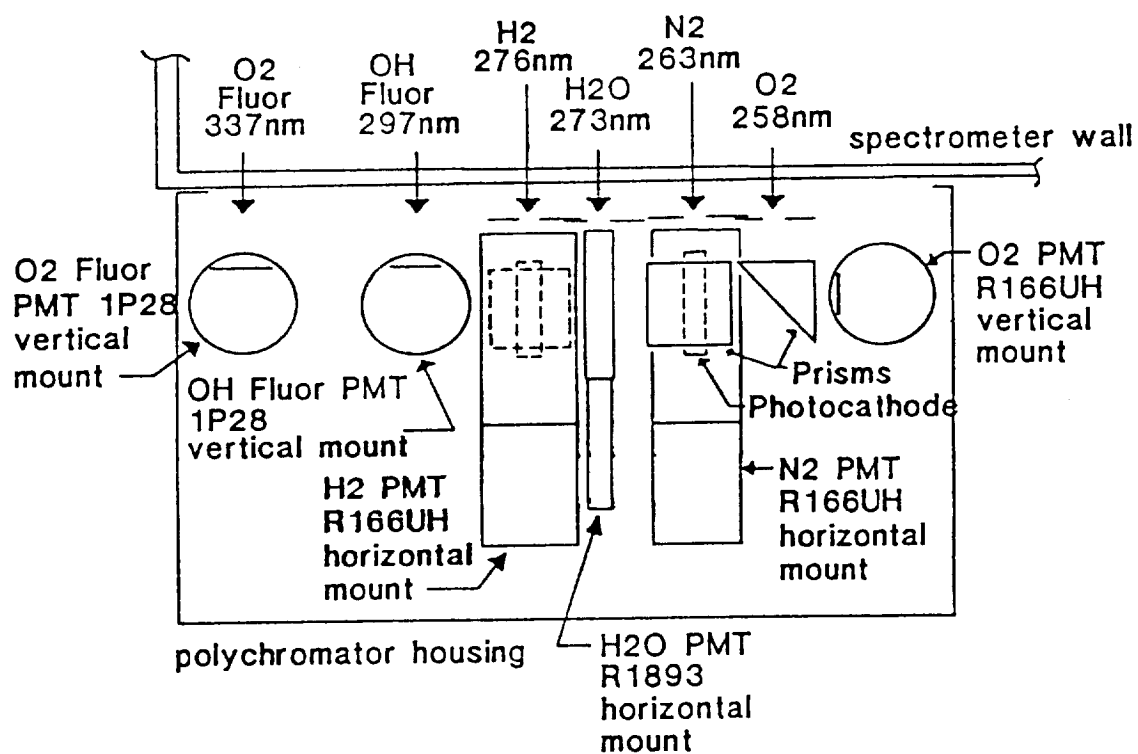
Fig. 6 PMT array diagram.

It receives a +2 volt step input and during the time that the step input is at its high value the card accepts and stores current sent by the PMT. The step has a duration of 50 ns and it is generated by a Stanford Research Systems Model 60625 delay and gate generator. The delay and gate generator receives a nonstandard voltage "sync" pulse from the laser approximately 1 μs before the laser fires, and provides the gate to the A/D card when the laser fires. An IBM/AT personal computer is employed to store and analyze the digitized data.

Prior to turbulent flame measurements, the UV Raman system is calibrated. Calibration and data reduction procedures are described in Chapter IV.

CHAPTER IV

LAMINAR FLAME MEASUREMENTS

Flat-Flame Burner

A schematic diagram of the Hencken burner cross section is shown in Fig. 7. The burner surface is 50.8 mm by 50.8 mm. It is composed of fuel tubes distributed in a honeycomb matrix. Air travels through the empty interstices and results in many tiny diffusion flamelets near the surface of the burner. Fuel and air flowrates are measured with Teledyne Hastings-Raydist hot-wire mass flowmeters. These have accuracies of 1% of full scale with a maximum flowrate of 100 lpm for air and 500 lpm for hydrogen. Thermocouple temperature measurements of the post-flame zone have shown that the heat transfer to the burner surface is a function of the total gas flowrate through the burner. In order to increase the flame temperature to close to adiabatic conditions for calibration measurement, the total gas flowrate is operated at a range of 100-240 lpm from lean to rich conditions.

Oxygen and OH Excitation Spectra

In order to reduce the fluorescence interference from O_2 and OH that respectively interferes with O_2 and H_2O Raman signals, the optimal operating wavelength of the narrowband KrF excimer laser must be determined. The tuning of the laser wavelength is accomplished by changing the grating angle (see Fig. 3).

post-flame zone

air

fuel

air

fuel

injector tube
for particle seeding
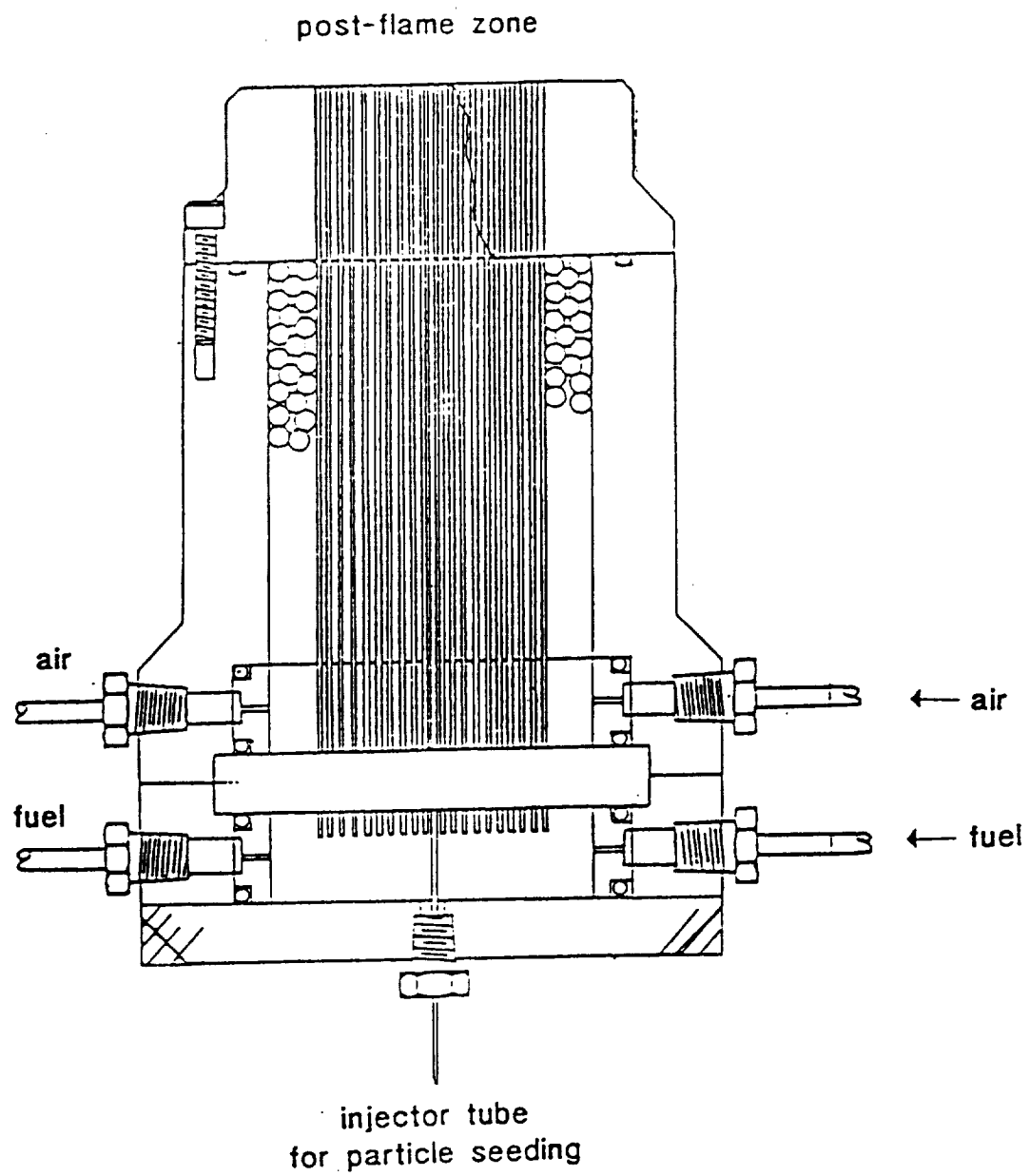
Fig. 7 Hencken burner cross section.

To obtain the O_2 excitation spectrum, the Hencken burner is operated at a fuel-lean condition ($\phi = 0.5$, T = 1600±50 K). The spectrometer is set to 256.8 nm with a 1.65 nm bandpass, a fluorescence region that interferes with the O_2 Raman Stokes signal. The laser is tuned through its locking range while monitoring the brightness of the fringe pattern from the monitor etalon to verify proper locking. The resultant O_2 excitation spectrum is shown in Fig. 8. A similar procedure is repeated for the OH excitation spectrum shown in Fig. 9. In order to produce the highest OH concentration, the Hencken burner is operated at a stoichiometric condition, near the adiabatic flame temperature of 2380 K. To measure the OH fluorescence, the spectrometer is set to 271.7 nm with a 1.4 nm bandpass.

To reduce fluorescence interference, the laser wavelength must be tuned to avoid coincidence with any OH or O_2 rotational line within the laser tuning range. Comparison of both excitation spectra indicates that an optimal wavelength is 248.623 nm (shown by the arrow in Figs. 8 and 9). This optimal wavelength allows minimal O_2 and OH fluorescence and also provides the best separation between the residual fluorescence and the Raman signals.

Calibration for Major Species Measurements

The UV Raman system is calibrated with the flat-flame Hencken burner operated at several known equivalence ratios from fuel-lean to fuel-rich ($\phi = 0$, 0.23, 0.32,...3.4). Flame temperature measurements are made with Pt/Pt-10% Rhodium (ANSI type S) thermocouple wire coated with sintered SiO_2. This coating is to
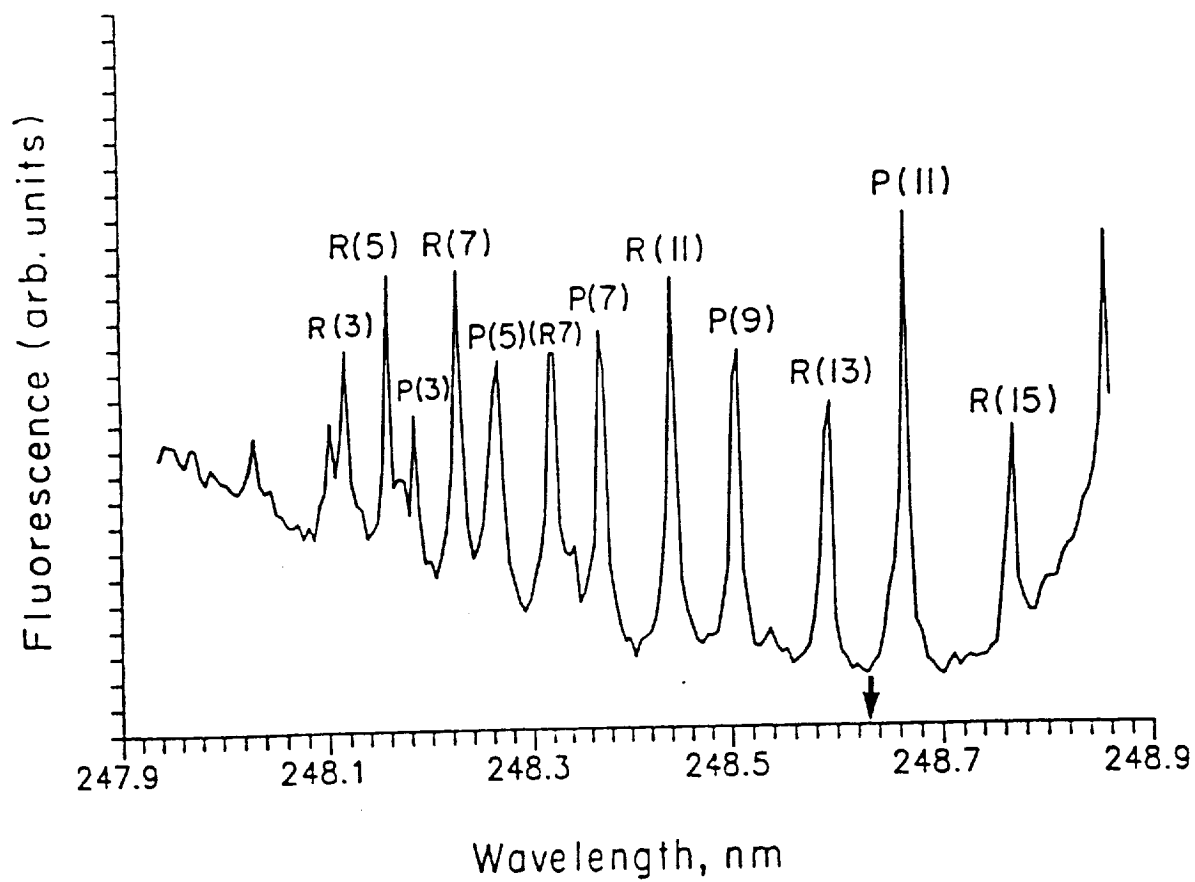
Fig. 8 O_2 fluorescence excitation spectrum.
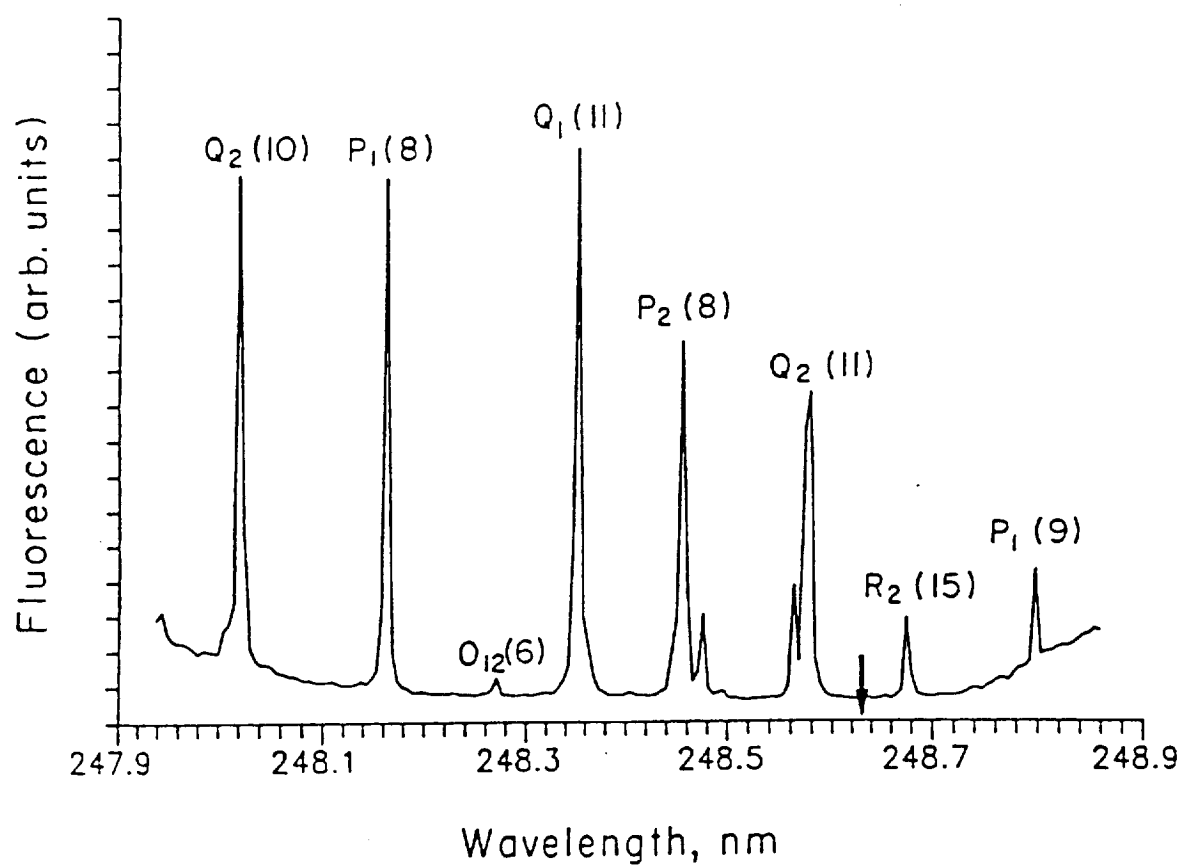
Fig. 9 OH fluorescence excitation spectrum.

eliminate catalytic heating effects on the platinum wire itself. At low burner flowrates, radiation corrected temperature measurements indicate that flame temperatures are well below the adiabatic equilibrium values due to heat transfer to the burner surface. In order to obtain higher temperatures for system calibration, the total flowrates to the burner are operated at a range of 100-240 lpm from lean to rich conditions. At these high flowrates, the largest heat loss is under rich conditions (e.g., 140 K temperature reduction at $\phi = 2.1$).

As the flame temperature is often higher than the thermocouple melting temperature (1723 K), a spectral fitting method is used to arrive at temperature measurements. A short N_2 Stokes Raman spectrum is recorded from each flame condition and compared with the theoretical spectrum which is calculated from Eq. (2-1) modified to include resonant enhancement of the Raman signal (Wehrmeyer, 1990). This method is tested against the thermocouple measured temperature below 1700 K, and the agreement is within ±50 K for those flame temperatures.

Two spectra are demonstrated in Fig. 10 for low and high temperatures. Fig. 10a shows the best fitting temperature is 1050 K with the uncertainty of ±50 K where the radiation corrected thermocouple temperature is 1000±20K. For the higher temperature stoichiometric flame (2380 K) the uncertainty increases to about ±100 K due to decreased N_2 concentration in flame (Fig. 10b). The spectral fitting method is an excellent tool for laminar flame temperature measurement especially for flame temperatures higher than the thermocouple melting temperature. This method is employed for all the calibration temperature measurements.
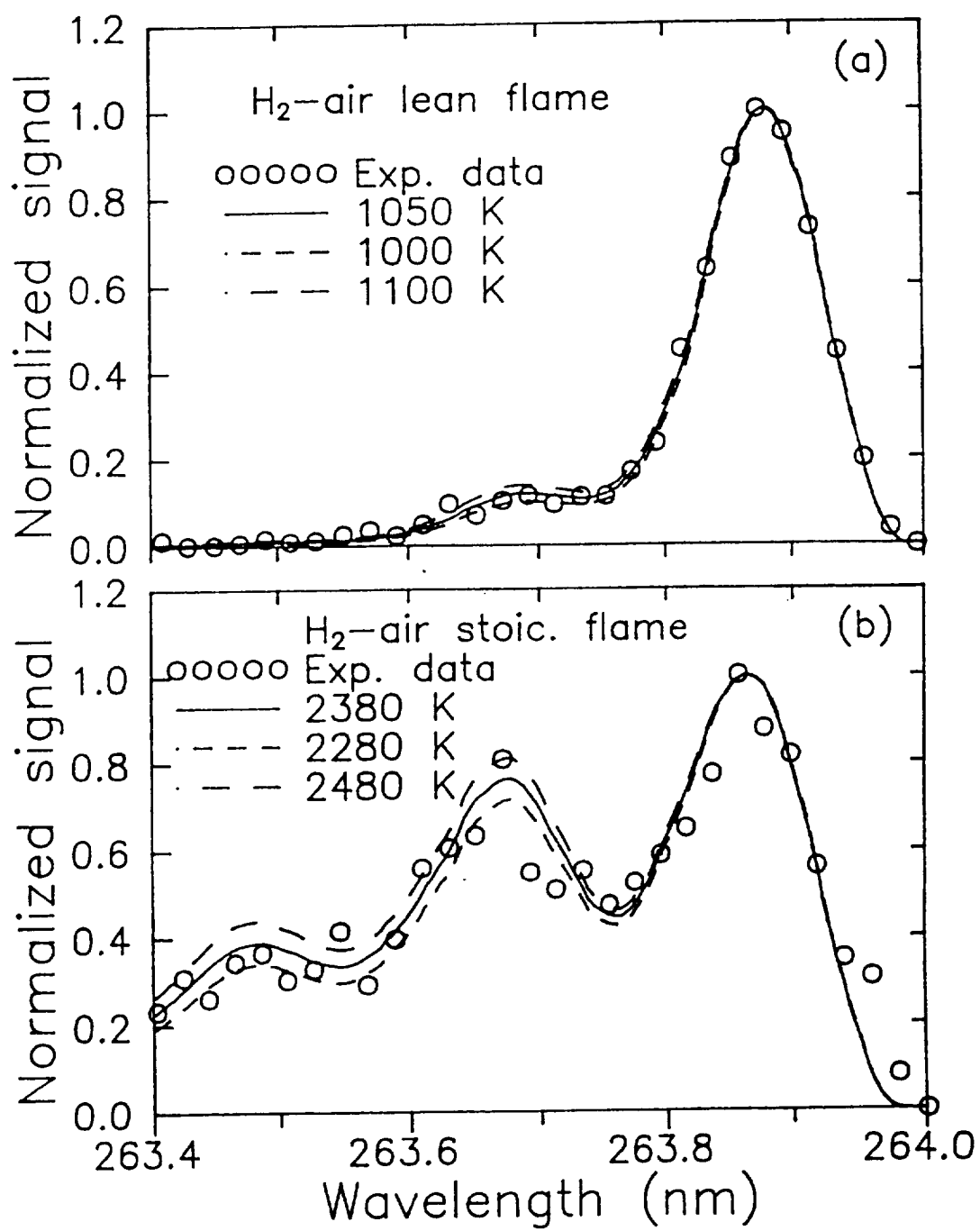
Fig. 10 Theoretical and experimental Stokes N_2 Raman spectra.

To calibrate the Raman and OH fluorescence signals, the measured temperature and measured flowrates are used to calculate the equilibrium species concentrations with the STANJAN equilibrium program (Reynolds, 1986). For major species concentration measurements, Eq. (2-2) can be rewritten as follows (Dibble et al., 1987):

$$Q_i = K_i \, Q_l \, [N_i] \, f_i(T) \tag{4-1}$$

where Q_i is the integrated charge from a PMT collecting the Raman scattering signal from species i, $[N_i]$ is the number density of species i, Q_l is the incident laser energy, K_i is a proportionality constant (dependent on the vibrational Raman cross section, geometry), and optical efficiency, and $f_i(T)$ is the bandwidth factor which accounts for the temperature-dependent distribution of molecules in their allowed quantum states. The bandwidth factor also depends on the spectral location, shape and the bandwidth of the spectrometer and the bandwidth of the laser. It can be calculated for diatomic molecules; however, the calculation is less reliable for polyatomic molecules. Therefore, it is experimentally determined. The terms K_i and $f_i(T)$ are combined to give the calibration factor $C_i = 1/K_i f_i(T)$. The number density of species i is then given by:

$$[N_i] = C_i \, (Q_i / Q_l) \tag{4-2}$$

Various flame spectra (see Fig. 11) obtained with the optimal laser wavelength (248.623 nm) have shown that a small amount of O_2 fluorescence appears at 257, 267, and 277 nm in lean conditions. Residual OH fluorescence also appears at 272
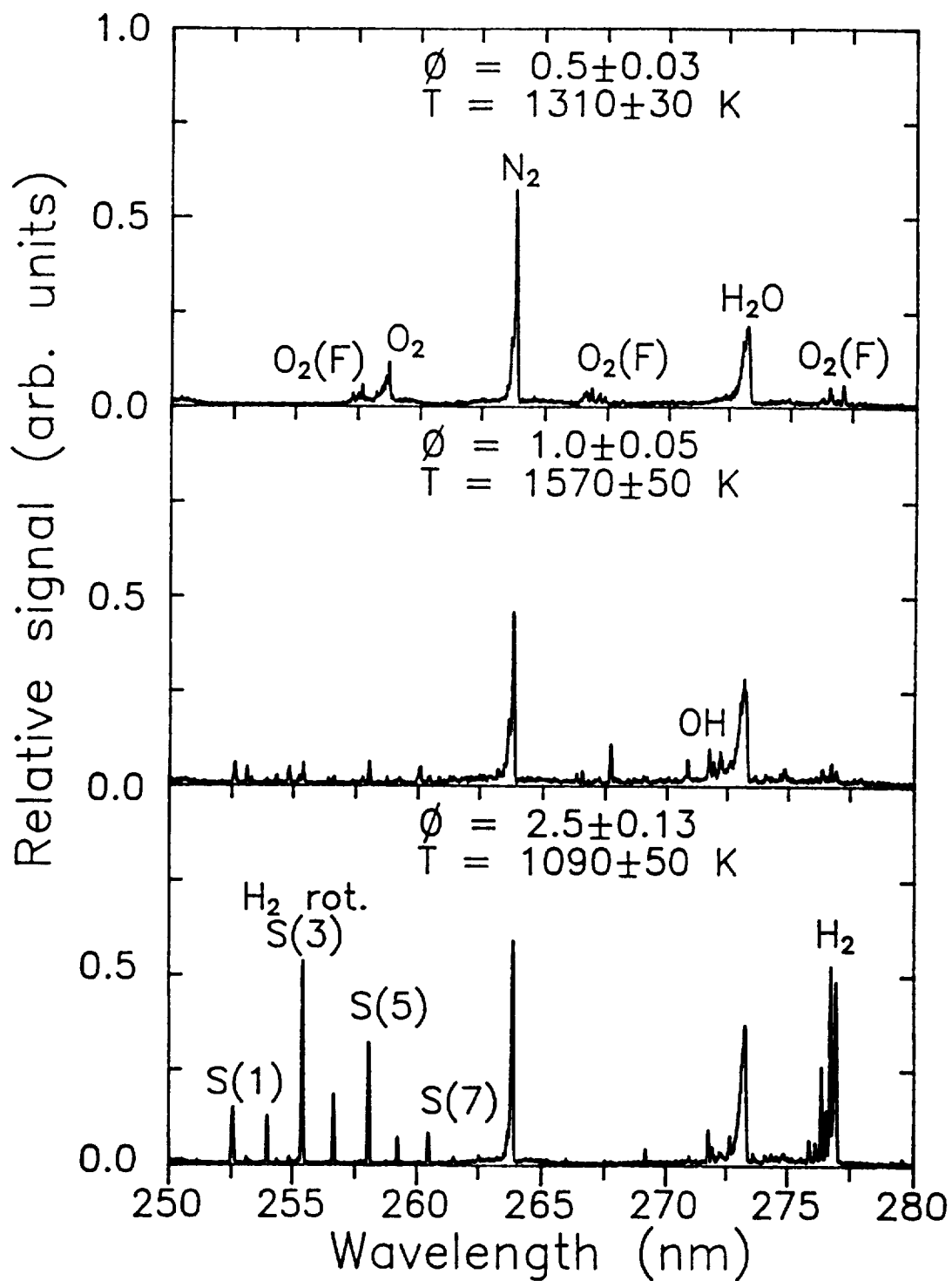
Fig. 11 Narrowband Raman flame spectra for ϕ = 0.5, 1.0, and 2.5.

nm in stoichiometric and high temperature lean and rich flames. In addition, the pure H_2 rotational lines appear from 252 to 261 nm in rich conditions.

The O_2 fluorescence at 257 nm interferes with the O_2 Raman signal (258 nm) and O_2 fluorescence at 277 nm interferes with the H_2 vibrational Raman signal. The residual OH fluorescence (272 nm) interferes with the H_2O Raman signal. The S(4) and S(5) of the pure H_2 rotational lines coincide with the O_2 Raman signal. In turbulent flames, lean, stoichiometric, and rich conditions can occur during the laser measurements. To obtain reliable concentration measurements for all major species, the fluorescence interference and overlapping signals from different species must be subtracted out.

To measure O_2 concentration, the small amount of O_2 fluorescence and the S(4) and S(5) H_2 rotational Raman signals must be subtracted out from the O_2 Raman signal measured by the O_2 PMT. The O_2 fluorescence signal is measured by a different PMT at 337.5 nm (see Fig. 6). The pure H_2 rotational Raman signals are determined from the H_2 vibrational Raman signal times a Boltzmann population fraction and a temperature dependent factor. Since there is no O_2 concentration in the rich Hencken burner flames, the O_2 PMT measured signals are totally attributed to the H_2 rotational signals. The amount of H_2 rotational signal in the O_2 Raman channel can be easily determined from the calibration at several rich flame conditions. However, the percentage of O_2 fluorescence signal that results in interference with the O_2 Raman signal is difficult to determine since both O_2 Raman and O_2 fluorescence coexist in lean flames. An alternative way to obtain the

calibration curve for O_2 concentration measurement is to subtract out a percentage

of O_2 fluorescence signal from the O_2 Raman signal until a monotonic-decreasing

least-squares fitting curve is obtained. Normally the percentage of O_2 fluorescence

signal that needs to be removed varies from 10 to 25%. The calibration curve is

shown in Fig. 12. For the N_2 concentration measurement, there is no fluorescence

interference. The calibration curve is shown in Fig. 13 for the measured calibration

flames.

For the H_2O concentration measurement, the residual OH fluorescence has

to be subtracted out from the H_2O Raman signal. The OH fluorescence is measured

by a different PMT at 297.5 nm (see Fig. 6). Since the OH radical exists in

stoichiometric and high temperature lean and rich conditions, the amount of OH

fluorescence that needs to be removed cannot be directly determined from both H_2O

Raman and OH fluorescence signals during calibration. The procedure of obtaining

the calibration curve for H_2O is identical to that for O_2. The percentage of OH

fluorescence removed varies from 1 to 5%. The calibration curve is shown in Fig.

14.

Fig. 15 shows the calibration curve for H_2. The data are obtained from the

calibration with the Hencken burner in rich flame conditions except for a point in

room temperature pure hydrogen. The datum at 300 K is obtained in the potential

core of a lifted flame where pure hydrogen exists. This is to avoid running unburnt

hydrogen through the Hencken burner into the laboratory. The amount of O_2

fluorescence removed from the H_2 Raman signal in turbulent flame measurement is
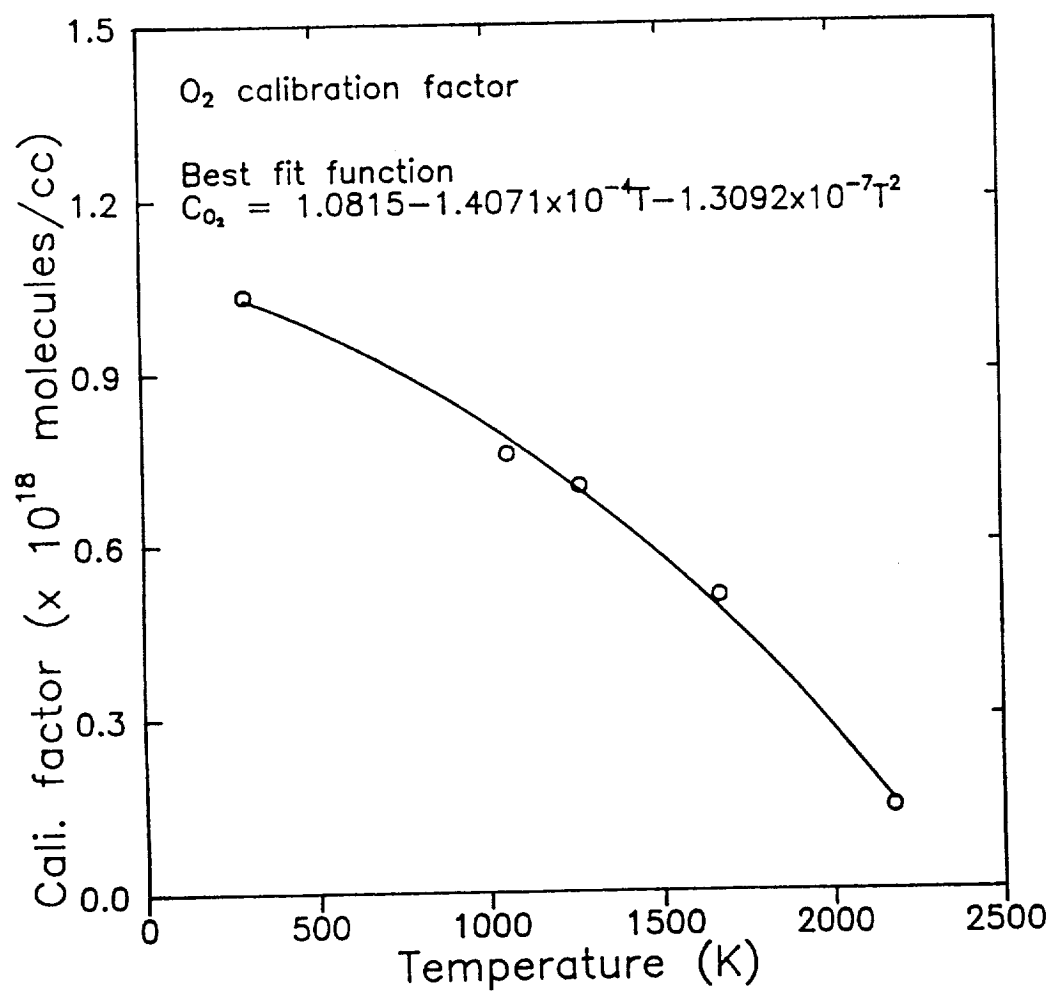
Fig. 12 Variation of the calibration factor of O_2 with temperature.
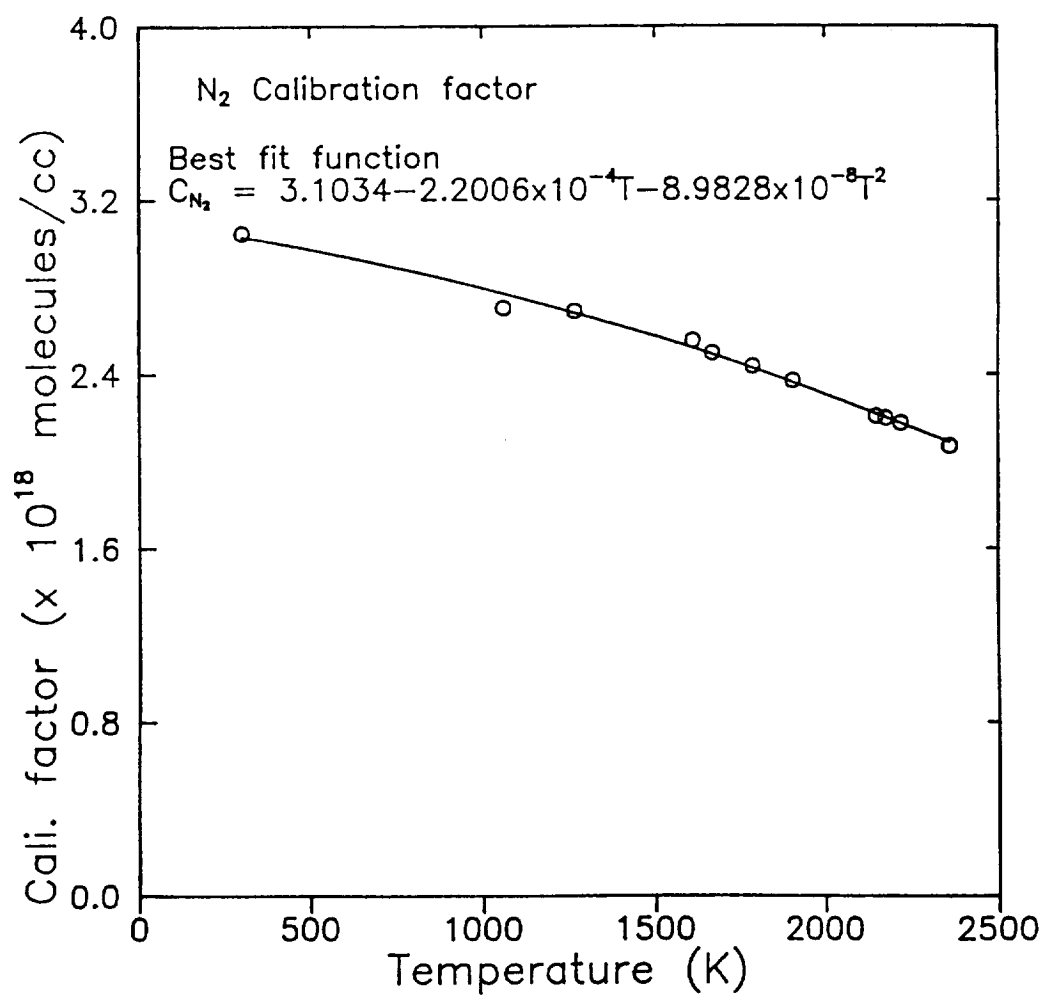
Fig. 13 Variation of the calibration factor of N_2 with temperature.
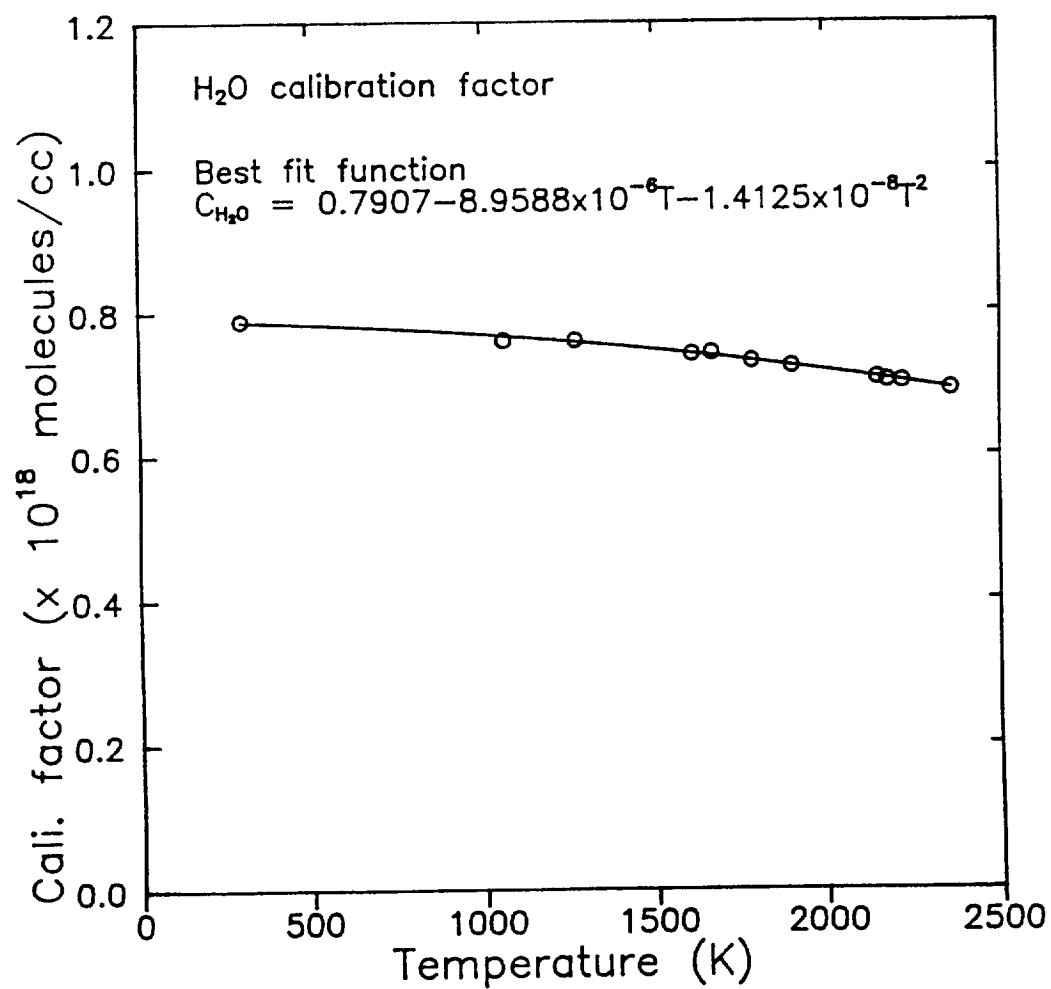
Fig. 14 Variation of the calibration factor of H_2O with temperature.
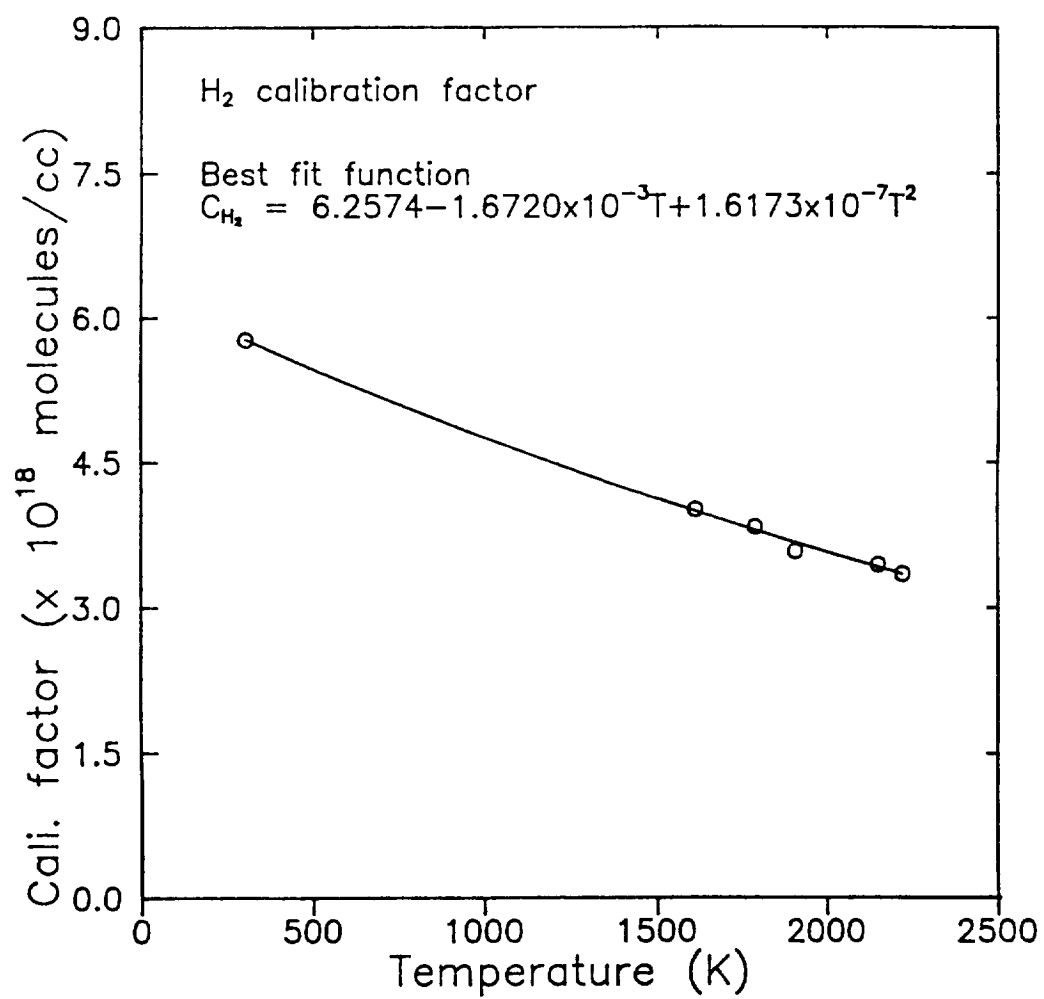
Fig. 15 Variation of the calibration factor of H_2 with temperature.

obtained from the calibration in the Hencken burner under lean conditions.

Calibration for OH Measurement

For the OH concentration measurement, the laser-induced predissociative fluorescence (LIPF) process is employed. The 5% unlocked broadband part of the narrowband laser excites OH molecules from $v'' = 0$ to $v' = 3$ in the $A^2\Sigma \leftarrow X^2\Pi$ system (see Fig. 16). The $v' = 3$ state is predissociated due to a crossing of the $a^4\Sigma^-$ state (German, 1975). The predissociating rate of $v' = 3$ state is $\sim 1.0 \times 10^{10}$ s^{-1} which is estimated using the Heisenberg uncertainty principle and the theoretically obtained linewidth by Sink and Bandrauk (1980). The collisional quenching cross sections of $v' = 3$ state are not either theoretically or experimentally determined. Therefore, the collisional quenching cross sections of the $v' = 0$ state obtained by Garland and Crosley (1986) are used to determine the collisional quenching rate for the $v' = 3$ state. The highest calculated value is $\sim 0.5 \times 10^9$ s^{-1} for a temperature of 1500 K in a rich-flame condition. The fluorescence rate of the $v' = 3$ state is assumed to be the same order of magnitude as the $v' = 0$ state ($\sim 10^6$ s^{-1}, Garland and Crosley, 1986).

The predissociating rate is greater than the collisional quenching rate and the fluorescence rate. Therefore the collisional quenching correction is unnecessary if fluorescence is measured from the $v' = 3$ state. The LIPF technique has been employed for OH fluorescence imaging inside an internal combustion engine by Andresen et al. (1990).
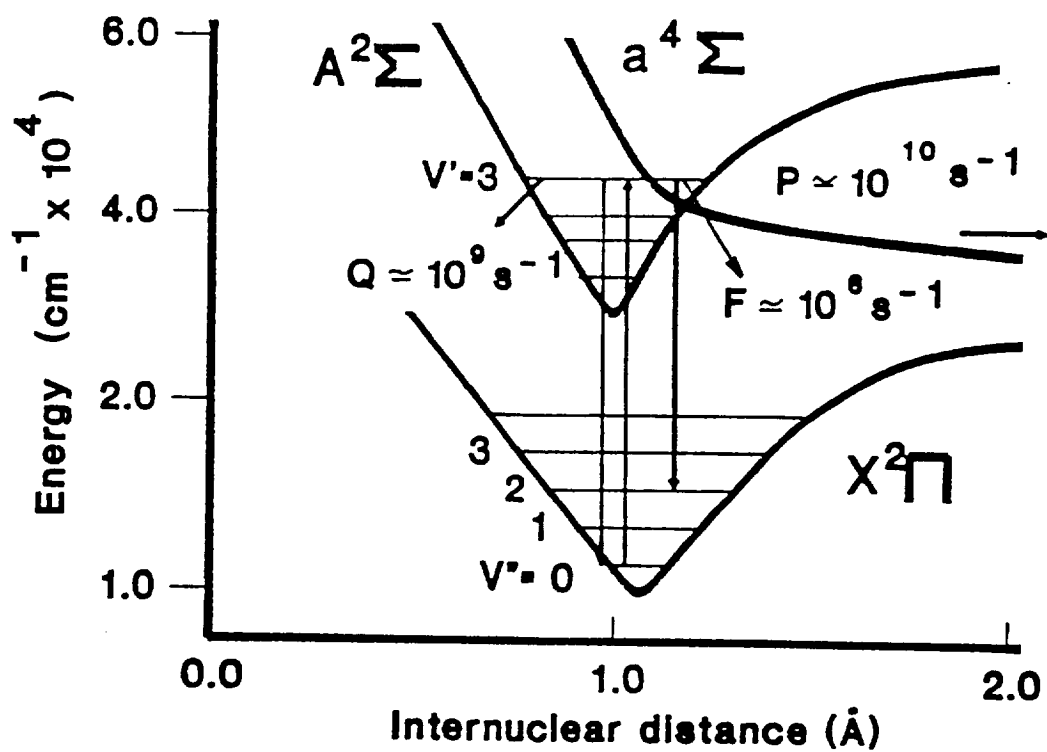
Fig. 16 Schematic diagram of OH potential energy.

The excited OH molecules can fluoresce down to the ground electronic state ($X^2\Pi$) by several paths. Fluorescence from the (3,0) band produces emission near 250 nm and fluorescence from the (3,1) band produces emission in the 272 nm region which interferes with the H_2O Stokes Raman signal. There are other emission bands that do not interfere with the Raman signal, such as the (3,2) lines at 297.5 nm or the (3,3) lines near 330 nm (Bass and Broida, 1953).

The (3,2) emission lines at 297.5 nm are used for the OH fluorescence measurement as the other lines overlap with other signals or are outside the spectrometer spectral range. It is worth noting that the OH molecules in the upper excited electronic state ($v'=3$) can depopulate to the lower vibrational states ($v'=2$, 1, 0) by vibrational/rotational energy transfer. As a result the emissions ((2,2), (2,1), (1,1), (1,0), (0,0), etc.) from the lower vibrational states in the excited $A^2\Sigma$ state are collisionally quenched and are not considered for OH concentration measurement.

For predissociative fluorescence measurement, the measured OH intensity is related to the OH number density as follows:

$$I_F = C(F/(F+Q+P))I_L[N_{OH}]f_B(T) \qquad (4\text{-}3)$$

where C is a constant dependent on optical and detector efficiency, F is the fluorescence rate, Q is the collisional quenching rate, P is the predissociating rate, I_L is the incident laser intensity, $[N_{OH}]$ is the OH number density, and $f_B(T)$ is the temperature dependent Boltzmann population fraction. Since P is greater than F plus Q, Eq. (4-3) can be simplified as:

$$I_F = C(F/P)I_L[N_{OH}]f_B(T) \qquad (4\text{-}4)$$

To demonstrate that the measured intensity is not sensitive to temperature, a calculation is performed. The ground vibrational state energy (Dieke and Crosswhite, 1962) for all the rotational lines (see Fig. 9) within the laser tuning range is used to calculate the sum of OH population fraction for the temperature range from 300 to 3000 K. In the calculation each rotational line is weighted by its respective transition probability. The result shows that the sum of the weighted OH population fraction is temperature insensitive ($<$ 15%) from 1500 to 3000 K (see Fig. 17). Although the weighted population fraction varies strongly from 300 to 1500 K, few OH molecules exist in the H_2-air flames below 1500 K. Thus the OH LIPF signal is linearly proportional to the OH concentration.

The constants in Eq. (4-4) can be grouped into a single calibration constant, a, and Eq. (4-4) becomes linear:

$$[N_{OH}] = a(I_F/I_L) + b \qquad (4\text{-}5)$$

where b is a constant.

The OH linear relationship is calibrated in the Hencken burner at 5 cm, as shown in Fig. 18, where the OH molecules have recombined to give an equilibrium concentration. The convective time is approximately 10 ms from the Hencken burner surface to 5 cm downstream. The OH recombination time (~3 ms) for a stoichiometric H_2-air flame is found to be about the same as that for a stoichiometric methane-air flame (Cattolica, 1982).
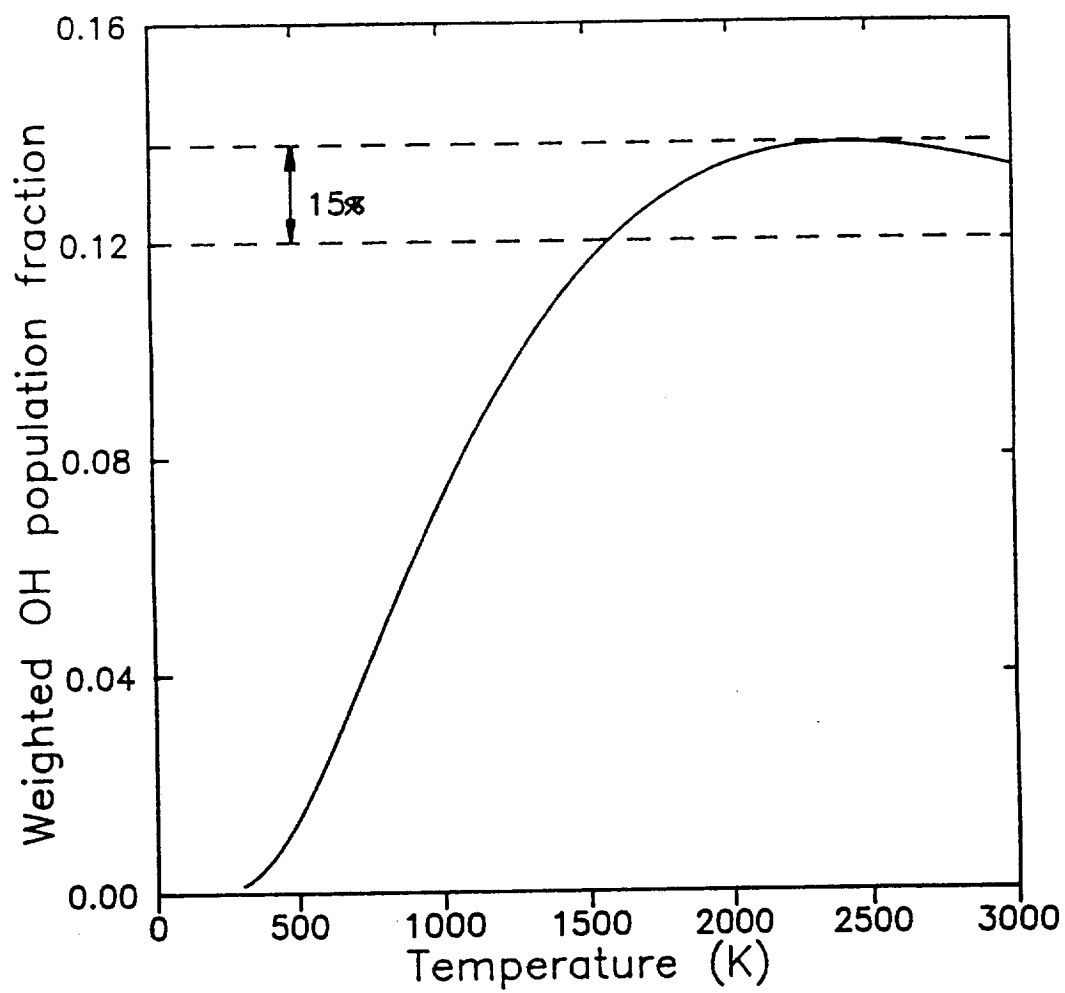
Fig. 17 Variation of weighted OH population fraction with temperature.
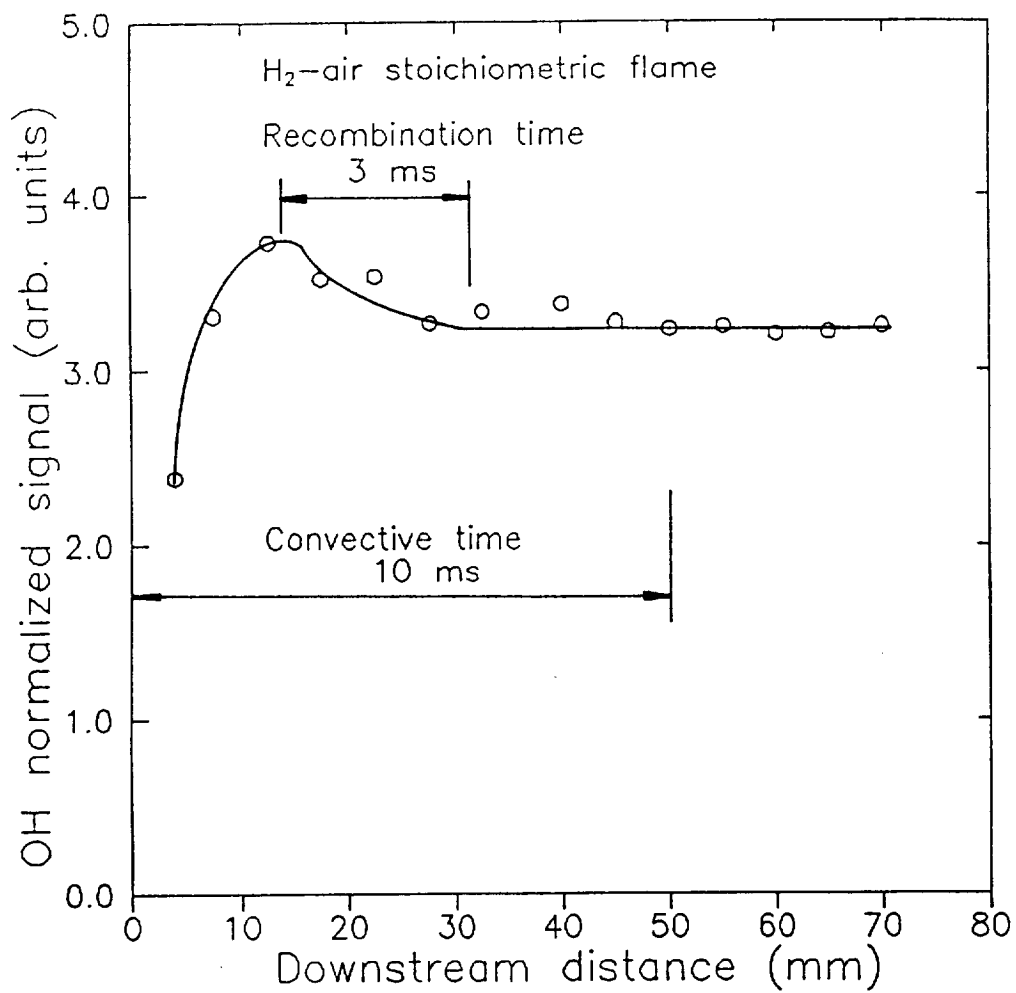
Fig. 18 Variation of OH concentration in the Hencken burner.

The calibration function as shown in Fig. 19 is calibrated from lean to rich flame conditions. The O_2 fluorescence interferes with the OH fluorescence signal at high temperature lean conditions and is corrected by monitoring the O_2 fluorescence at 337.5 nm. For the normalized signal less than 1.4, there are two points which have very small amount of OH density, about 18-30% of the maximum normalized signal, possibly due to the non-uniform power distribution of the focused laser beam (0.75mm x 0.25mm) causing two-photon photodissociation of water vapor and producing OH photofragments.

A H_2O excitation spectrum is shown in Fig. 20. To obtain this spectrum, a 1000 mm focusing length lens is used to produce two-photon process, the Hencken burner is operated at a fuel-lean condition ($\phi = 0.23$), and the spectrometer is set to 417 nm with a 4.4 nm bandpass. The arrow indicates that the optimal laser wavelength may resonate with line number 3 to cause photodissociation of water vapor. For future improvement of the Raman system, two cylindrical focusing lenses will be used to produce a square cross section (0.4mm x 0.4mm) and a more uniform power distribution. The optimal laser wavelength will be readjusted to avoid resonance with any rotational line in the O_2, OH, or H_2O excitation spectra.

Temperature Measurement

The vibrational temperature measurement of N_2 is made using the ratio of the Stokes signals, N_s, to detected anti-Stokes signals, N_a. The temperature is given by (Drake et al., 1982b):
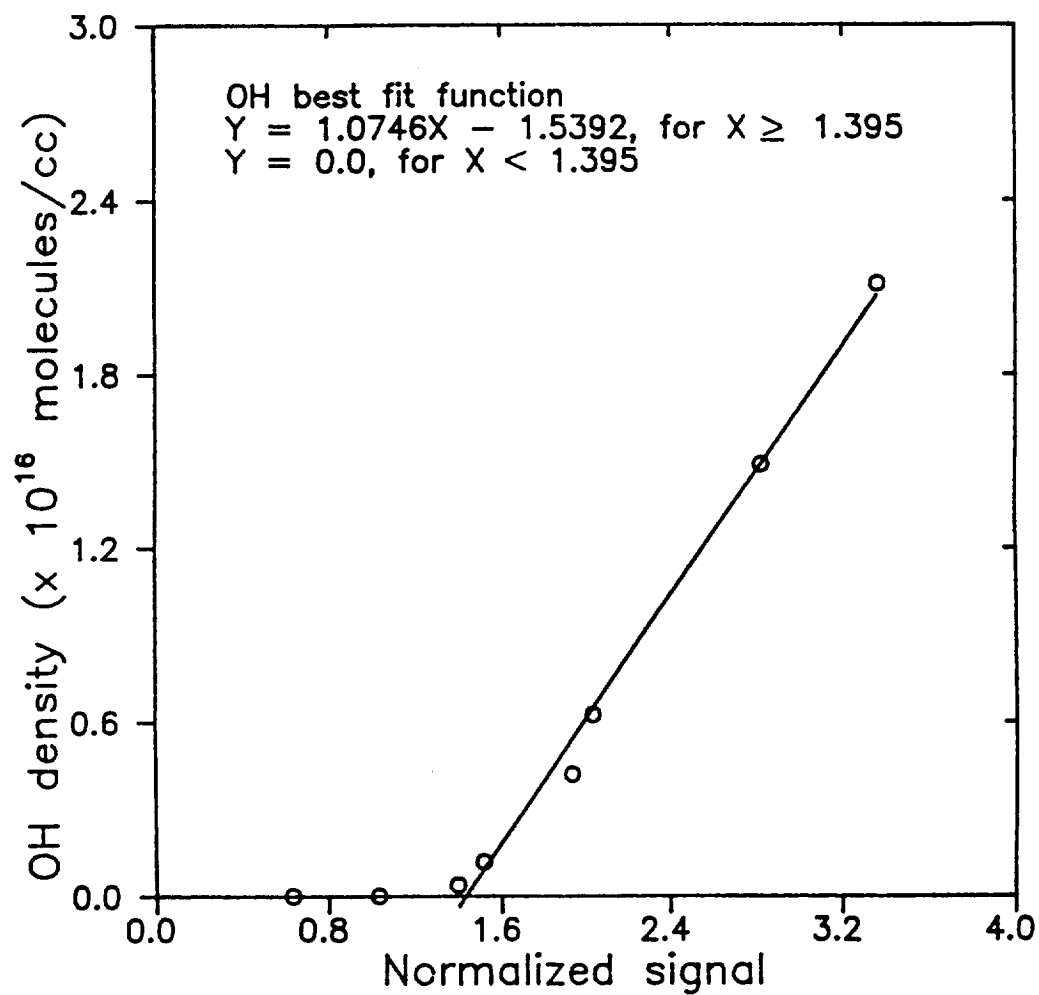
Fig. 19 Calibration function for OH measurement.
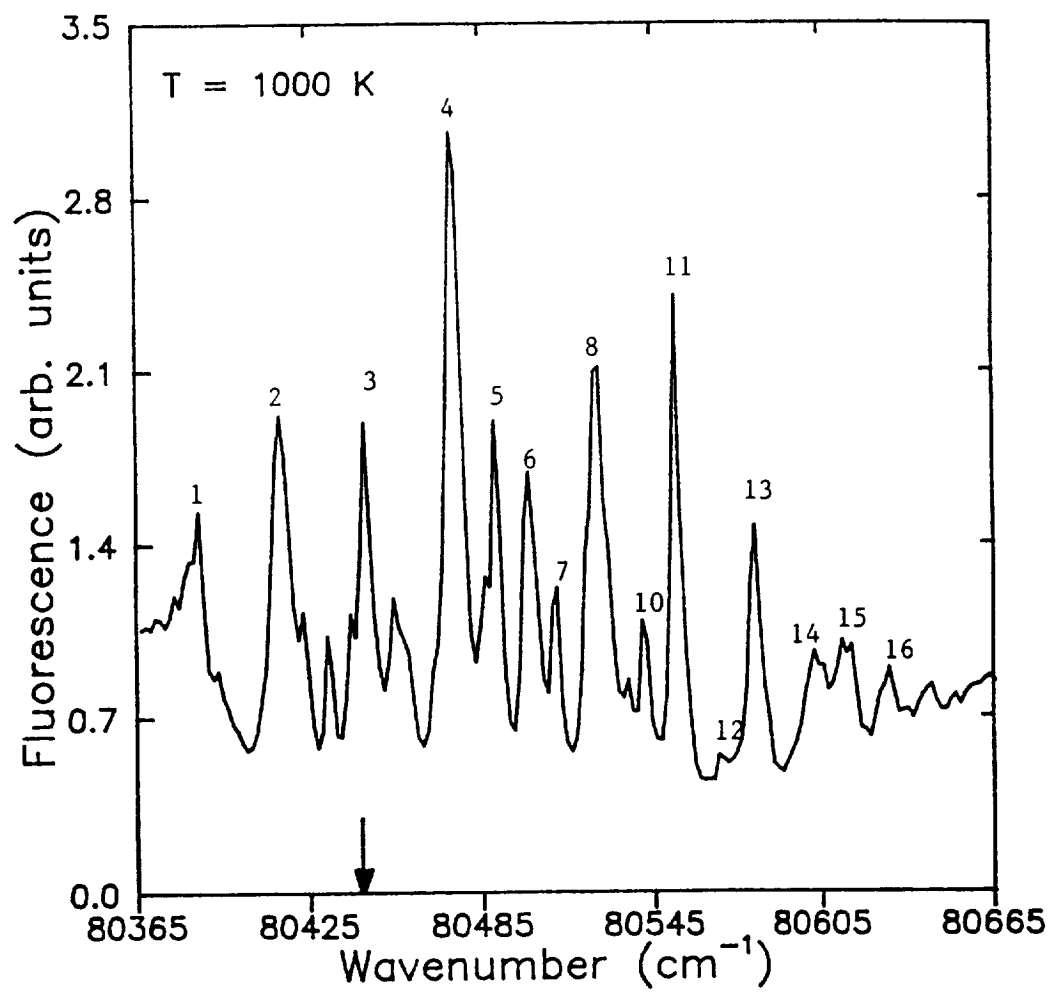
Fig. 20 H₂O fluorescence excitation spectrum.

$$T = \frac{T_V}{\ln(N_s/N_a) + 3\ln(v_a/v_s) + \ln(K)} \qquad (4\text{-}6)$$

where T_V is the characteristic vibrational temperature of the gas species (3357.6 K for N_2) and K is the ratio of the optical efficiencies at the anti-Stokes and Stokes wavelength. The anti-Stokes frequency shift is $v_a = v_L + v_R$ and the Stokes frequency shift is $v_s = v_L - v_R$. The optical efficiencies and the ratio of anti-Stokes to Stokes frequency can be grouped together to give a single calibration constant, C_T. The temperature is then given by:

$$T = \frac{3357.6K}{\ln(N_s/N_a) + C_T} \qquad (4\text{-}7)$$

For temperatures below 800 K, Eq. (4-7) becomes less accurate. Instead, the perfect gas law is used to arrive at the temperature measurement by adding the number densities of the major species and assuming atmospheric pressure. Perfect gas law thermometry normally has better accuracy than the Stokes/anti-Stokes method because all major species concentrations are measured from the ground vibrational state. However, its application is limited to a constant pressure flame.

For each equivalence ratio, an ensemble of 500 single laser shot measurements is taken in the Hencken burner. The averages of these various ensembles are used to obtain the calibration constants and bandwidth factors. For the turbulent flame measurements, this calibration procedure is performed each day at the beginning and/or end of each experimental run.

Calculation of Mixture Fraction

The mixture fraction, f, is a conserved scalar that describes the state of mixing between fuel and oxidizer. The mixture fraction is calculated from the Raman scattering measurements of the major species concentrations for each laser shot as the mass originating from the fuel stream divided by the total mass (Pitz and Drake, 1986; Magre and Dibble, 1988):

$$f = \frac{\left[\dfrac{2[H_2]+2[H_2O]}{32[O_2]+28[N_2]+18[H_2O]+2[H_2]}\right] - Z_{H,a}}{1 - Z_{H,a}} \qquad (4\text{-}8)$$

where $Z_{H,a}$ is the mass fractions of hydrogen atoms in the still air. This is given by $Z_{H,a} = (2/18)(\omega/(1+\omega))$ where ω is the specific humidity (kg H_2O/kg dry air) in the ambient air. The humidity is frequently measured from a humidity gauge. The OH concentration and $Z_{H,a}$ (< 0.001) are not included in the mixture fraction calculation for lifted turbulent jet flame measurements, because the error in mixture fraction is small. The mixture fraction is 1 in pure hydrogen, 0 in pure air, and 0.0283 at stoichiometric.

Uncertainty Analysis

In a scattering measurement of gas concentration, the number of detected photoelectrons will show a statistical variation because the detection of photons using a photocathode is a random process. The number of photoelectrons detected in a series of identical measurements will have a Poisson distribution about the mean

value, N, with a standard deviation of $N^{1/2}$. The mean value of photoelectrons is determined by the average number of incident photons that successfully cause a photoelectron emitted from the photocathode surface, and is given by (Lapp et al., 1973; Eckbreth, 1988):

$$N = MQ \qquad (4-9)$$

where M is the average number of incident photons, and Q is the quantum efficiency. For a Poisson distribution, the standard deviation is the expected rms deviation from the mean value (Larsen and Marx, 1986), and is given by:

$$\sigma = \sqrt{MQ} \qquad (4-10)$$

The relative standard deviation that describes the probable error in a single shot measurement is given as the standard deviation over the mean:

$$Rel.\ SD = \frac{\sqrt{MQ}}{MQ} = \frac{1}{\sqrt{N}} \qquad (4-11)$$

For a Raman scattering measurement, the major contributor to the single-shot signal uncertainty is photon statistical shot noise. Thus, in order to reduce the measurement uncertainty a strong signal and a high quantum efficiency detector are needed.

For temperature measurement, the relative standard deviation (σ_T/T) from a single laser shot can be calculated approximately by (Drake et al.,1982b):

$$\frac{\sigma_T}{T} \approx \frac{1}{T}\left[\left(\frac{\partial T}{\partial N_s}\sigma_s\right)^2 + \left(\frac{\partial T}{\partial N_{AS}}\sigma_{AS}\right)^2\right]^{1/2} \qquad (4-12)$$

where σ_S is the standard deviation in the Stokes measurement, σ_{AS} is the standard deviation in the anti-Stokes signal, and σ_S/N_s and σ_{AS}/N_{AS} are small compared to unity. Eq. (4-12) can be simplified to:

$$\frac{\sigma_T}{T} \approx \frac{T}{T_V}\left[\frac{1}{N_s} + \frac{1}{N_{AS}}\right]^{1/2} \qquad (4\text{-}13)$$

where T_V is the characteristic vibrational temperature, and N_S and N_{AS} are the expected number of detected photoelectrons for the Stokes and anti-Stokes signals, respectively.

An estimate of the signal uncertainty for N_2 measurements in room air can be made by inserting the various parameters in Eq. (2-3). The various parameters are: $n = 1.91 \times 10^{19}$ molecules/cc, $\eta_{spect} = 0.2$, $\eta_{prism} = 0.64$, $\eta_{filter} = 0.8$, $Q = 0.2$, $\epsilon_{casse} = 0.25$, $L = 0.04$ cm, $\Omega = 0.349$ sr, $\sigma = 10 \times 10^{-30}$ cm^2/sr, $E_L = 0.1$ J (polarized), and $h\nu_s = 7.553 \times 10^{-19}$ J/photon. The bandwidth factor, $f(T)$, is relatively close to one at room temperature. The listed parameters, when inserted in Eq. (2-3), give an estimated photoelectron measurement of 1807. Inserting this value in Eq. (4-11) gives an expected relative standard deviation of 2.4% for N_2 measurement at room air conditions. The population fraction of N_2 molecules in excited vibrational states is 0.00005 at room air condition. Thus, there will be no measurable anti-Stokes signal. The perfect gas law is used to arrive at temperature measurements for temperatures below 800 K.

In a flame at 1620 K all of the parameters will remain about the same except

that the bandwidth factor increases to 1.22 and the number density of N_2 reduces to 3.24×10^{18} molecules/cc. The expected photoelectron count is 374, and the photon statistics relative standard deviation is 5.2%. The expected number density of vibrationally excited N_2 molecules is 38% of the total, or 1.23×10^{18} molecules/cc. The sample length for the N_2 anti-Stokes measurement is 0.033 cm. The throughput of the double-monochromator is ~10%. The optical constants for the N_2 anti-Stokes measurement are obtained from the calibration constant C_T in Eq. (4-7). These parameters give an expected photoelectron count of 27 for the N_2 anti-Stokes signal. Inserting these numbers into Eq. (4-13) results in an expected relative standard deviation of 9.6% for temperature measurement.

An extensive study of the influence of signal strengths upon measurement uncertainties for concentration and temperature has been performed by Bowling (1988) and Wehrmeyer (1990). Only a few calculations are performed in this work. A comparison of estimated and measured relative standard deviations for N_2 concentration and temperature measurements is shown in Table 2. It shows that the estimated relative standard deviations correspond well with the measured values.

Data Reduction

After the constant, C_T, for Eq. (4-7) and the calibration factors for species concentrations are determined from the calibration measurements, they are used with a data reduction program (see Appendix A) to arrive at single shot temperature and concentration measurements. In the program when the Stokes/anti-Stokes signal

Table 2. Comparison of estimated and measured relative standard deviations.

ϕ	Temp.(K)	Estimated relative SD(%)		Measured relative SD(%)	
		N_2	Temp.	N_2	Temp.
0	300	2.4	-	2.7	-
0.5	1620	5.2	9.6	5.9	10.2
1.0	2280	5.9	10.5	6.3	11.7
2.1	1820	6.6	11.9	7.2	12.7

strengths are too low and/or temperature is below 800 K, the perfect gas law is used to obtain the temperature. In this case, the temperature is first assumed to be 300 K and the resulting total number density is then used to compute the next temperature. Iteration is continued until a convergence criterion is met. Other quantities such as density, conventional and Favre averages of mixture fraction, mean and rms values of temperature and concentration, are calculated in the program.

The relative standard deviations of mixture fraction, temperature, major species, and minor species concentrations from single-shot calibration measurements are listed in Table 3. The maximum temperature difference from the two different methods is 130 K. Temperatures obtained by the perfect gas law give better accuracy, because all major species concentrations are measured from the ground vibrational state. For H_2O concentration measurement, the lower quantum efficiency miniature PMT gives higher uncertainties. The relative standard deviations for OH concentration measurements are much higher than those for major species measurements because the OH concentrations are small in the equilibrium flames.

Calibration results are presented in Figs. 21 and 22. The experimental data, which are given in terms of the mean values and error bars at the single-pulse standard deviations, are compared with theoretical adiabatic equilibrium curves. Fig. 21a shows the Stokes/anti-Stokes temperature measurements. For stoichiometric and some rich-flame conditions, the measured mean temperature is still up to 200 K less than the adiabatic flame temperature due to heat transfer to the Hencken burner surface. Under these conditions, the burner surface is visibly glowing red. The

Table 3. Single-shot measurement relative standard deviations.

ϕ	T_{adia} (K)	$T_{S/AS}$ (K)	T_{perf} (K)	$T_{S/AS}$	T_{perf}	Relative standard deviation(%)					
						f	O_2	N_2	H_2O	H_2	OH
0	300	-	300	-	5.0	11.4	2.8	2.7	11.0	-	-
0.23	1010	1060	1040	9.6	6.5	9.3	6.6	4.8	8.7	-	-
0.32	1240	1250	1270	8.4	6.7	8.7	8.7	5.3	8.4	-	-
0.50	1640	1620	1670	10.2	8.1	9.6	15.2	5.9	9.0	-	48.6
0.80	2160	2110	2170	11.2	11.3	11.0	18.0	6.6	9.9	-	18.2
1.00	2380	2280	2380	11.7	10.4	10.0	-	6.3	8.9	-	13.2
1.30	2330	2150	2280	12.3	9.4	9.7	-	6.6	9.3	13.9	18.7
1.42	2280	2080	2180	11.7	9.0	8.9	-	7.1	8.6	10.4	19.6
2.10	2020	1820	1880	12.7	8.5	8.8	-	7.2	11.3	7.2	46.0
2.55	1890	1760	1780	11.9	8.2	8.6	-	7.4	11.1	6.8	-
3.40	1680	1660	1630	9.9	7.4	8.1	-	7.4	9.5	5.8	-
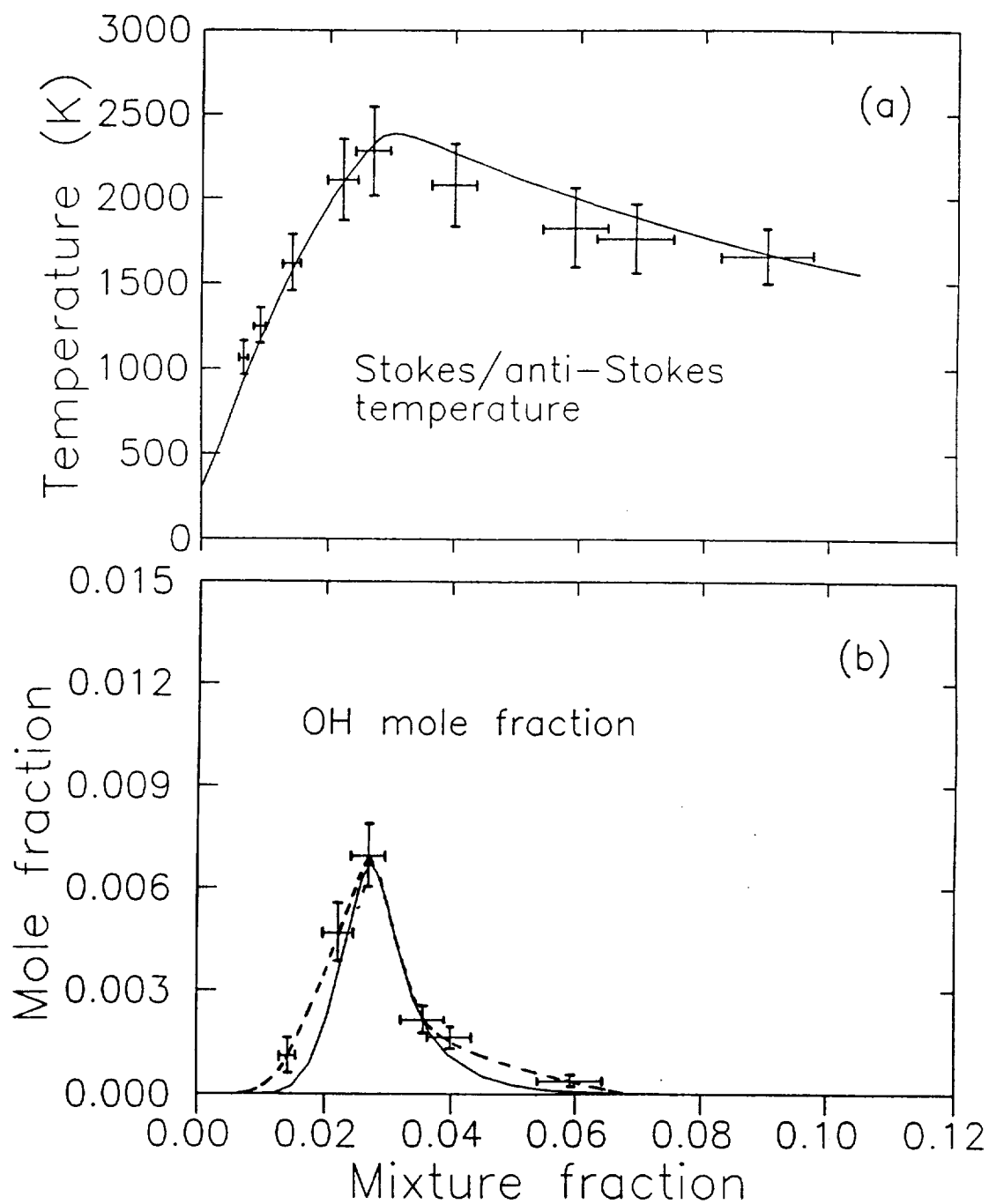
Fig. 21 Calibration results for temperature and OH concentration measurements.
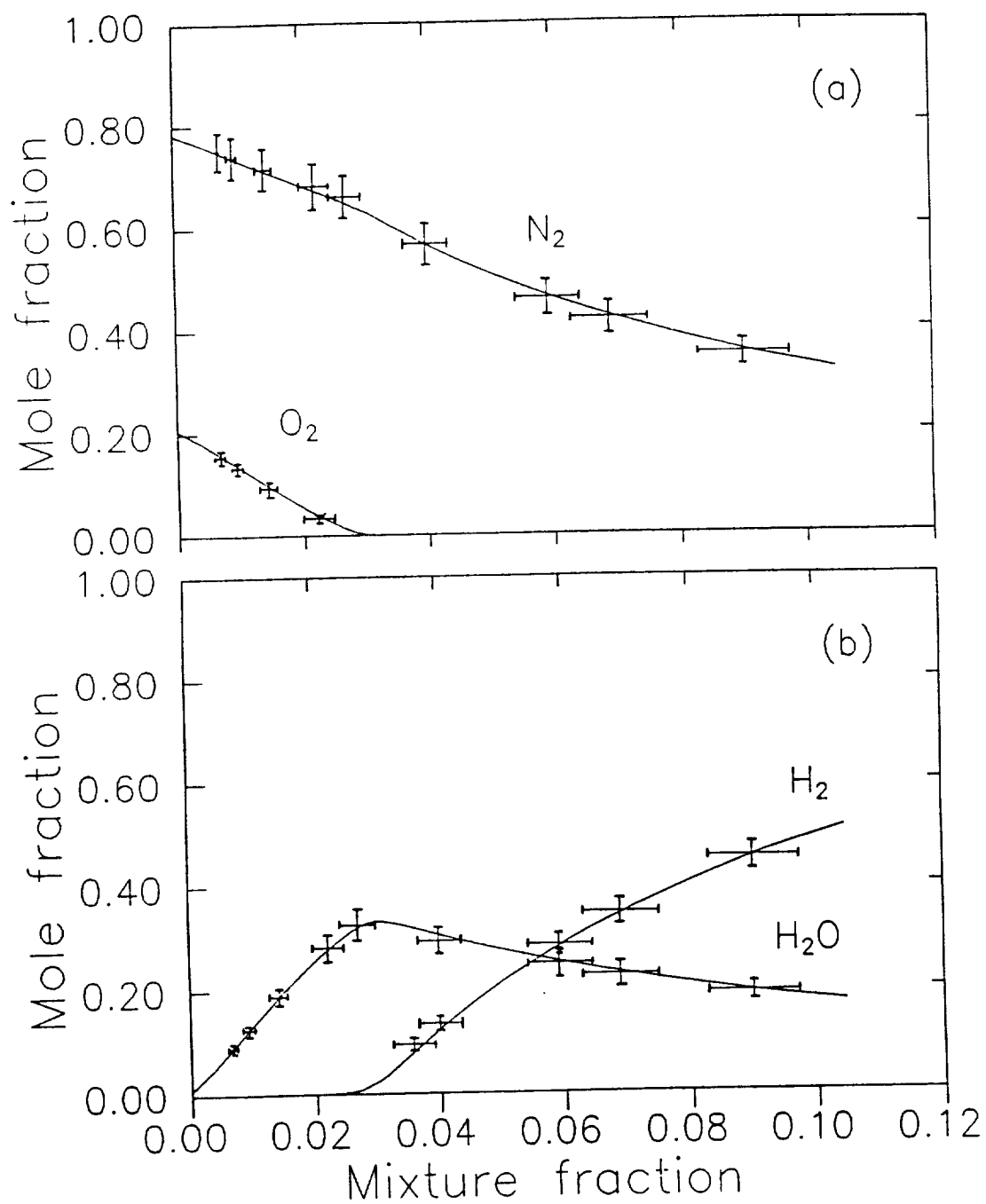
Fig. 22 Calibration results for O_2, N_2, H_2O, and H_2 concentration measurements.

variations of mixture fraction are correlated to all major species concentrations according to Eq. (4-8). Fig. 21b shows the OH calibration measurements. The dashed curve shows that the measured OH concentrations are slightly higher than the equilibrium values. This may be due to two-photon photodissociation of H_2O and producing small amount of OH photofragment. The results for N_2 and O_2 (see Fig. 22a) and H_2O and H_2 (see Fig. 22b) concentrations show good agreement with equilibrium values. The well-calibrated Raman system is then capable of analyzing flows where conditions are unknown.

CHAPTER V

LIFTED TURBULENT FLAME MEASUREMENTS

Jet Diffusion Flame

A schematic diagram of the jet diffusion burner is shown in Fig. 23. This jet diffusion burner is a simple straight tube which has a 9.5 mm inner diameter with a 10° taper to a 2 mm inner diameter at the nozzle exit. The rim thickness at the jet exit is about 0.2 mm to minimize the effects of the formation of a recirculation zone at the jet exit. A lifted hydrogen diffusion flame is formed by injecting fuel through a straight tube into the still atmospheric air. The jet has an exit velocity of 680 m/s which is calculated based upon the flowrate and the jet exit diameter (Reynolds number = 13600, Mach number = 0.54, and temperature = 280 K). The Froude number of the jet (U_0^2/gD, where g is the gravitational acceleration) is 2.4×10^7. For the jet exit velocity of 680 m/s an attached flame cannot be maintained. The liftoff height is about 7 diameters (visible flame base). The total flame length (~175D) is divided into three zones: lifted zone, slow three-body recombination zone, equilibrium zone. The four solid circles represent the locations for scatter plots which will be shown later.

This jet flame generated a significant amount of noise, requiring ear protection, due to the strong fluctuations of the pressure field at the jet exit. The jet
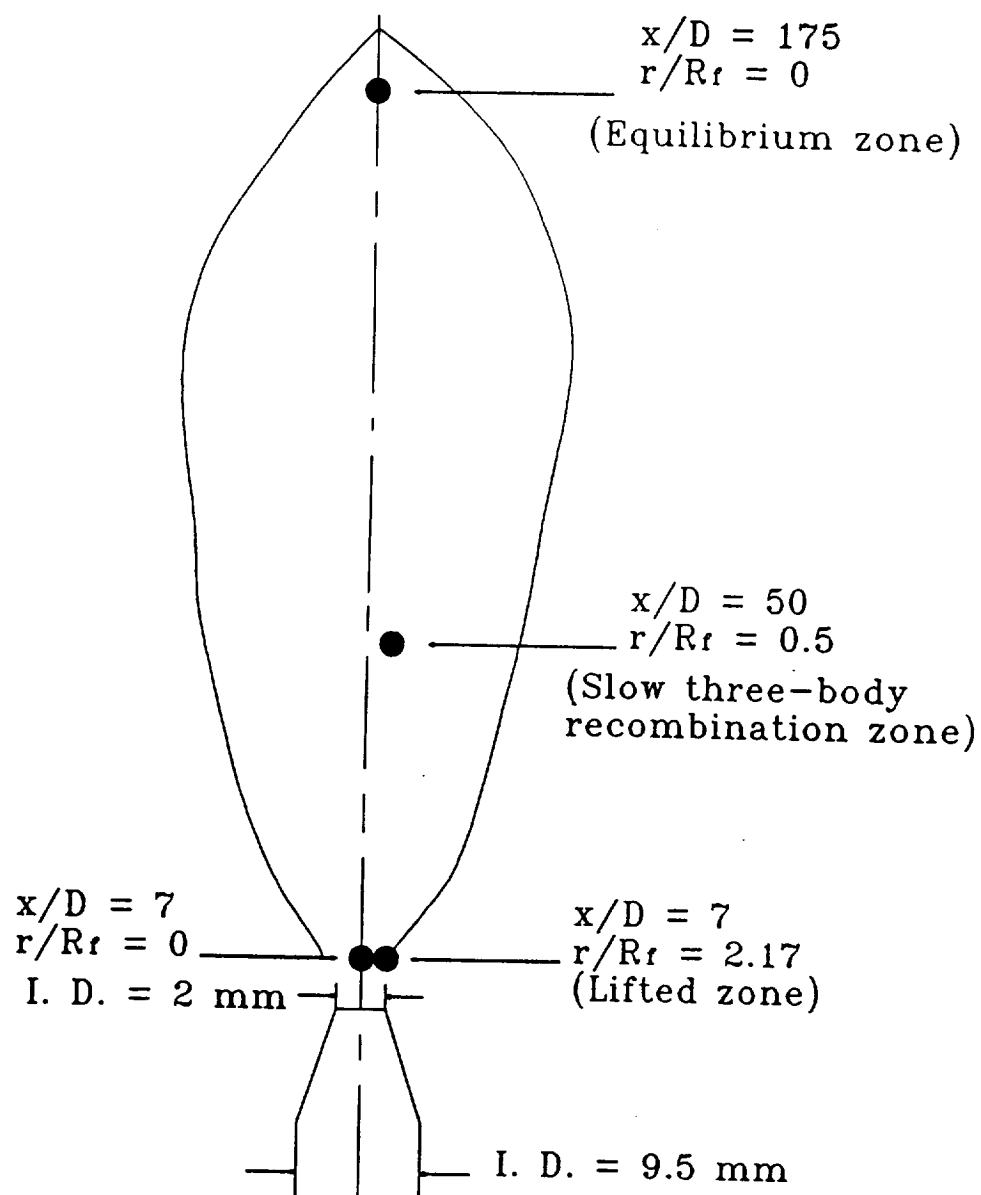
Fig. 23 Schematic diagram of jet diffusion burner.

is mounted on a 3-D translation stage while the optical system remains fixed. In order to center the jet in the laser beam, helium gas is injected through the nozzle while the N_2 Stokes signal is monitored by an oscilloscope. As the jet is horizontally moved toward the laser beam (3 mm above the jet nozzle), the N_2 Stokes signal decreases. The center of the jet is found when the N_2 signal decreases to a minimum value.

Temperature, Mixture Fraction, and Concentration Profiles

UV Raman measurements are made in the radial direction at following downstream locations: x/D = 7, 9.5, 30, 50, 100, 150, 175. At each measurement location 1000 independent laser shots were taken. In order to maximize the laser pulse energy, the laser is operated at 20 Hz. Operating at 100 Hz would decrease pulse energy by about 10%. For each single laser shot the thermodynamic state properties such as temperature and species concentration are measured in the flame. Other instantaneous quantities such as density and mixture fraction are calculated.

The radial profiles of mean and rms temperatures at x/D = 7, 9.5, 50, 100, and 175 are shown in Fig. 24. The radial distance is normalized by the half-radius based upon mean mixture fraction, R_f. The value of R_f is 1.84, 2.82, 7.8, 12, 24, 33.6, and 37.2 mm for x/D = 7, 9.5, 30, 50, 100, 150, and 175, respectively. Temperature profiles for x/D = 30 and 150 have been omitted for clarity. The maximum mean flame temperature determined from the radial profiles increases from the lifted zone near the nozzle to x/D = 100 and decreases thereafter to the equilibrium zone (see
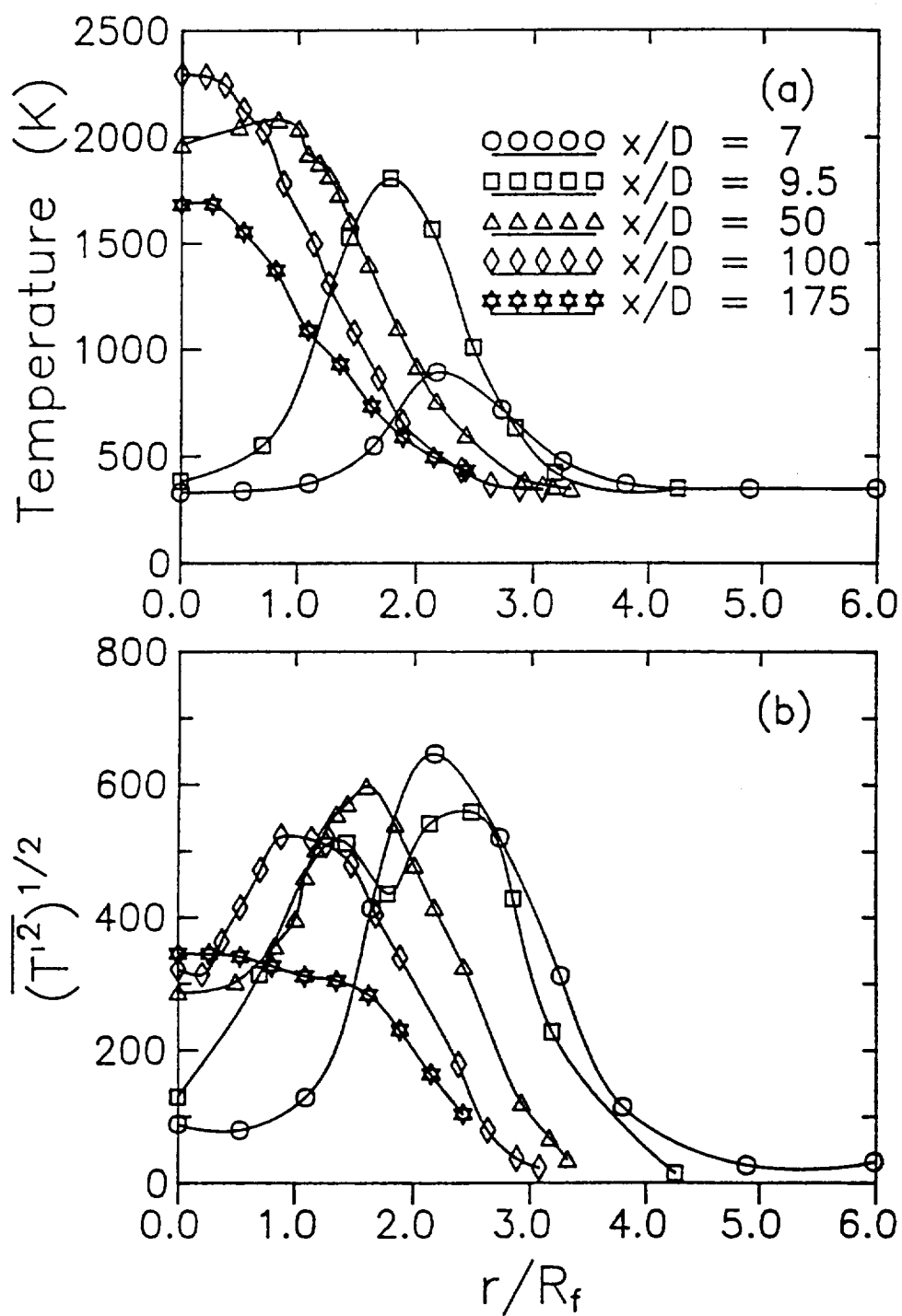
Fig. 24 Radial profiles of mean and rms temperatures at five downstream locations.

Fig. 24a). The lower mean flame temperatures at the lifted zone near the nozzle are mainly due to turbulent mixing without reaction and superequilibrium radical concentrations (discussed later).

Similar trends can be seen in the rms temperature profiles (see Fig. 24b). The peak rms temperature value (650 K) at $x/D = 7$ is higher than the others. This is due to the flame base fluctuations and intermittency effects. Both peak values for mean and rms temperature lie at the same radial position for $x/D = 7$ and likewise for $x/D = 175$. For $x/D = 50$ and 100 the peak rms temperature occurs farther out in the outer shear layer region, and a double-peak appears at $x/D = 9.5$. These findings are in agreement with Raman measurements by Pitz and Drake (1986) and Drake et al. (1986). They found the peak mean and rms temperatures appeared respectively at $r/R_f \approx 1.3$ and 1.6 for $x/D = 50$, and a double-peak rms temperature appeared at $x/D = 10$ in a turbulent H_2 co-flowing with air jet flame ($Re_D = 8500$, $D = 3.2$ mm).

The normalized mean and rms mixture fraction radial profiles are shown in Fig. 25 for seven axial locations. At each downstream location, the radial mixture fractions are normalized by their centerline values. In Fig. 25a, all the normalized points lie on a single curve which implies that the mean mixture fraction profiles are self-similar in the lifted diffusion flame. Fig. 4b indicates that the normalized rms mixture fraction profiles are not self-similar in the flame. These findings are also found in turbulent reacting and non-reacting jets.

The centerline mixture fractions (f_0) are: 0.28621, 0.18209, 0.09550, 0.05918,
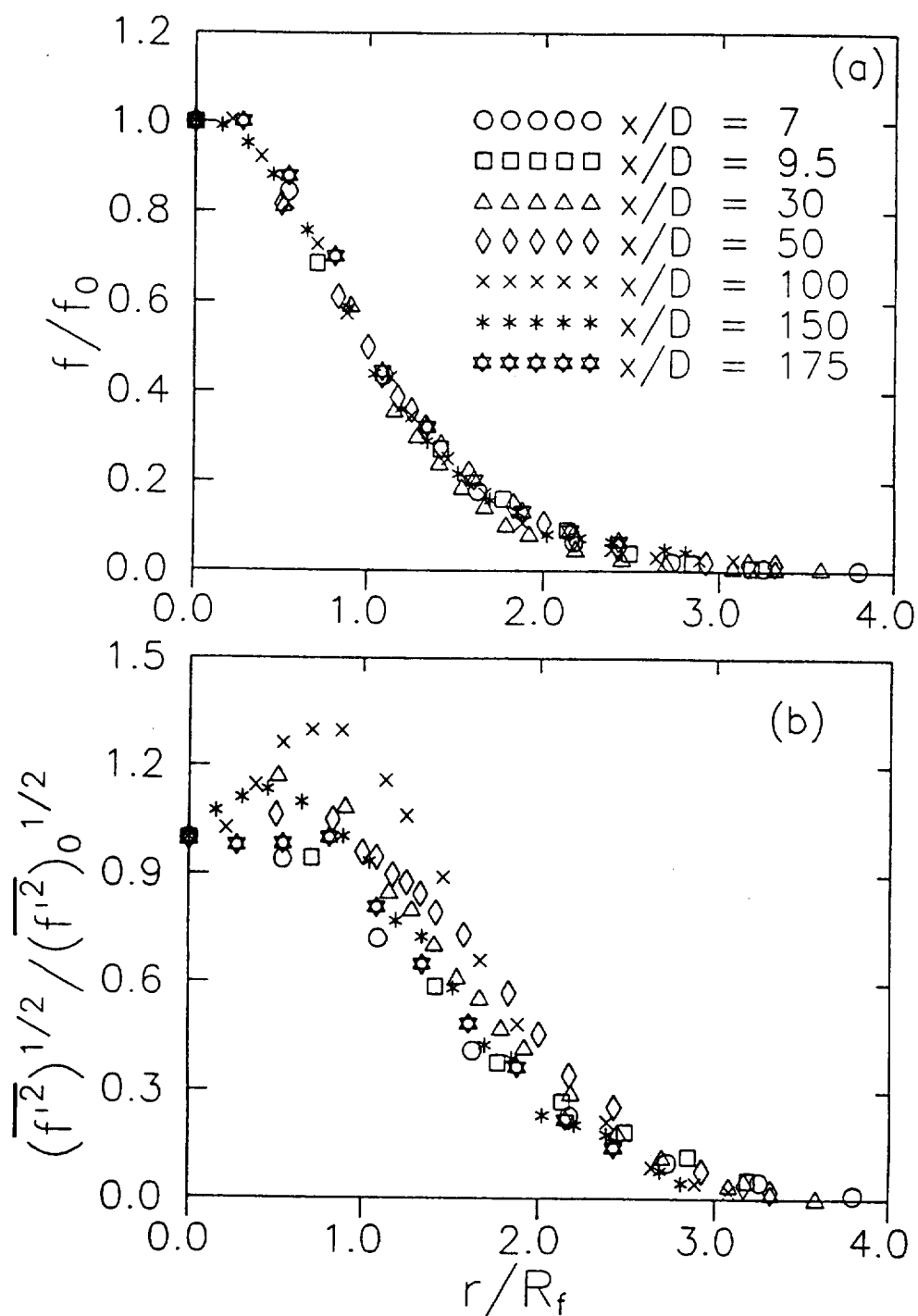
Fig. 25 Normalized mean and rms mixture fractions radial profiles.

0.03228, 0.02128, 0.01747 for the seven downstream locations. Thus, the flame length based on the mean mixture fraction is ~103 diameters. However, instantaneous stoichiometric mixture fractions are found as far as 175 diameters downstream.

Radial profiles of the mean values of H_2, O_2, N_2, H_2O, and OH mole fractions are shown in Figs. 26-29 for seven downstream locations. In all cases, the peak mole fractions of OH and H_2O appear at the same radial position where the maximum mean temperature occurs. Note that at the center of the flame base ($x/D = 7$, $r/R_f = 0$) and 2.5D farther downstream ($x/D = 9.5$, $r/R_f = 0$) a significant amount of O_2 exists (see Fig. 26). The nonreactive O_2 concentration has the N_2/O_2 ratio about the same as room air (3.76). This premixing process in a lifted flame is not seen in an attached turbulent flame at $x/D = 10$ (Drake et al., 1986). Scholefield and Garside (1949) used flow visualization to demonstrate that for the positions between the base of the flame and the burner head a turbulent mixing region exists which is very similar to that for the unignited, isothermal flow. Moving farther downstream, the H_2 concentration decreases. At $x/D = 150$ and 175 (see Figs. 28b and 29), the H_2 fuel has burned out and the mole fraction profiles are flatter than these in the lifted zone (see Fig. 26) and in the slow three-body recombination zone (see Fig. 27).

For turbulent jet diffusion flames into still air, the flame length is defined as the length on the axis from the tip of the burner to the point having a stoichiometric composition. The mean stoichiometric point on the axis of this lifted flame is found at $x/D \approx 103$ for a Froude number of 2.4×10^7. This flame length appears to be about the same as that of Bilger and Beck (1975) for a Froude number of 1.5×10^6.
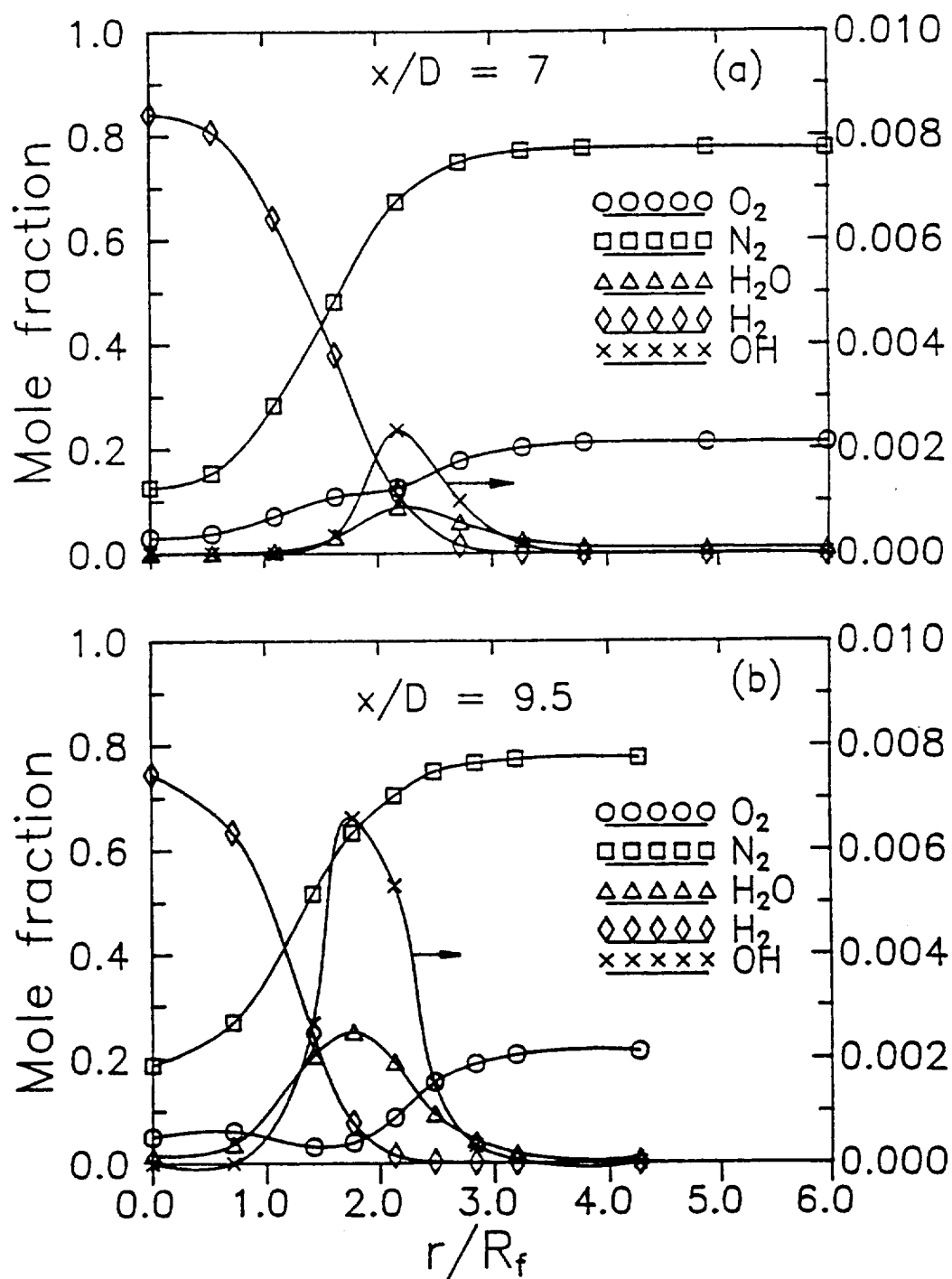
Fig. 26 Radial profiles of major and minor species mole fractions at x/D = 7 and 9.5.
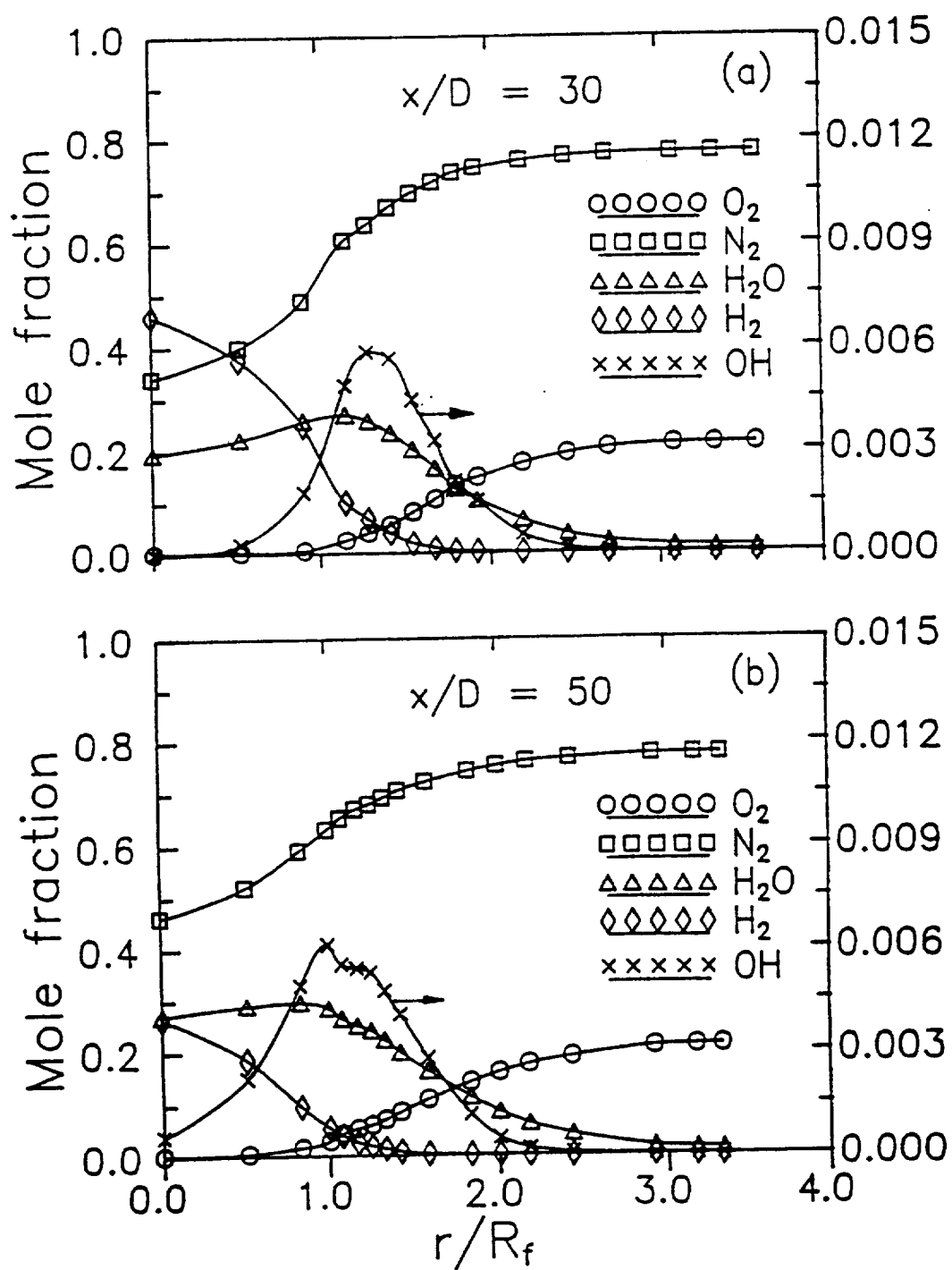
Fig. 27 Radial profiles of major and minor species mole fractions at x/D = 30 and 50.
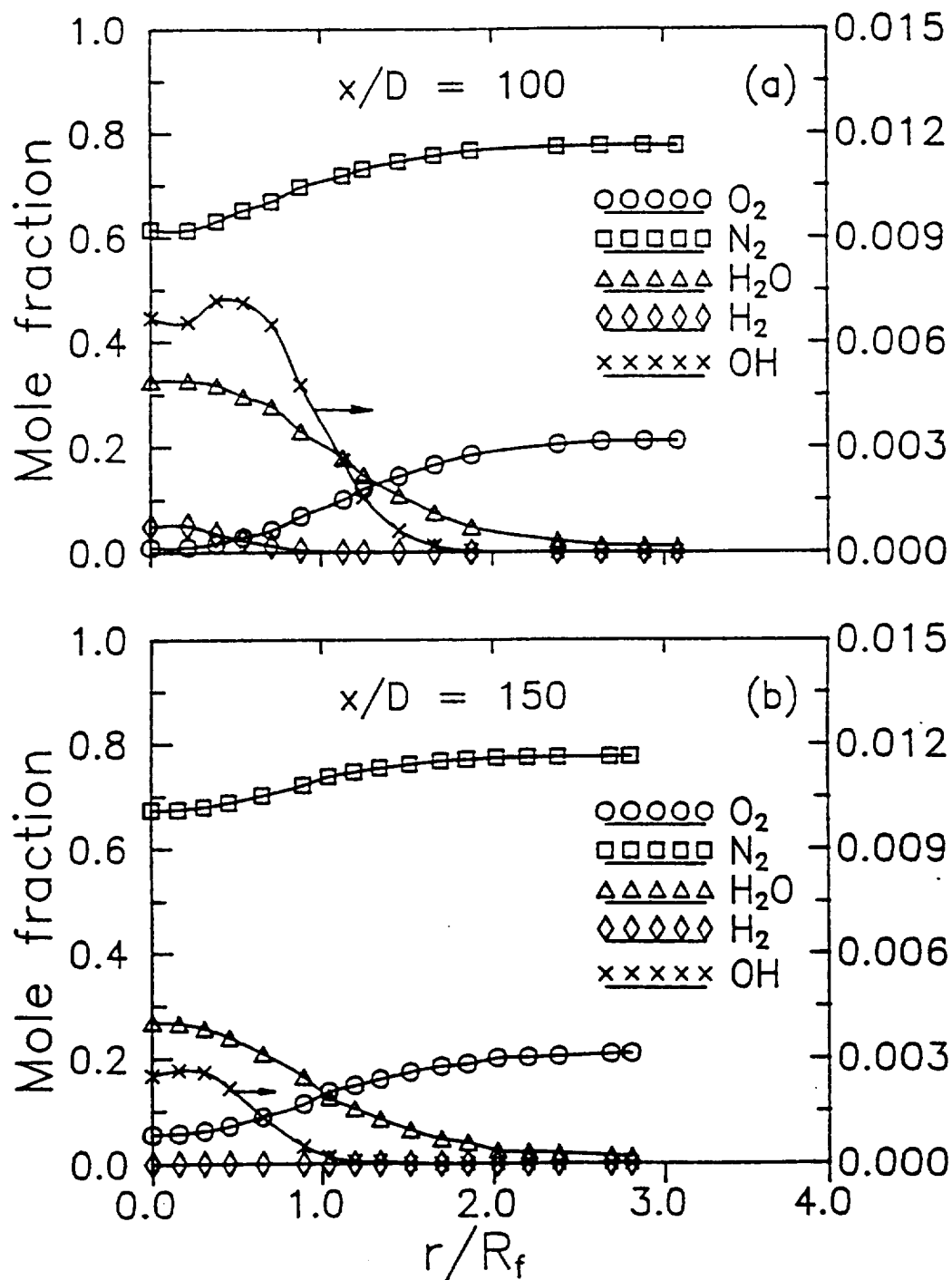
Fig. 28 Radial profiles of major and minor species mole fractions at x/D = 100 and 150.
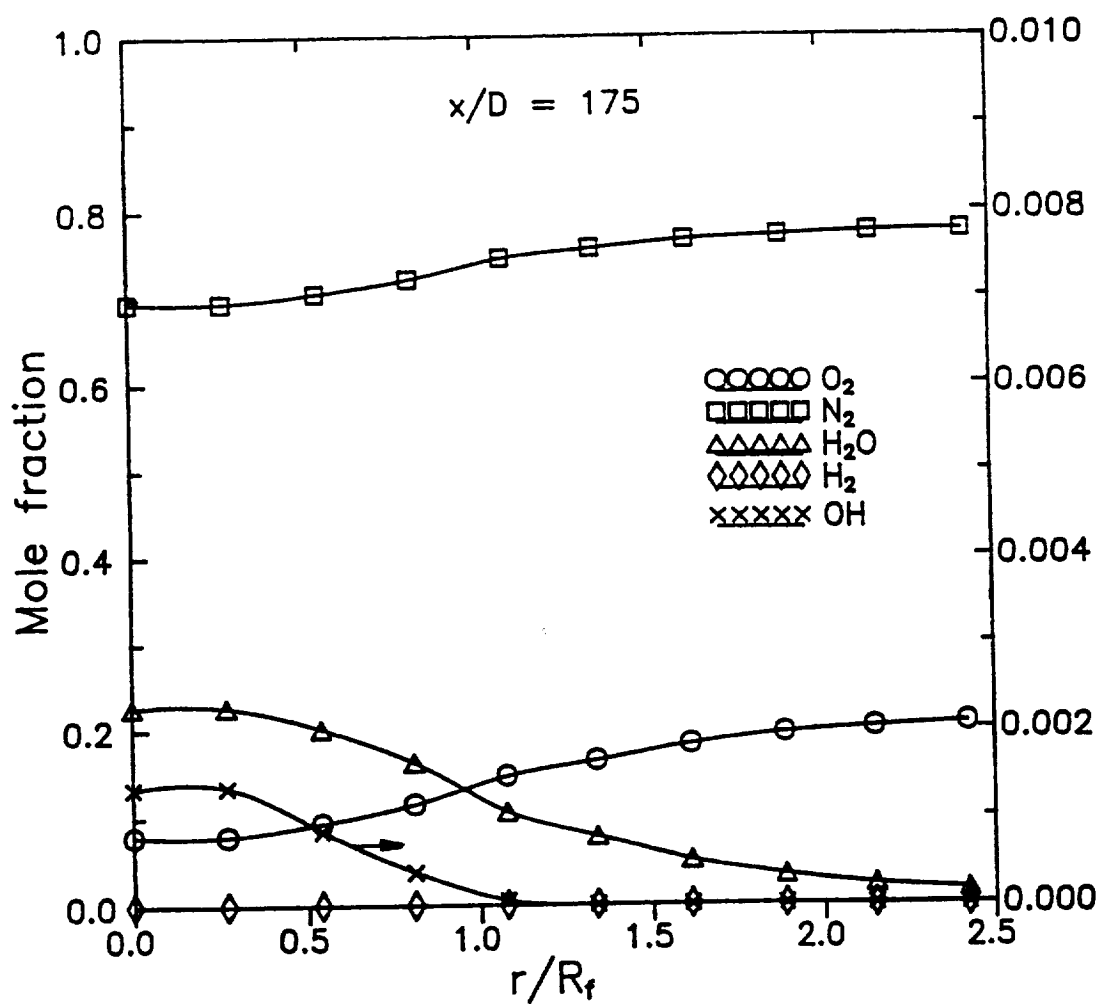
Fig. 29 Radial profiles of major and minor species mole fractions at x/D = 175.

This comparison indicates that buoyancy effects are unimportant for this lifted flame.

Fluid Mechanical Scales

The required spatial and temporal resolutions for the Raman scattering system are estimated by calculating the relevant turbulence length and time scales in the flame. Goulard et al. (1976) suggested that the spatial and temporal resolutions of the experimental systems are adequate if they are less than ~3 times the Kolmogorov scales. Recently, in a study of the behavior of scalar interfaces of a liquid jet (water), Miller and Dimotakis (1991) suggested that the required spatial resolution is about 25 times the Kolmogorov length scale for resolving the velocity field spatial scale where the action of viscosity becomes important. In a study of spatial-averaging effects in Raman/Rayleigh measurements, Mansour et al. (1990) estimated that a measurement would capture at least 85% of mean and rms scalars for the turbulent Reynolds number range from 50 to 500 if the probe length is 0.3 times the integral length scale.

To determine the required spatial resolution for the present turbulent flame measurements, the flame thickness must also be considered. For example, if the measurement is in the wrinkled flame region (laminar flame thickness less than Kolmogorov length scale) spatial-averaging effects may still occur even if the spatial resolution is less than ~3 times the Kolmogorov length scale. On the other hand, if the measurement is in the distributed reaction zone (Kolmogorov length scale less than laminar flame thickness) the spatial resolution of the system may be adequate

even if it is greater than ~3 times the Kolmogorov length scale.

The smallest velocity scale in a turbulent flow is the Kolmogorov length scale given by (Kolmogorov, 1941):

$$\eta = (v^3 / \varepsilon)^{1/4} \qquad (5\text{-}1)$$

where v is the kinematic viscosity and ε is the turbulent kinetic energy dissipation rate. The kinematic viscosity is determined at each radial location using measured temperature and species mole fractions ($v \propto T^{1.5}$ and $v = \Sigma \chi_i v_i$). The dissipation rate can be approximated by:

$$\varepsilon = u^3{}_{rms} / L \qquad (5\text{-}2)$$

where u_{rms} is the turbulent fluctuating velocity and L is the integral length scale. The integral length scale in turbulent H_2/air diffusion flames is given by (Starner and Bilger, 1980):

$$L = 0.7 \, R_u \qquad (5\text{-}3)$$

where R_u is the radius at which the velocity is halfway between the centerline and freestream value.

The smallest scalar scale in the flow is the Batchelor scale, λ_B. The Batchelor scale is given by (Batchelor, 1959):

$$\lambda_B = (v \, k^2 / \varepsilon)^{1/4} = \eta / (Sc)^{1/2} \qquad (5\text{-}4)$$

where Sc is the molecular Schmidt number (kinematic viscosity divided by species diffusivity k). For gas flows, where Sc $\approx$ 1, the Batchelor scale is about the same as

the Kolmogorov scale. Thus, the Kolmogorov length scale is used for estimating the required spatial resolution for the Raman system.

The required temporal resolution of the Raman system is estimated from the Kolmogorov time scale, τ_u, given by:

$$\tau_u = (v \ / \ \varepsilon)^{1/2} \tag{5-5}$$

Since the velocities are not measured in this flame, they are estimated using the jet exit velocity (680 m/s) and the similarity law along with an assumed Gaussian velocity profile by (Chen and Rodi, 1980):

$$\frac{U}{U_c} = \exp(-K_u \ (r/x)^2) \tag{5-6}$$

and

$$U_c = 6.3 \left(\frac{\rho_0}{\rho_a}\right)^{1/2} \left(\frac{D}{x}\right) U_0 \tag{5-7}$$

where U_c is the jet centerline velocity, U_0 is the jet exit velocity, ρ_0 is the measured local density for this calculation, ρ_a is the ambient air density, D is the jet exit diameter, x is the axial distance downstream of the jet nozzle, K_u is a constant with a value of 94, and r is the radius of the nozzle.

The half-radius of the velocity, R_u, is also estimated using the density ratio suggested by Chen and Rodi (1980). The values of R_u are found very close to that of R_f. The turbulent fluctuating velocity, u_{rms}, is assumed to be 10% of the local velocity, U. Fluid mechanical scales for x/D = 7, 30, and 50 are summarized in

Table 4. The temporal resolution of the Raman system (20 ns) is well within the requirement for this experiment. The spatial resolution of the Raman system (~0.4 mm) does not meet the criterion (~3η) for r/R_f = 0 to 1.63 at x/D = 7. However, the measurement will capture at least 85% of the mean and rms scalars based on the estimation of Mansour et al. (1990). The spatial resolution is adequate for r/R_f > 1.63 and for locations at farther downstream (x/D>7) as the velocities decay.

Identification of Mixing and Finite-Rate Chemistry Effects

A major objective of this research is to study the interaction of turbulent mixing and chemical reaction as well as finite-rate chemistry effects in turbulent diffusion flames. To identify these important processes, the instantaneously measured quantities for four locations in the flame (solid symbols in Fig. 23) are compared to equilibrium values as the mixture fraction is determined simultaneously with each laser shot.

The interactions of turbulent mixing and chemical reaction can be characterized by the Damköhler number, the ratio of a turbulent mixing time to a chemical reaction time, Da = τ_t/τ_c. For Da >> 1 chemical reaction is fast compared to turbulent mixing, and chemical equilibrium is approached everywhere in the flow. For the case of Da << 1, turbulent mixing is rapid compared to chemical reaction, and the flow approaches the limit of a homogeneous, reacting mixture. When Da ≈ 1, turbulent mixing and chemical reaction are competitive, and departures from chemical equilibrium are expected to exist in the flow.

Table 4. Fluid mechanical scales in the subsonic flame.

x/D	r/R$_f$	U, m/s	T, K	$v \times 10^4$, m^2/s	η, mm	τ_u, μs	L, mm	l/L
7	0.00	269.3	330	1.10	0.015	2.0	1.4	0.3
	0.54	226.5	337	1.09	0.017	2.5	1.4	0.3
	1.09	134.6	373	1.06	0.024	5.5	1.4	0.3
	1.63	56.6	550	1.28	0.053	22.0	1.4	0.3
	2.17	16.8	892	1.38	0.140	141.2	1.4	0.3
	2.72	3.6	717	0.65	0.255	1002.4	1.4	0.3
	3.26	0.5	475	0.32	0.626	12291.2	1.4	0.3
30	0.00	41.4	1721	8.30	0.353	150.1	4.2	0.1
	0.51	29.0	1800	7.72	0.436	246.1	4.2	0.1
	0.90	14.0	1919	6.62	0.671	680.3	4.2	0.1
	1.15	6.9	1966	4.52	0.857	1625.3	4.2	0.1
	1.28	4.5	1896	3.78	1.026	2788.3	4.2	0.1
	1.41	2.8	1797	3.07	1.246	5048.7	4.2	0.1
	1.54	1.7	1612	2.35	1.490	9457.4	4.2	0.1
	1.67	1.0	1402	1.79	1.839	18913.2	4.2	0.1
50	0.00	26.6	1965	7.11	0.507	361.4	7.0	0.06
	0.50	17.9	2046	6.25	0.620	613.8	7.0	0.06
	0.83	8.8	2080	4.89	0.874	1560.5	7.0	0.06
	1.00	5.5	2040	4.04	1.087	2929.3	7.0	0.06
	1.08	4.1	1920	3.43	1.182	4078.3	7.0	0.06
	1.17	3.0	1878	3.10	1.370	6053.9	7.0	0.06
	1.25	2.2	1820	2.85	1.633	9364.1	7.0	0.06
	1.33	1.6	1733	2.56	1.947	14809.8	7.0	0.06

l = 0.4 mm (spatial resolution of the Raman system).

The effects of Damköhler number on turbulent shear layers (Mungal and Frieler, 1988) and on superequilibrium OH concentration in turbulent diffusion flames (Barlow et al., 1990) have been investigated. Barlow et al. (1990) reported that the OH concentrations have superequilibrium values for the Damköhler numbers ($\tau_t/\tau_{c,3\text{-body}}$) less than unity. To calculate the turbulent mixing time for the present lifted jet flame, the large-eddy-turnover time, which was suggested by Mungal and Frieler (1988) and interpreted for the jet flames by Barlow et at. (1990), is used:

$$\tau_t = \delta_{1/2} / (U - U_\infty) \tag{5-8}$$

where $\delta_{1/2}$ is the width (full width, half maximum) of the jet velocity profile, U is the local velocity which is calculated from Eq. (5-6), and U_∞ is the mean co-flow velocity which is assumed to be zero for the still air.

For a hydrogen-air diffusion flame, a seven-step reaction mechanism is generally used to account for two-body and three-body reactions (Janicka and Kollmann, 1979). Magre and Dibble (1988) suggested that for a pure hydrogen-air flame the two-body shuffle reactions

$$H + O_2 \rightarrow OH + O \tag{R1}$$

$$O + H_2 \rightarrow OH + H \tag{R2}$$

$$H_2 + OH \rightarrow H_2O + H \tag{R3}$$

$$OH + OH \rightarrow H_2O + O \tag{R4}$$

have a time scale of ≈ 18 μs. They used the stirred reactor code of Glarborg et al.

(1986) to calculate the minimum residence time of ≈ 20 μs for a perfectly stirred reactor with stoichiometric reactants of 22% argon in hydrogen plus air initially at 300 K and then estimated the time scale for undiluted hydrogen-air. Radicals that are produced via rapid two-body reactions will decay toward equilibrium via slow three-body recombination reactions:

$$H + OH + M \rightarrow H_2O + M \qquad\qquad (R5)$$

$$H + O + M \rightarrow OH + M \qquad\qquad (R6)$$

$$H + H + M \rightarrow H_2 + M \qquad\qquad (R7)$$

These recombination reactions have a characteristic time scale of ≈ 3 ms in an atmospheric flame (see Chapter IV).

The calculated turbulent mixing times and Damköhler numbers are listed in Table 5. In the center core of the lifted region ($x/D=7$, $r/R_f=0$), the chemical reaction times must be much greater than the turbulent mixing times due to no chemical reactions (T=300 K). Hence, Damköhler numbers ($Da_{2\text{-body}}$ and $Da_{3\text{-body}}$) must be much less than unity. For the location at $x/D = 7$, $r/R_f = 2.17$ where reacted, partially reacted, and unreacted conditions coexist. These Damköhler numbers are maximum found at this location.

In the lifted flame region, scatter plots of temperature, OH mole fraction, and major species mole fractions for an ensemble of 1000 independent single-shot measurements are shown in Figs. 30-33. The measured quantities are plotted versus local mixture fraction. The solid curves represent the adiabatic equilibrium

Table 5. Damköhler numbers for the subsonic flame.

x/D	r/R$_f$	U (m/s)	τ_t (ms)	Da$_{2-body}$	Da$_{3-body}$
7	0	269	0.0148	<< 1	<< 1
7	2.17	17	0.24	13	0.08
50	0.5	18	1.1	62	0.37
175	0	9	7	389	2.3

Fig. 30 Scatter plot of temperature and OH mole fraction at x/D = 7, r/R$_f$ = 0.
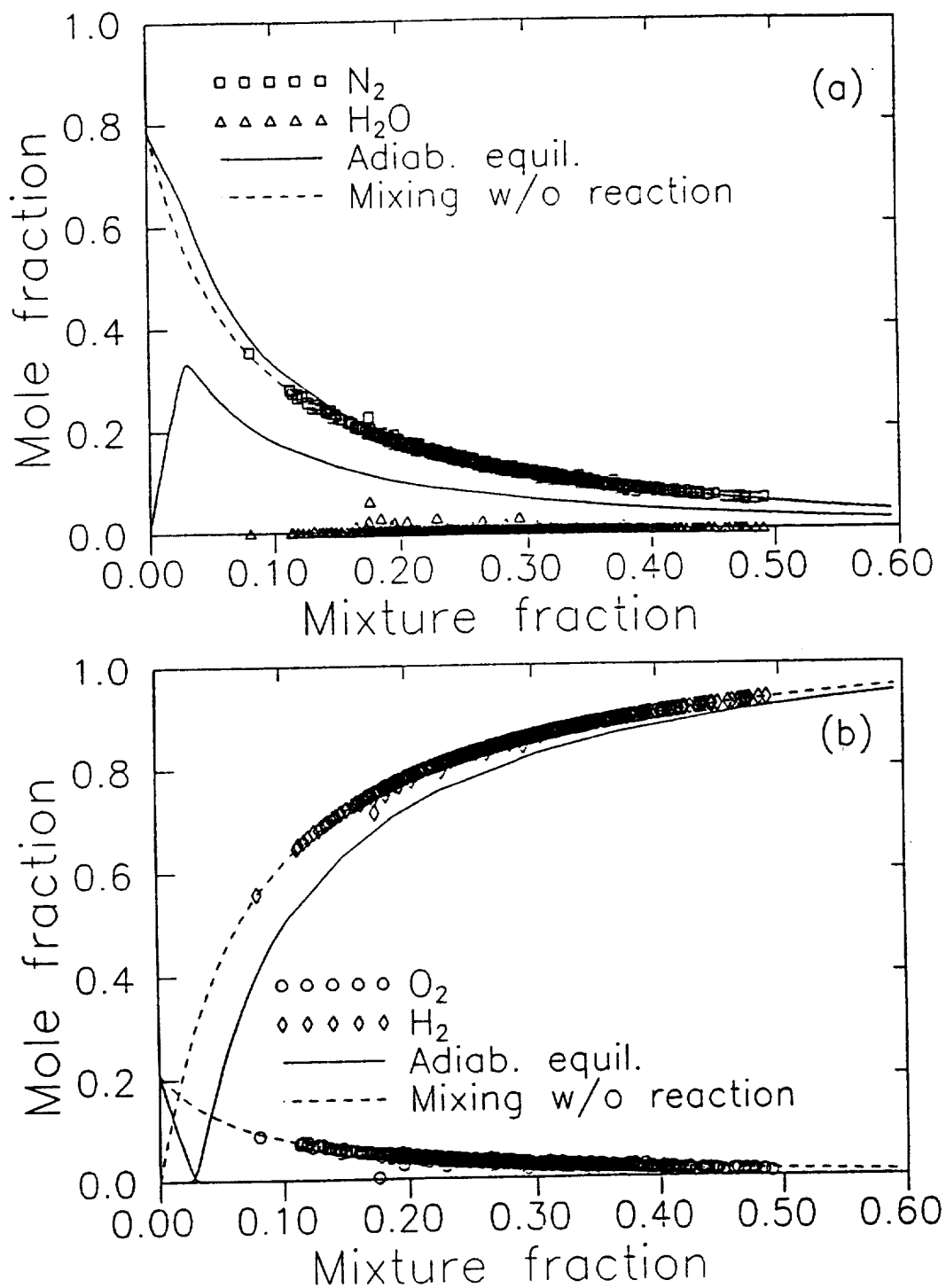
Fig. 31 Scatter plot of major species mole fractions at x/D = 7, r/R$_f$ = 0.
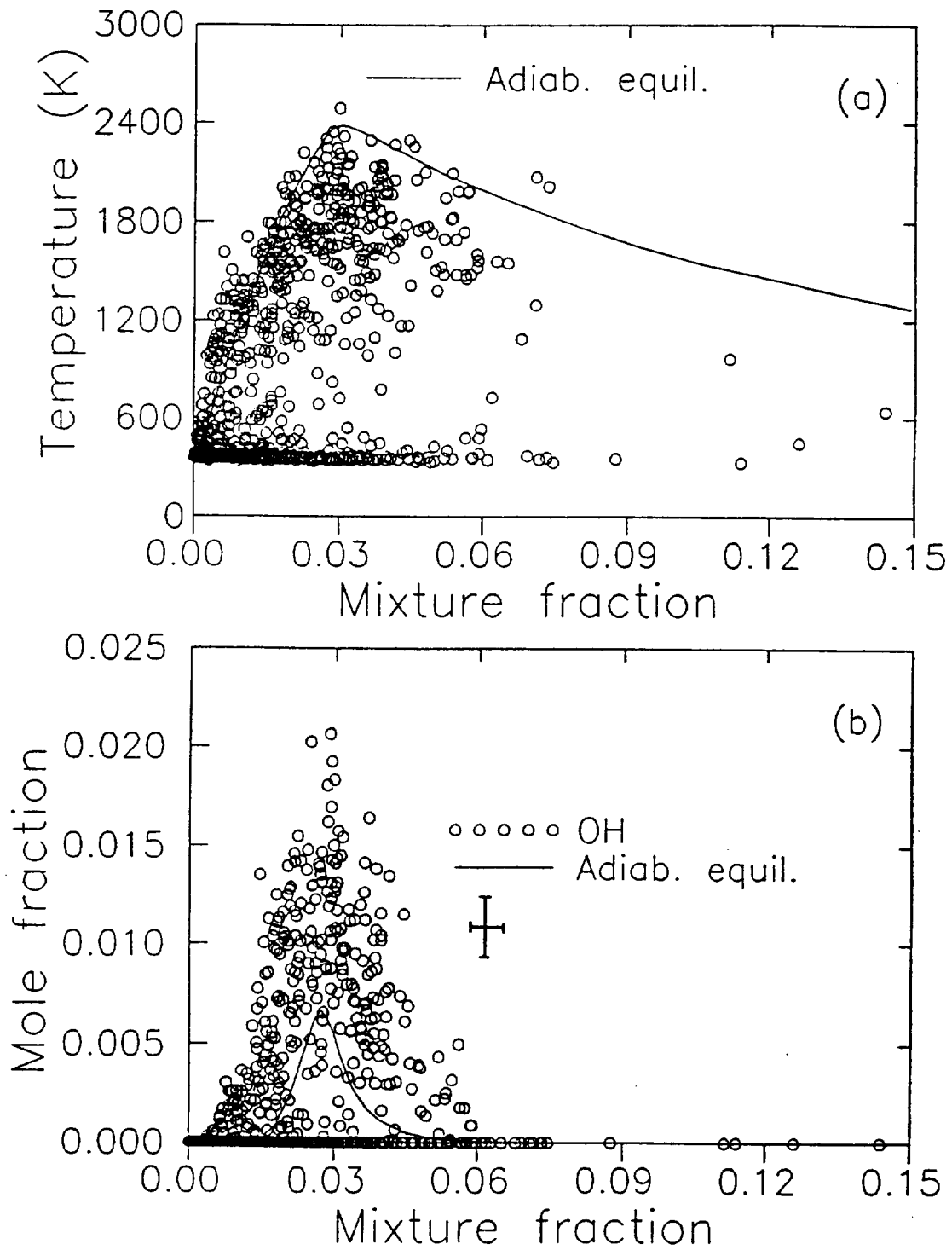
Fig. 32 Scatter plot of temperature and OH mole fraction at x/D = 7, r/R$_f$ = 2.17.
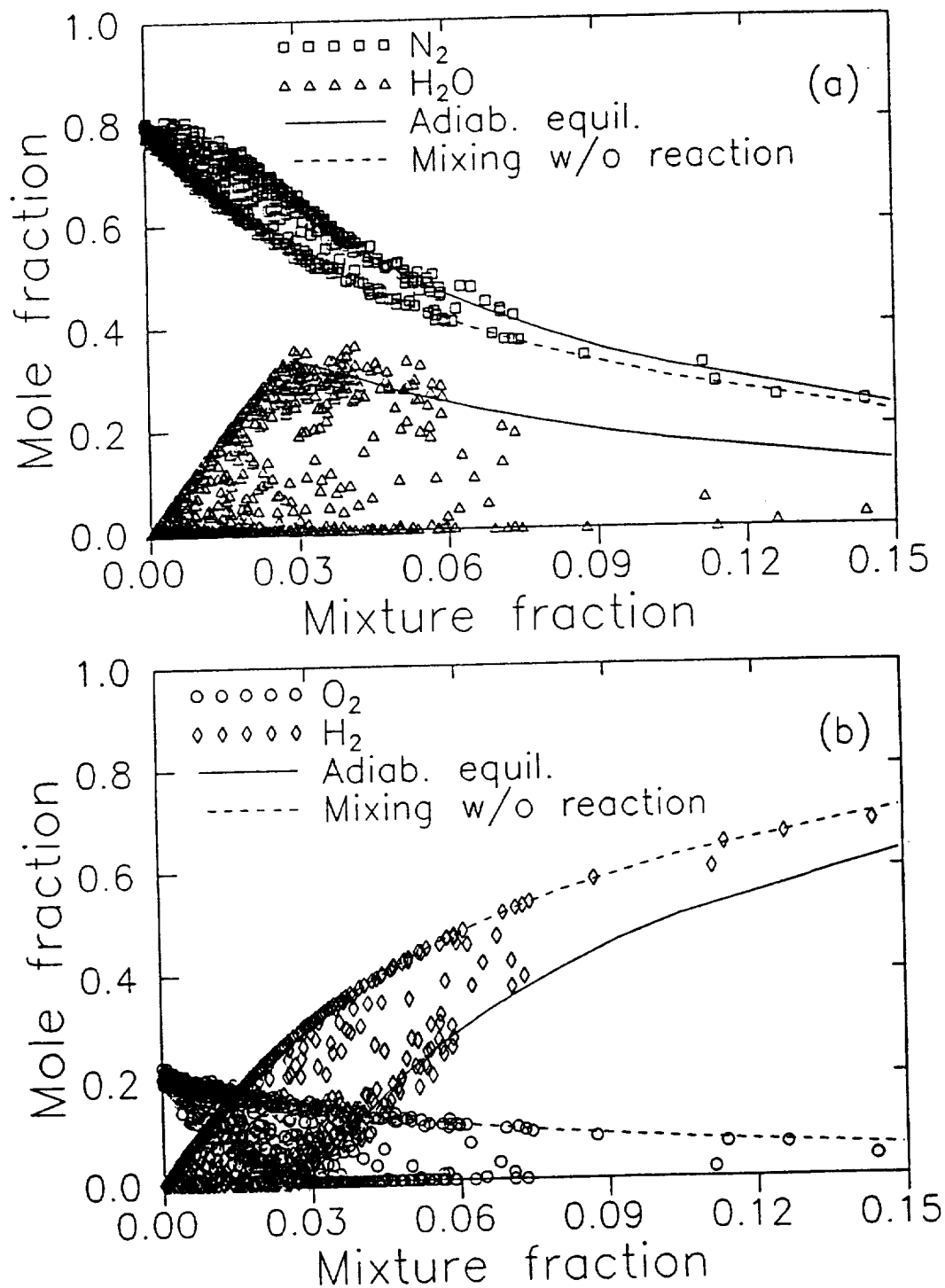
Fig. 33 Scatter plot of major species mole fractions at x/D = 7, r/R$_f$ = 2.17.

conditions (infinite reaction rate, Da$>>1$), and the dashed curves are for mixing without reaction (Da$<<1$).

In the center of the lifted flame base (x/D = 7, r/R_f = 0), the temperature is essentially room temperature (see Fig. 30a), and the H_2, O_2, and N_2 mole fractions are on mixing without reaction curves for f$\approx$ 0.1 to 0.5 (see Fig. 31). No H_2O combustion product (see Fig. 31a) or intermediate OH radical (see Fig. 30b) is produced. At this location, the fuel/air mixture is in a rich unignited condition. The unreacted O_2 concentration in the center of the lifted flame base seen earlier (see Fig. 26) is due to air mixing upstream of the flame base without reaction. Here the turbulent mixing time is much less than the two-body reaction time (Da$_{2\text{-body}}<<1$), so the fuel and air are premixed without reaction. This finding shows that in this region of the present flame turbulent mixing affects chemical reaction and results in departure from the classical "fast chemistry" assumption.

The outer region of the lifted flame is shown in scatter plots (see Figs. 32 and 33) for the location at x/D = 7, r/R_f = 2.17 where reacted, partially reacted, and unreacted conditions coexist. In Fig 32a, the scatter points along the line at 300 K correspond to mixing without reaction, while the scatter points close to but below the equilibrium curve correspond to nearly complete reaction.

Scatter points near but below the equilibrium curve are caused by the slow three-body recombination of OH radicals (Da$_{3\text{-body}}<1$) which depresses flame temperature below the equilibrium value. Some scatter points above the equilibrium curve may be either due to experimental error or due to differential diffusion. The

rest of the intermediate temperature points are either due to flame extinction/ignition phenomena or due to spatial averaging of thin reaction zones. Gutheil and Williams (1989) calculated the reaction zone to be ~0.2 mm thick for highly stretched flames near extinction (strain rate of 6000 s^{-1}) in counterflow hydrogen-air diffusion flames. The experimental results are very similar to the Raman scattering combined with LIF measurements by Barlow et al. (1989) who measured a lifted hydrogen co-flowing air jet flame at a different exit velocity. Although the spatial resolution for the UV Raman system (0.4 mm) through the vertical flame sheets is 2.5 times better than that of the Raman system (1 mm) used by Barlow et al. (1989), averaging across the steep temperature and species concentrations gradients could still occur because of the thin reaction zone. Spatial-averaging effects could reduce the rms fluctuations of the species concentrations and reduce the bimodality of the bimodal PDFs.

Fig. 32b shows the measured OH mole fractions. Experimental points along the baseline correspond to mixing without reaction. Peak OH mole fractions are about 2 times the peak equilibrium value. Calibration results of OH concentration measurements show that the OH concentrations are only slightly higher than the equilibrium values (see Fig. 21b). The uncertainty interval is the measurement in the calibration burner at stoichiometric condition (f=0.0283). By comparing Fig. 32b with Fig. 21b, one can conclude that the measured superequilibrium OH radicals in this lifted flame are mainly due to slow three-body recombination reactions. These superequilibrium OH radicals will decay toward equilibrium values further

downstream via three-body recombination reactions. Explanation for the major species mole fractions (see Fig. 33) is similar to that for temperature.

The probability density functions (pdfs) of mixture fraction and temperature for $x/D = 7$ are shown in Fig. 34. The shape of mixture fraction pdf at the jet center looks Gaussian, but at outer radial positions, the shape becomes non-Gaussian, and a spike appears due to room air (see Fig. 34a). In Fig. 34b, the pdf shapes of temperature at the jet center and at large radii look Gaussian but very narrow. At the intermittent region, the shapes are bimodal (all spikes are cut off at the height of 0.002 ($r/R_f = 1.63, 2.17, 2.72$)).

In the recombination region ($x/D = 50, r/R_f = 0.5$), measurements led to the scatter plots shown in Figs. 35 and 36. The average temperature near stoichiometric condition ($f = 0.0283$) is ~2230 K, which is ~150 K below the adiabatic equilibrium temperature. This temperature depression is caused by the finite-rate chemistry effects of slow three-body recombination reactions of OH radicals ($Da_{3-body} < 1$). Fig. 35b shows that OH mole fraction peak value near stoichiometric condition is about 2-2.5 times the peak equilibrium value, which is a lower value than that observed by Barlow et al. (1989) (2.5-3 times) who measured OH by a quenching corrected LIF technique. The values measured in this experiment are more consistent with superequilibrium values obtained from stretched laminar diffusion flame calculations (2.5 times at a strain rate of 60 s^{-1} obtained from Gutheil and Williams, 1989). The major species mole fractions are on the equilibrium curves because the local time scale of turbulent mixing increases with streamwise distance, allowing the two-body
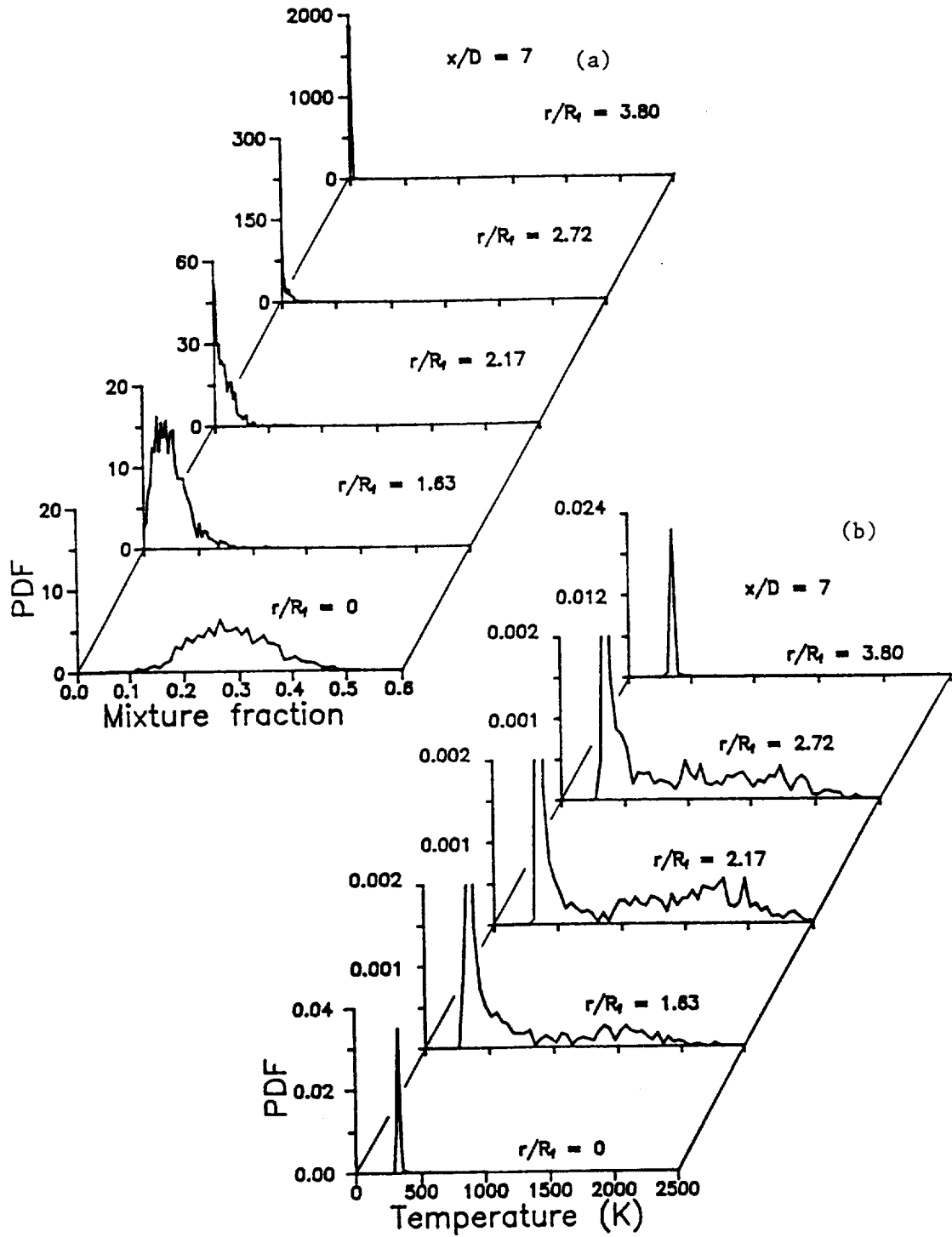
Fig. 34 Probability density functions of mixture fraction and temperature at x/D = 7.
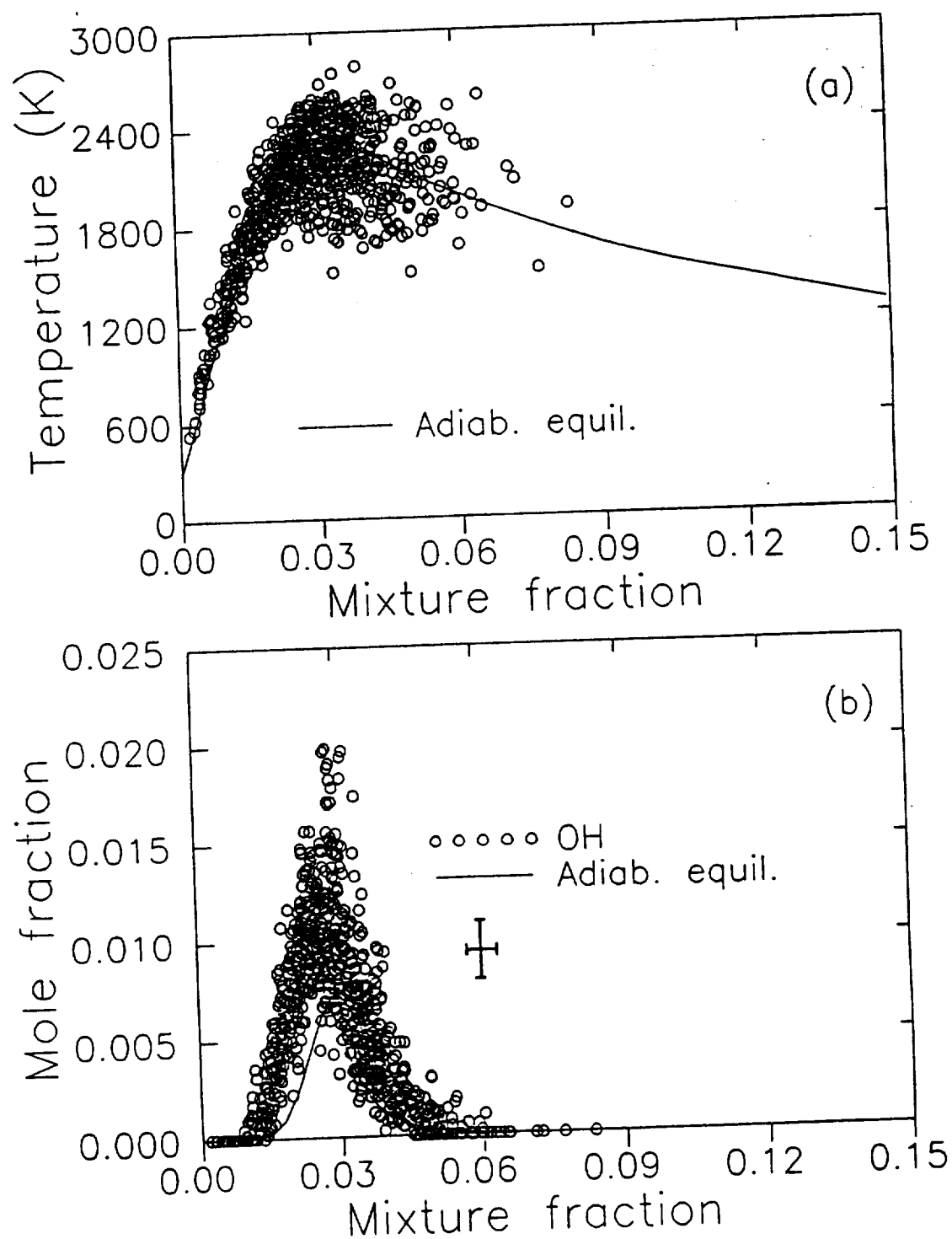
Fig. 35 Scatter plot of temperature and OH mole fraction at x/D = 50, r/R$_f$ = 0.5.
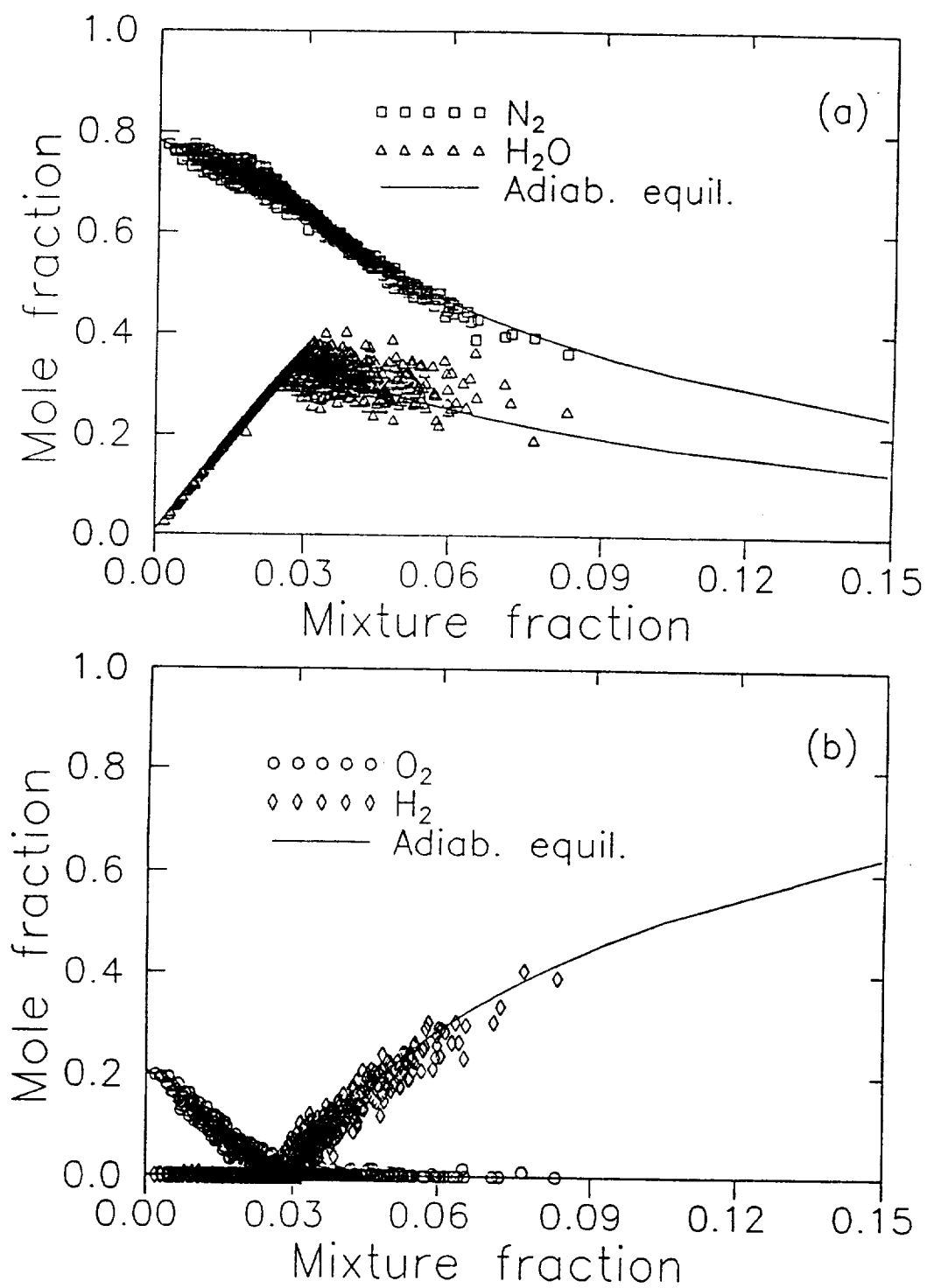
Fig. 36 Scatter plot of major species mole fractions at x/D = 50, r/R_f = 0.5.

reactions to be in partial equilibrium (see Fig. 36).

Far downstream in the flame at $x/D = 175$, $r/R_f = 0$ (see Figs. 37 and 38), the temperature, OH radicals, and major species mole fractions are in equilibrium. The excess OH radicals have completely recombined to equilibrium levels (see Fig. 37b). At this location, the jet velocity decreases to 9 m/s as calculated from Eq. (5-6). As seen in Table 5, the turnover time is 7 ms which is about 2 times longer than the time required for three-body recombination reactions (~3 ms).

Simultaneous measurements of temperature and multi-species concentrations are obtained in a subsonic lifted turbulent diffusion flame by combining spontaneous Raman scattering with laser-induced predissociative fluorescence techniques. These measurements demonstrate that turbulent mixing affects chemical reaction. Finite-rate chemistry effects depress flame temperatures below equilibrium values. The successful application of the UV Raman system to a subsonic reacting flow suggests utilization to measure in a supersonic reacting flow. The studies in the NASA Mach 2 combustor are documented in the next chapter.
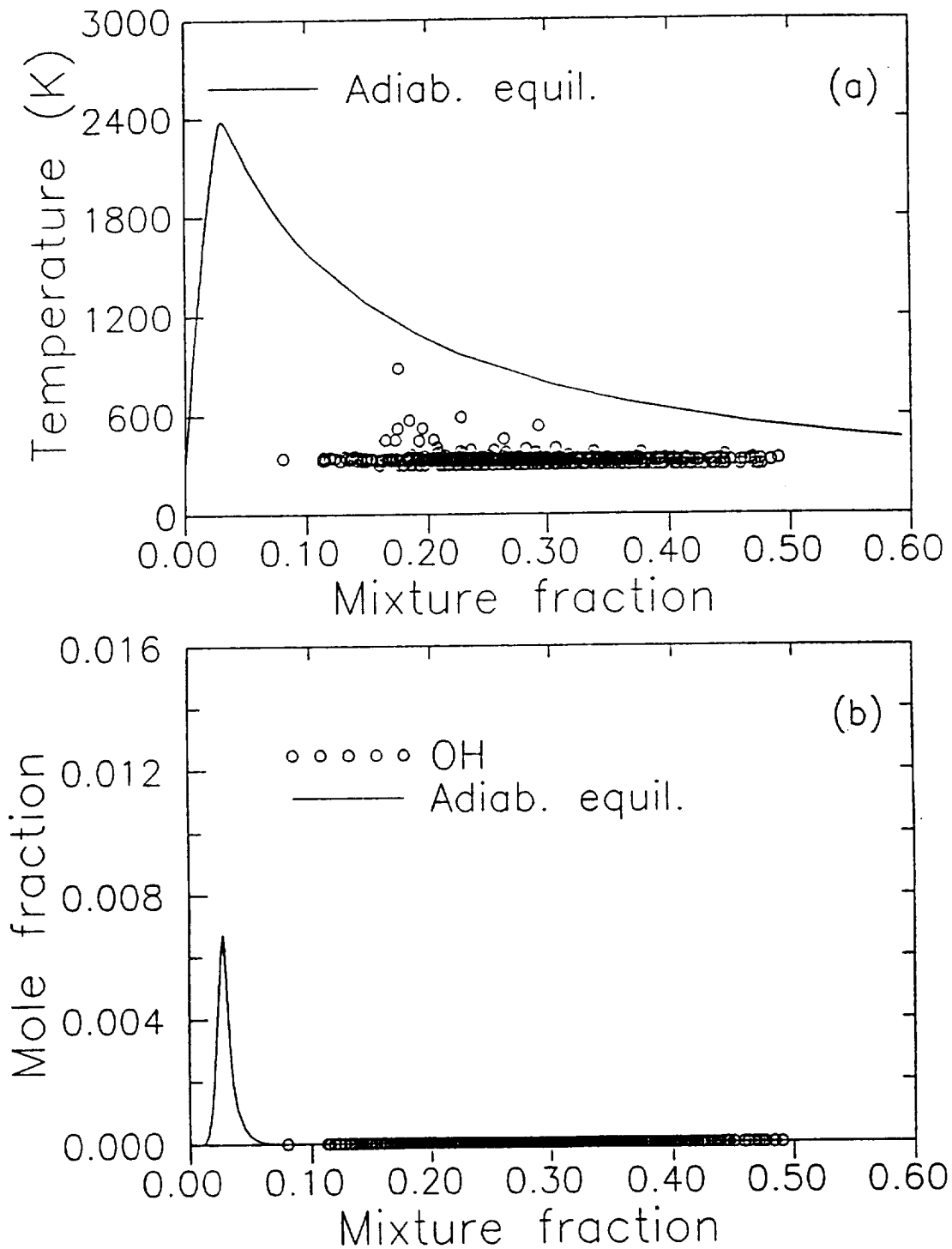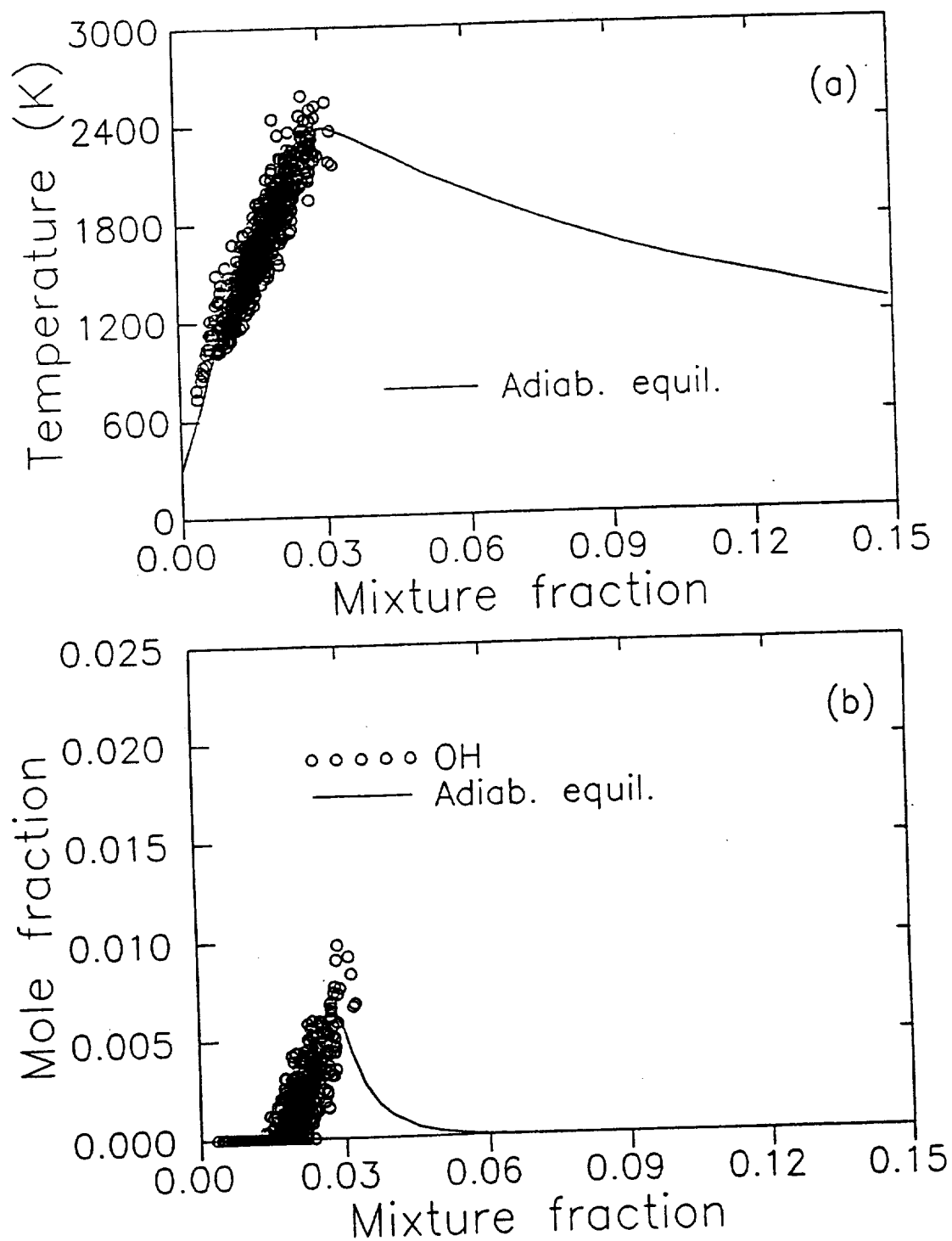
Fig. 37 Scatter plot of temperature and OH mole fraction at x/D = 175, r/R$_f$ = 0.
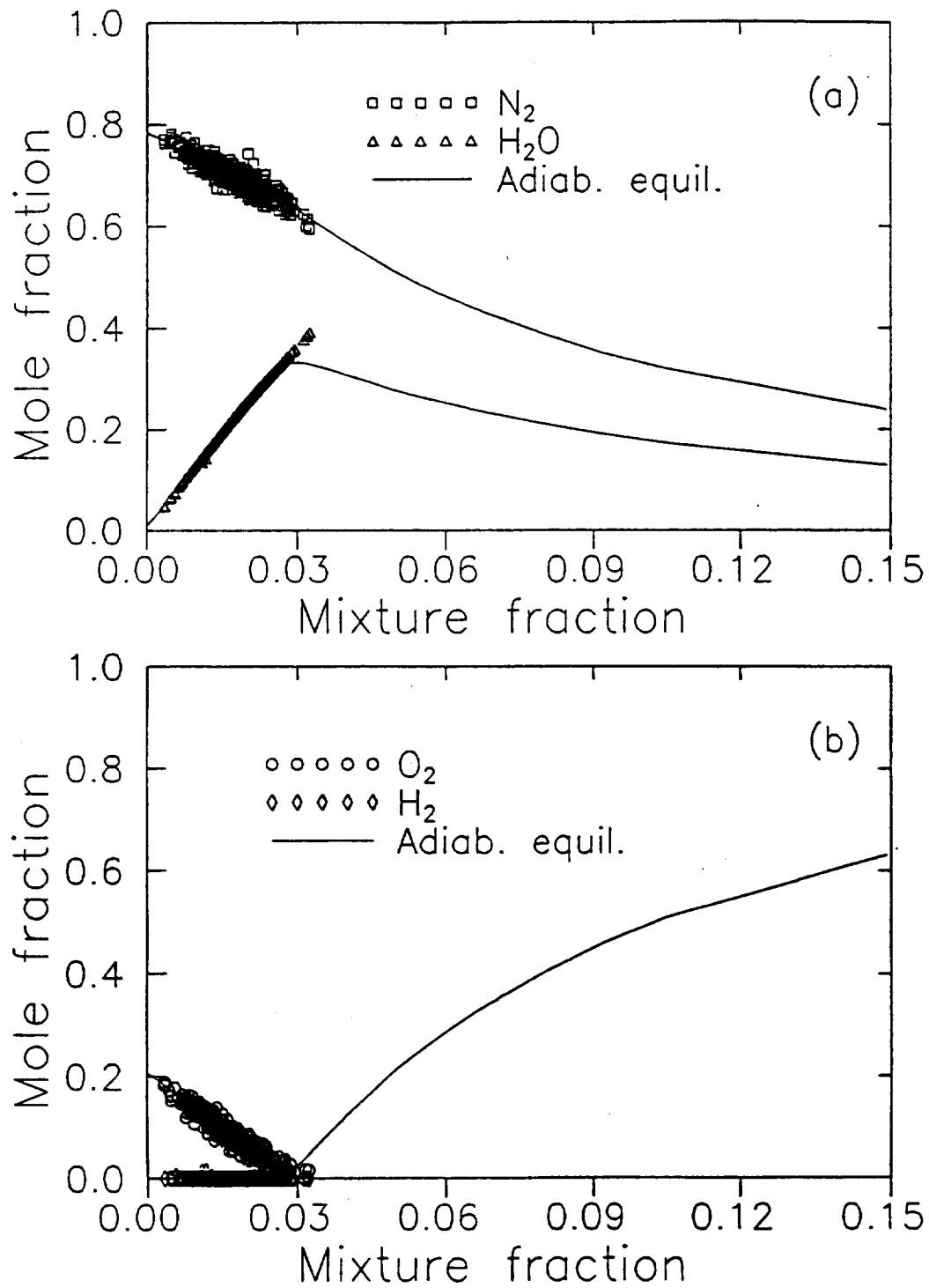
Fig. 38 Scatter plot of major species mole fractions at x/D = 175, r/R$_f$ = 0.

CHAPTER VI

SUPERSONIC FLAME MEASUREMENTS

Supersonic Burner

The UV Raman system has successfully demonstrated that it can provide simultaneous measurements of temperature, and minor and major species concentrations in a subsonic turbulent flame (see Chapter V). To study the interactions of turbulence and chemistry in a supersonic flow, the Raman system was transported to the NASA Langley Research Center where the supersonic burner is located. Prior to supersonic flame measurements, the calibration procedures described in Chapter IV were performed.

A schematic diagram of the supersonic burner is shown in Fig. 39. This supersonic burner provides an annular, axisymmetric jet of hot, vitiated air at Mach 2 concentric to the choked main H_2 fuel jet. Secondary hydrogen is injected into the combustion chamber directly through four injectors (only one of which is shown in the figure), and oxygen enriched air is distributed at the base of the heater by a liner. This hydrogen is burned with the oxygen enriched air, raising the stagnation temperature to the desired operational level, and the vitiated air is accelerated through a convergent-divergent nozzle, exiting into the atmosphere. The walls of the divergent portion of the convergent-divergent nozzle are conical, with a 4.3° half
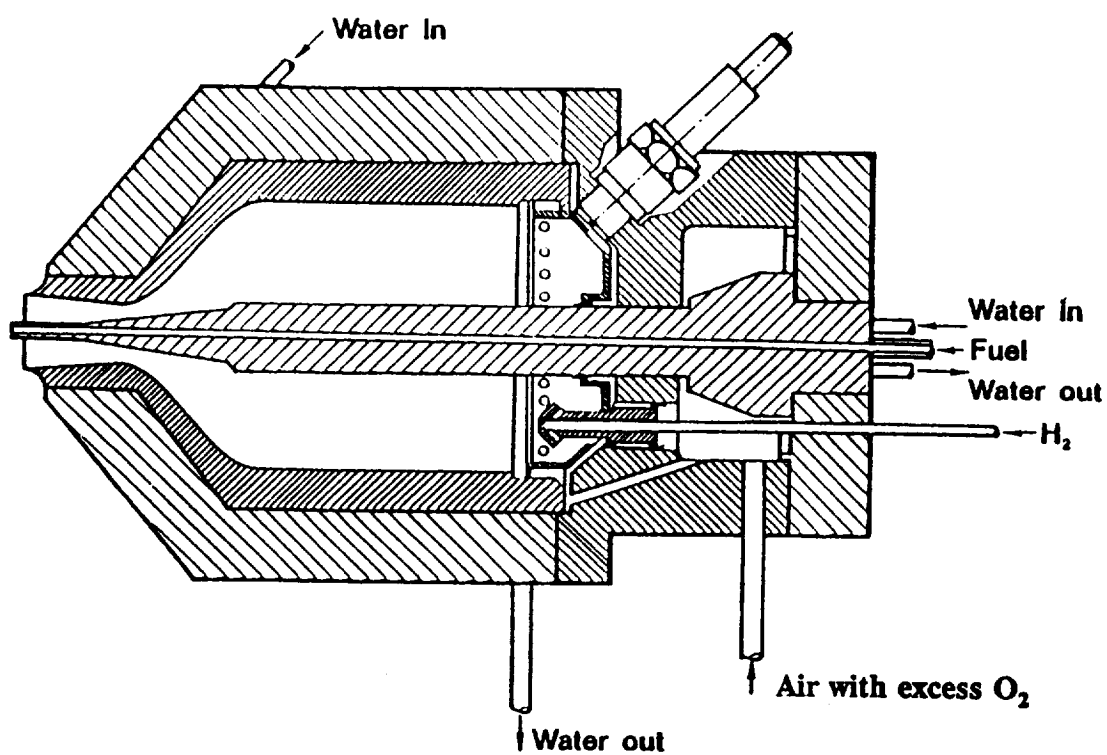
Fig. 39 Schematic diagram of supersonic burner.
(Courtesy of NASA Langley Research Center)

angle. The combustion of the main hydrogen fuel and the vitiated air forms the supersonic flame for this work.

The combustion chamber and the fuel injector are water cooled, and the flowrates of all four gases (hydrogen, air, oxygen, and fuel) are monitored by critical orifices. Cooling water flowrate, cooling water temperature, combustion chamber total pressure, static pressure near the nozzle exit, and fuel pressure in the fuel injector are measured. The gas flowrates are controlled by air actuated needle valves which can be operated manually or by a computer. To operate the supersonic burner for UV Raman measurements, the burner is started under manual control and operation is established near the desired condition. Control is then switched to the computer and the desired running condition is maintained for one to two hours of operation. Computer control is necessary not only to assure constant running conditions, but also to allow personnel to leave the laboratory during data acquisition as the sound levels produced by the supersonic burner exceed 135 db.

This supersonic burner is mounted on a computer controlled motor driven 2-D translation stage and the optical system remains fixed. The parameters and operating conditions of the supersonic burner are given in Table 6. The experimental setup is similar to that for the subsonic flame measurements as shown in Fig. 40. However in the supersonic experiments due to laboratory space limitations, an Acton Research 45° turning mirror was used to direct the high power excimer beam into the supersonic flame. As in the subsonic flame experiments, in order to maximize the laser pulse energy, the laser was operated at 20 Hz.

Table 6. Supersonic burner nominal operating conditions.

Parameter

Air mass flowrate ($\pm$ 2%)	0.0735 kg/s
H_2 mass flowrate ($\pm$ 2%)	0.00173 kg/s
O_2 mass flowrate ($\pm$ 3%)	0.0211 kg/s
Fuel mass flowrate ($\pm$ 3%)	0.000362 kg/s
Nozzle exit I.D.	17.78 mm
Fuel injector I.D.	2.36 mm
Fuel injector O.D.	3.81 mm

Stagnation conditions

Pressure ($\pm$ 4%)	778 kPa
Temperature	1752 K

Vitiated air exit conditions

Pressure	107 kPa
Temperature	1250 K
Mach number	2.0
Velocity	1417 m/s
O_2 mole fraction	0.201
N_2 mole fraction	0.544
H_2O mole fraction	0.255

Fuel exit conditions

Pressure	112 kPa
Temperature	545 K
Mach number	1.0
Velocity	1780 m/s
H_2 mole fraction	1.0
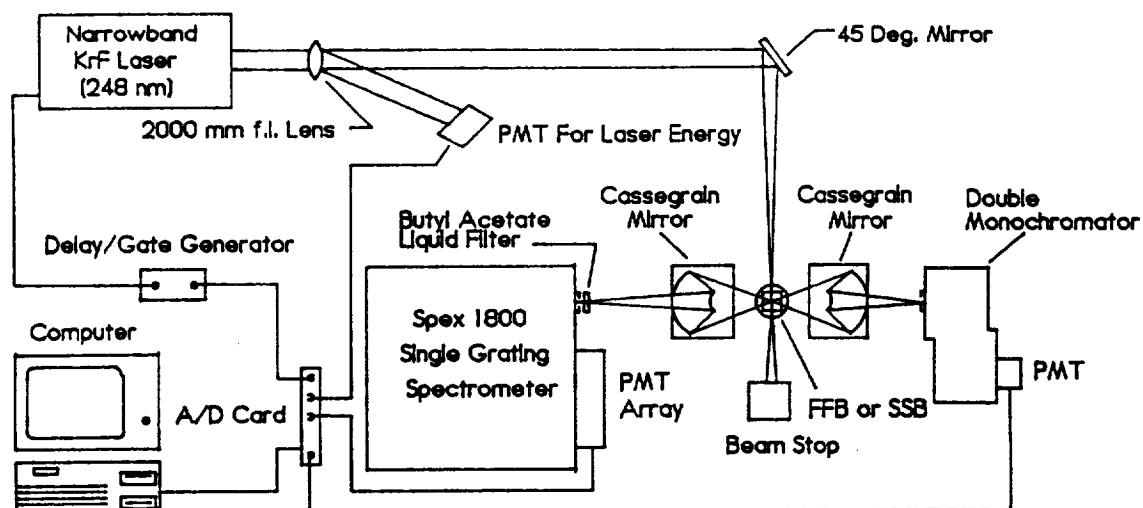
Fig. 40 Schematic diagram of Raman system for supersonic flame measurements.

Mixture Fraction, Temperature, and Concentration Profiles

UV Raman measurements were made in the radial direction at following downstream locations: x/D = 0.85, 10.8, 21.5, 32.3, 43.1, 64.7, and 86.1. For each downstream location, it took about 30 to 40 minutes to finish data acquisition. Data at each measurement location consist of either 500 or 2000 independent laser shots. The mean and rms profiles of mixture fraction, temperature, and multi-species mole fractions are shown in Figs. 41-47. The digital values are tabulated in Appendix B. The data taken at x/D = 0.85 can be used as the initial input for CFD codes and data taken at farther downstream locations can be used for code validation.

For this axisymmetric jet flame, exact axisymmetry is not obtainable due to installation difficulties and the thermal expansion of the main fuel jet in the hot vitiated air. Hence, the center of the jet ($y=0$) is chosen at the maximum mixture fraction and the minimum N_2 mole fraction, as shown by the dashed line in the profiles.

Fig. 41 shows the data taken at x/D = 0.85 ($D=2.36$ mm) where the flowfield is near the nozzle exit. The mean mixture fraction profile (see Fig. 41a) indicates that the mixture fraction is 1 and 0 in the fuel and air stream, respectively. In the mixture fraction calculation (see Eq. 4-7), the mass fraction of hydrogen atoms in the vitiated air is taken into account because of high concentration of water vapor in the vitiated air stream (26 mole %). The mean temperature profile (see Fig. 41c) shows about 1250 K in the vitiated air stream and about 545 K in the fuel stream. The temperature of the supplied fuel is originally 300 K. This increased temperature is
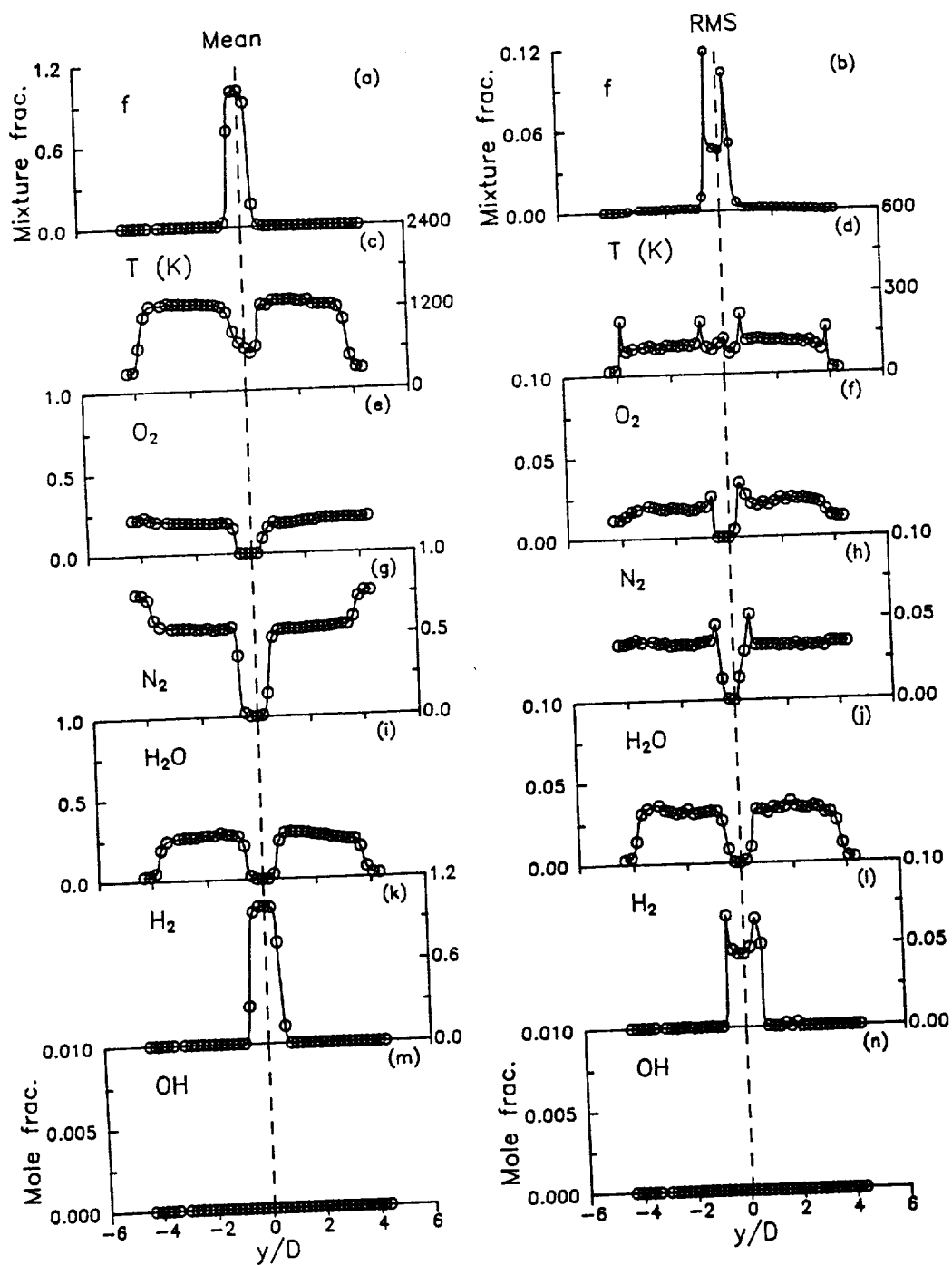
Fig. 41 Mean and rms profiles of mixture fraction, temperature, O_2, N_2, H_2O, H_2, and OH mole fractions at x/D = 0.85.

due to heat transfer from the vitiated air to the fuel tube inside the combustion chamber. For temperatures below 800 K, recall that the ideal gas law equation is used to determine the temperatures by summing all the major species concentrations and assuming atmospheric pressure. The maximum error in the perfect gas temperature measurement is 11% for a fuel exit pressure of 112 kPa. Since there is only mixing but no reaction in the free shear layer at this location, neither increased temperature nor combustion (i.e. products and intermediate radicals) is seen in the profiles (see Figs. 41c, 41i, 41m). Note that mixing takes place in the free shear layer as shown in Fig. 41d. The two inner peaks result from the mixing between the fuel jet and vitiated air stream, and the two outer peaks from the mixing between the vitiated air and ambient air.

To examine the Raman concentration measurements at the nozzle exit (x/D = 0.85), calculations of the mass ratio of O_2 to N_2 at the nozzle inlet and outlet are performed. At the nozzle inlet, the mass flowmeters measured the O_2/N_2 mass ratio as 0.684. At the nozzle outlet, the Raman technique measured O_2/N_2 is 0.682 which agrees very well with the mass flowmeter measurement. The accuracy of the mass flowmeters is about ±3%, and it is about ±2% for the Raman measurement.

Similar profiles are shown in Fig. 42 for x/D = 10.8. The mixture fraction and H_2 mole fraction decrease, and small amounts of O_2, N_2, and H_2O are detected in the fuel stream, due to entrainment of the vitiated air without reaction. The mixing process in the fuel stream is similar to that in the lifted region of the subsonic lifted flame (see Chapter V). Since the fuel jet has an exit Mach number of 1, the
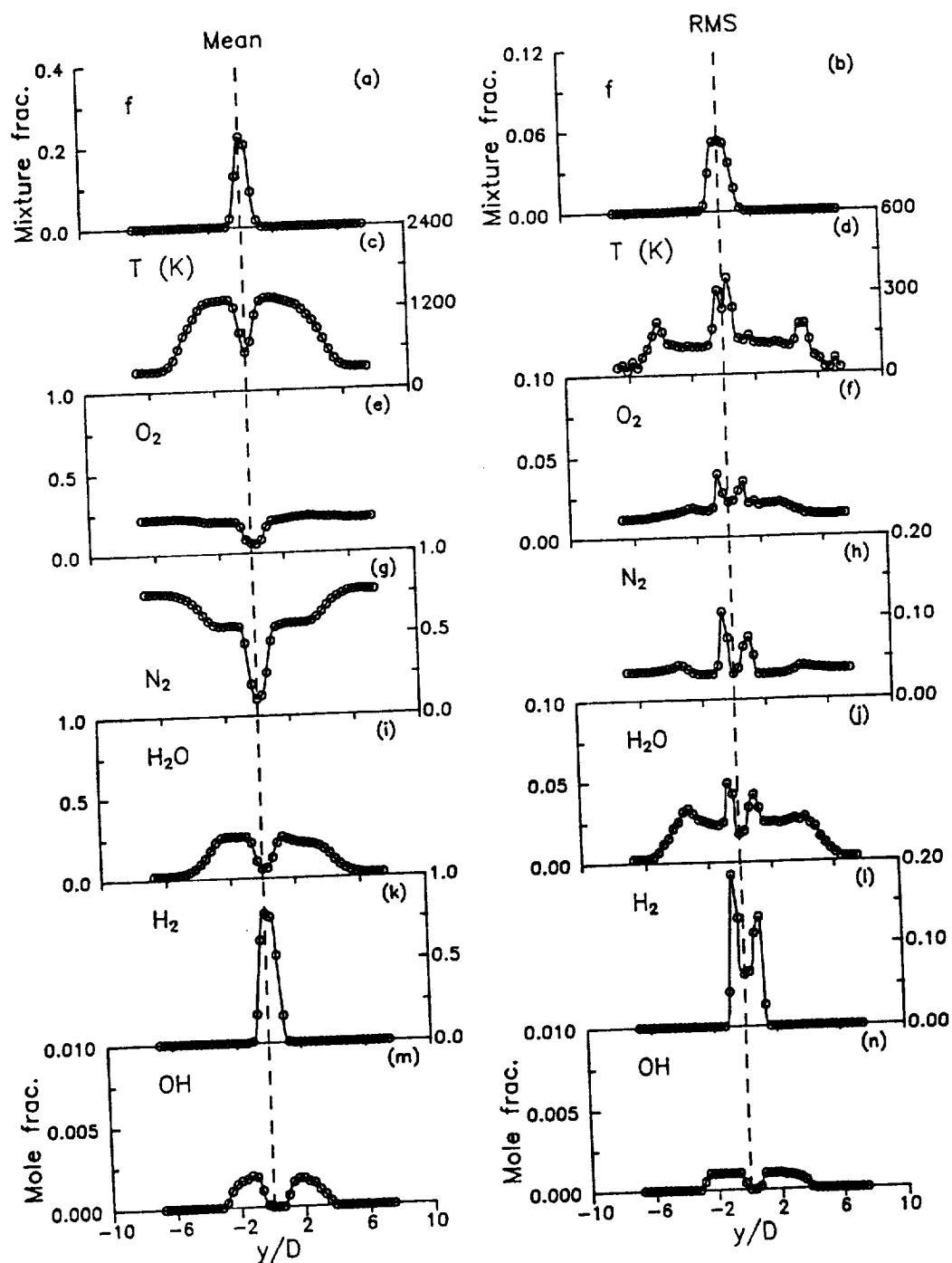
Fig. 42 Mean and rms profiles of mixture fraction, temperature, O_2, N_2, H_2O, H_2, and OH mole fractions at x/D = 10.8.

flame is lifted off about 20 diameters above the nozzle (this liftoff height was obtained from a photograph taken by the NASA group; Jarrett, 1990).

A small amount of OH mole fraction (<0.0025) is found in the vitiated air region (see Fig. 42m). This small amount of OH is either due to two-photon photodissociation of H_2O, to mass diffusion, or to local reaction. If the measured OH were a photofragment, then one should but does not see about the same amount of OH at the location near the nozzle exit (Fig. 41m). If it were due to mass diffusion, then one should but does not see about the same amount of OH in the main fuel jet. In this supersonic flame, ignition could take place because of co-flowing hot vitiated air and shock wave interactions. Therefore, the measured OH is most likely due to ignition rather than photodissociation of water vapor or mass diffusion.

Farther downstream at $x/D = 21.5$ and 32.3, chemical reaction takes place (see Figs. 43 and 44). The mean temperature profiles (see Figs. 43c and 44c) show higher temperatures at positive radii than at negative. These asymmetrical temperature profiles may be due to a wake effect or a shock wave interaction that causes ignition at the positive side. As mentioned earlier the asymmetry of the fuel jet could result in a wake or in an asymmetric shock pattern. This is consistent with the O_2, H_2O, H_2, and OH profiles. At the positive side, more O_2 and H_2 are consumed (see Figs. 43e, 43k, 44e, and 44k), and more H_2O and OH are produced (see Figs. 43i, 43m, 44i, and 44m). The two inner peaks that indicate mixing between the fuel jet and vitiated air are merged into a single peak while the two outer peaks
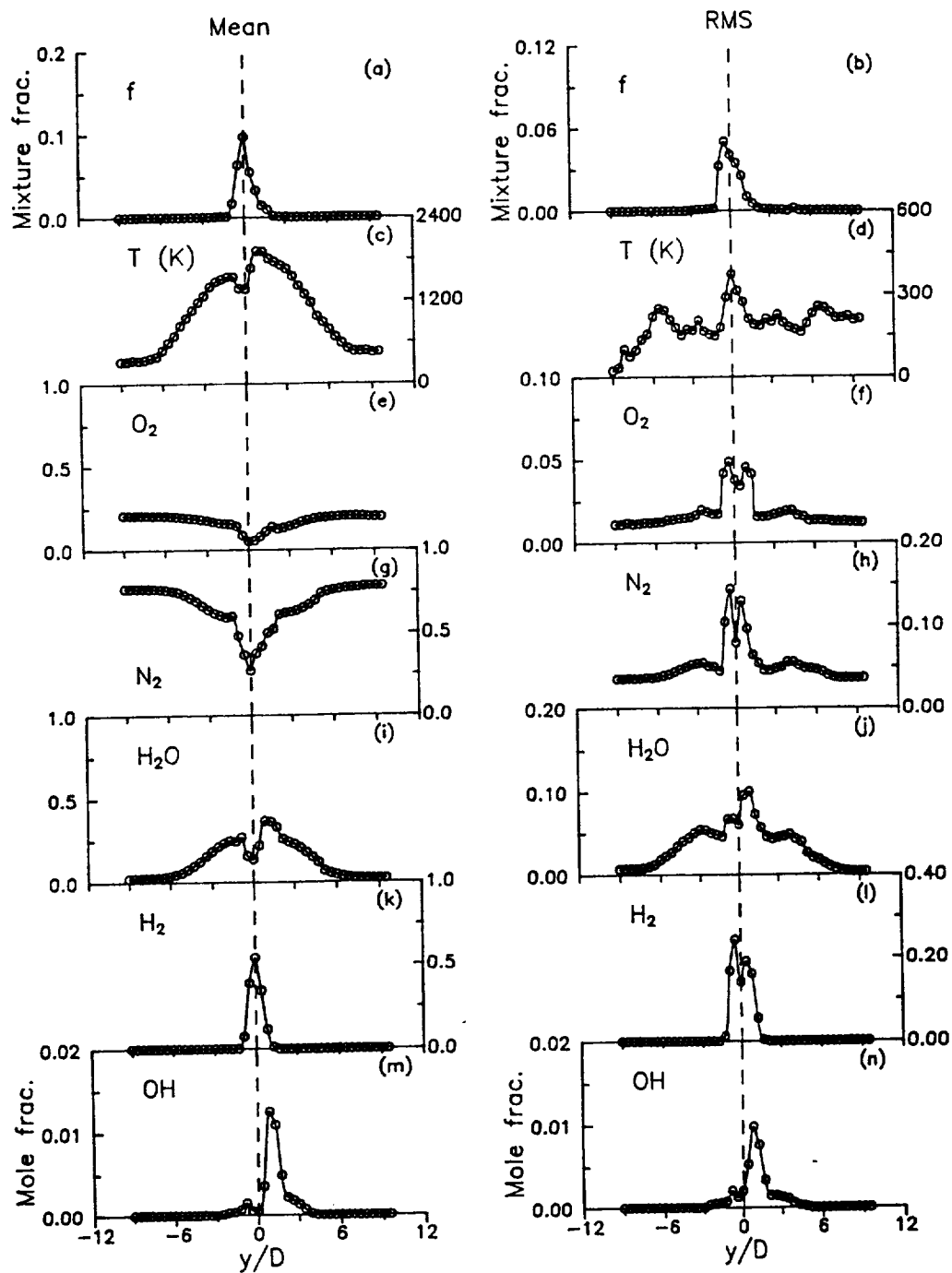
Fig. 43 Mean and rms profiles of mixture fraction, temperature, O_2, N_2, H_2O, H_2, and OH mole fractions at $x/D = 21.5$.
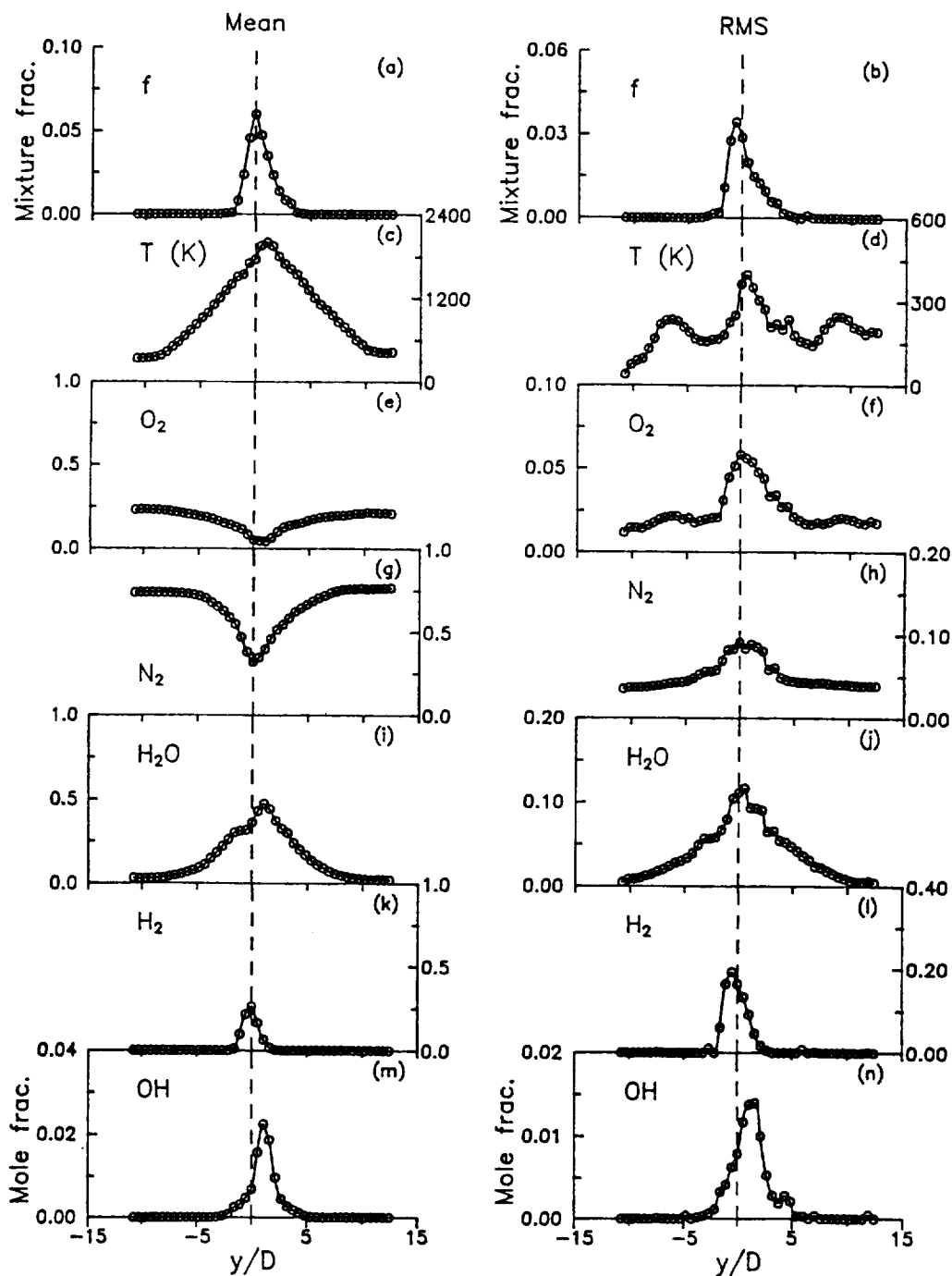
Fig. 44 Mean and rms profiles of mixture fraction, temperature, O_2, N_2, H_2O, H_2, and OH mole fractions at $x/D = 32.3$.

are still evident (see Figs. 43d and 44d). The two outer peaks are not symmetric because most likely the vitiated air stream is tilted slightly in the positive direction with respect to the centerline. At positive radii, the fluctuating rms temperatures near the still air do not decrease as on the negative side. This is due to tilt in the vitiated air stream and travel limitations of the translation stage.

For the axial location at $x/D = 43.1$ (see Fig. 45), the flame temperatures and the OH mole fractions near the centerline are higher than those at the other axial locations. The O_2 mole fraction profile (see Fig. 45e) shows that O_2 molecules are almost consumed near the center of the fuel jet.

Further downstream at $x/D = 64.6$ and 86.1 (see Figs. 46 and 47), the H_2 molecules have been consumed (see Figs. 46k and 47k) and the gas mixtures are in fuel-lean conditions ($f < 0.0283$). Excess O_2 and N_2 molecules from the ambient air have diffused to the center of the jet (see Figs. 46e, 46g, 47e, and 47g). The OH concentrations decrease due to three-body recombination reactions. At $x/D = 86.1$ (see Fig. 47), the flame is nearly in equilibrium. The temperature and concentration profiles are much flatter than those in the upstream locations.

The data presented above are inferred from either 500 or 2000 independent laser shots. Although direct information concerning the interactions of mixing and chemical reaction as well as finite-rate chemistry effects can not be obtained from the mean and rms profiles, they do provide a set of data for validation of CFD models. The measured rms values indicate that the species and temperature fluctuations can be as high as 40% and 20%, respectively. The neglect of these
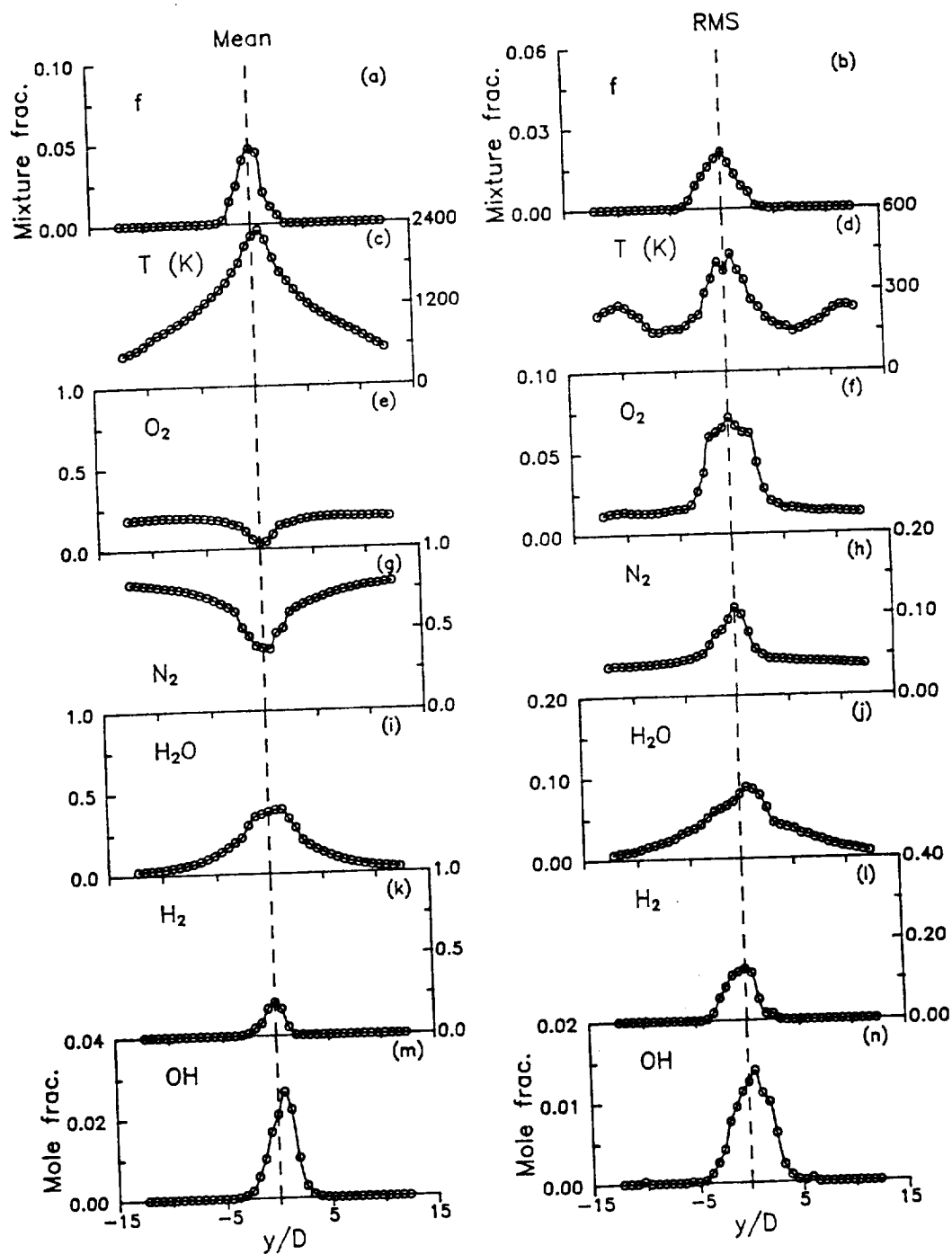
Fig. 45 Mean and rms profiles of mixture fraction, temperature, O_2, N_2, H_2O, H_2, and OH mole fractions at $x/D = 43.1$.
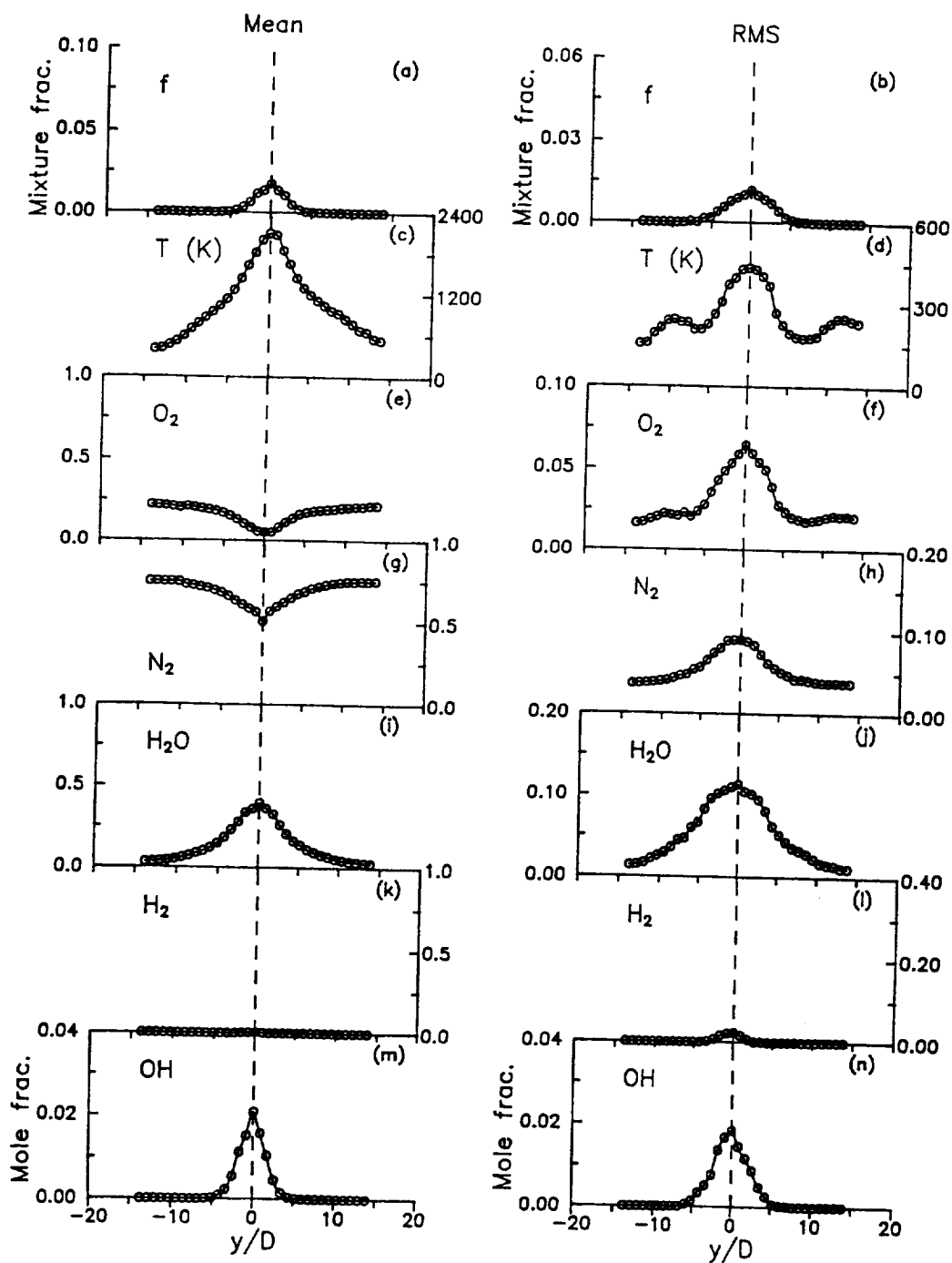
Fig. 46 Mean and rms profiles of mixture fraction, temperature, O_2, N_2, H_2O, H_2, and OH mole fractions at x/D = 64.7.

Mean

RMS

(a)

(b)

f

f

Mixture frac.

Mixture frac.

0.10

0.06

0.05

0.03

0.00

0.00

T (K)

T (K)

(c)

(d)

2400

600

1200

300

0

0

O_2

O_2

(e)

(f)

1.0

0.10

0.5

0.05

0.0

0.00

N_2

N_2

(g)

(h)

1.0

0.20

0.5

0.10

0.0

0.00

H_2O

H_2O

(i)

(j)

1.0

0.20

0.5

0.10

0.0

0.00

H_2

H_2

(k)

(l)

1.0

0.40

0.5

0.20

0.0

0.00

OH

OH

(m)

(n)

Mole frac.

Mole frac.

0.04

0.04

0.02

0.02

0.00

0.00

-20   -10   0   10   20

-20   -10   0   10   20

y/D

y/D
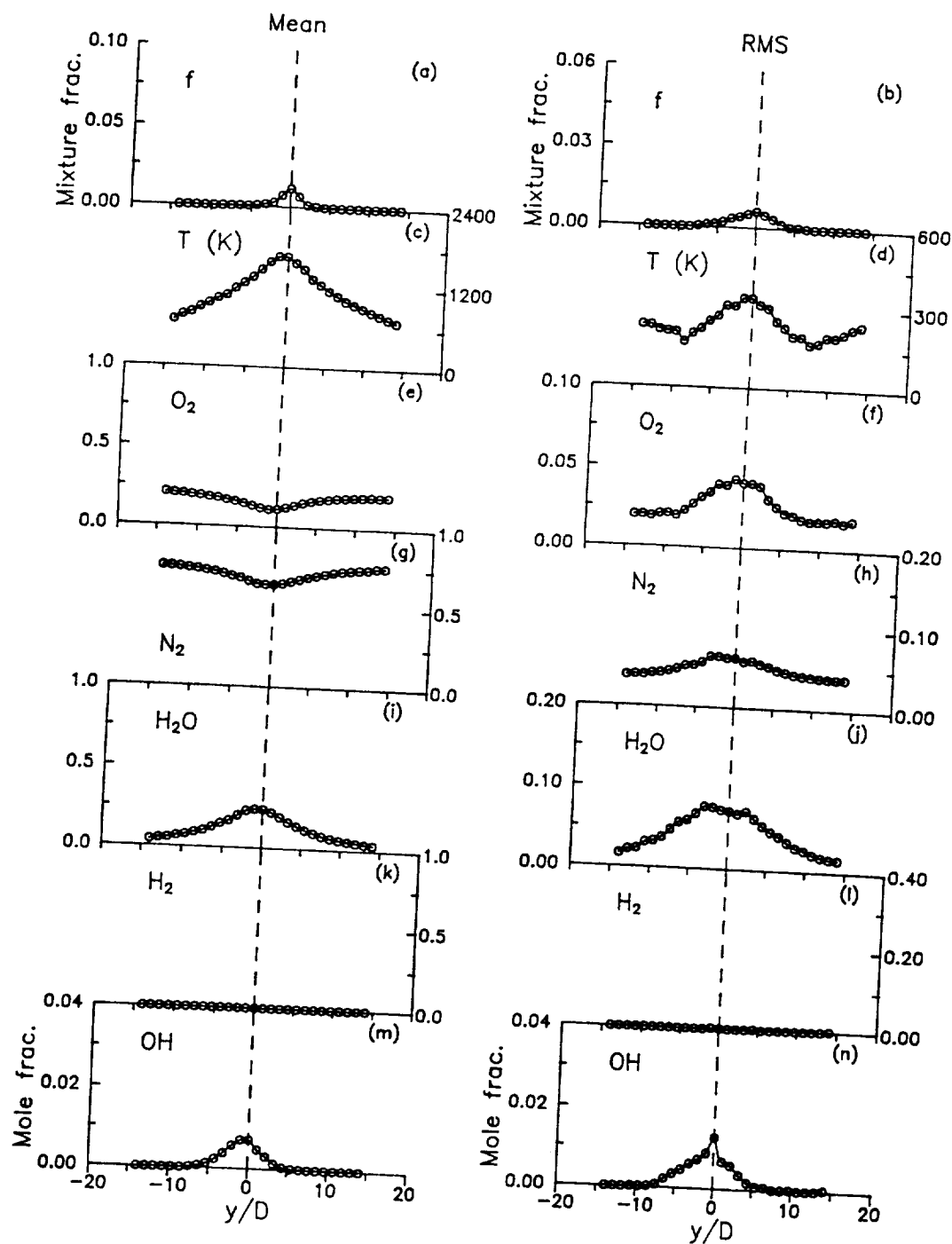
Fig. 47 Mean and rms profiles of mixture fraction, temperature, O_2, N_2, H_2O, H_2, and OH mole fractions at x/D = 86.1.

fluctuation effects on the mean chemical reaction rates in the combustion model can lead to an erroneous flow description including an incorrect prediction of the minor species and the ignition point.

Fluid Mechanical Scales

The Kolmogorov time and length scales are calculated for this supersonic flow. The velocity measurements of Jarrett et al. (1988) are used, and the turbulent fluctuating velocity is assumed to be 10% of the local velocity. The calculated scales and the ratio of the spatial resolution to the integral scale (l/L) for five downstream locations are listed in Table 7. In a supersonic flow these scales are much smaller than those in a subsonic flow (see Table 4). The temporal resolution of the Raman system is well within the requirement for this experiment; however the spatial resolution (~0.4 mm) is beyond the requirement (~3η). Thus, spatial averaging might affect the scalar measurements in this flow. The calculated l/L values indicate that the measurement will capture at least 90% of the mean and rms scalars in this flow, based on the estimation of Mansour et al. (1990).

Identification of Mixing and Finite-Rate Chemistry Effects

To identify the interaction of turbulent mixing and chemical reaction as well as finite-rate chemistry effects in supersonic reacting flow, the single shot measurements of temperature and multi-species concentrations are compared to equilibrium values, as were the data in the previous chapter. Since the exit pressure and temperature in the fuel jet and vitiated air stream are different (see Table 6),

Table 7. Fluid mechanical scales in the supersonic flame.

x/D	r/R_f	U, m/s	T, K	$v \times 10^4$, m^2/s	η, mm	τ_u, μs	L, mm	l/L
0.85	0.00	1780	545	3.29	0.013	0.5	3.4	0.12
	-0.43	1650	861	5.17	0.020	0.7	3.4	0.12
	-0.65	900	1212	3.17	0.021	1.5	3.4	0.12
	-1.72	1082	1273	1.53	0.011	0.8	3.4	0.12
	-2.58	1161	1275	1.53	0.010	0.7	3.4	0.12
	-3.44	1244	1255	1.48	0.009	0.6	3.4	0.12
10.8	0.00	1105	555	2.27	0.015	1.0	4.2	0.10
	-0.32	1120	840	3.51	0.021	1.2	4.2	0.10
	-0.65	1000	1212	2.72	0.019	1.3	4.2	0.10
	-1.29	1154	1331	1.62	0.011	0.8	4.2	0.10
	-2.58	1194	1275	1.52	0.011	0.7	4.2	0.10
	-3.23	1156	1058	1.12	0.009	0.7	4.2	0.10
21.5	0.00	1094	1364	6.56	0.035	1.9	4.9	0.08
	-0.43	1099	1375	5.23	0.029	1.7	4.9	0.08
	-0.86	1135	1543	2.79	0.018	1.2	4.9	0.08
	-1.29	1188	1545	2.04	0.014	0.9	4.9	0.08
	-2.58	1243	1400	1.72	0.012	0.8	4.9	0.08
	-3.44	1089	1176	1.30	0.010	0.8	4.9	0.08
32.3	0.00	1181	1760	6.07	0.034	1.9	7.1	0.06
	-0.54	1184	1703	5.15	0.030	1.8	7.1	0.06
	-1.08	1193	1543	3.14	0.021	1.4	7.1	0.06
	-3.23	1066	1200	1.35	0.012	1.1	7.1	0.06
	-5.38	248	820	0.73	0.023	7.0	7.1	0.06
43.1	0.0	1175	2214	7.45	0.041	2.2	7.4	0.05
	-0.65	1150	2069	5.99	0.035	2.0	7.4	0.05
	-2.58	1000	1534	2.13	0.018	1.5	7.4	0.05
	-3.87	815	1329	1.57	0.017	1.8	7.4	0.05
	-5.81	341	1063	1.09	0.024	5.4	7.4	0.05
	-7.1	167	928	0.88	0.035	14.2	7.4	0.05

l = 0.4 mm (spatial resolution of the Raman system)

the STANJAN program can not be used. The equilibrium temperature and concentration for various mixtures of fuel and air are calculated with the CHEMKIN equilibrium program (Kee et al., 1980).

The turbulent mixing time and Damköhler number for six locations in the flow are calculated. Scatter plots for these six locations will be shown to demonstrate the interactions of turbulent mixing and chemical reaction as well as slow three-body recombination reactions effects. The turbulent mixing times are calculated from Eq. (5-8). The chemical reaction times for two-body and three-body reactions at the locations $x/D \geq 32.3$ are assumed to be the same as that in the atmospheric flames, ~18 μs and ~3 ms for two-body and three-body reactions, respectively. Values of τ_t and both Damköhler numbers are given in Table 8. In the lifted region ($x/D = 0.85$ and 10.8), the chemical reaction times must be much greater than the turbulent mixing times since little reaction is found there. Hence, Damköhler numbers (Da_{2-body} and Da_{3-body}) must be much less than unity. The velocity at $x/D = 86.1$ is obtained by assuming that the decay rate is proportional to x^{-1}. The value of Da_{3-body} is still less than unity which indicates that chemical equilibrium has not reached at this location ($x/D = 86.1$). In scramjet engine designs, the optimal combustor length is required to be long enough for OH radicals to recombine ($Da_{3-body} > 1$) and to release their chemical energy inside the combustor rather than in the exhaust plume.

The scatter plots in this section consist of either 500 or 2000 independent laser shots. The solid curves represent the adiabatic equilibrium condition, and the dashed curves are for mixing without reaction except for the location at $x/D = 86.1$. In the

Table 8. Damköhler numbers for the supersonic flame.

x/D	y/D	ΔU (m/s)	τ_t (ms)	$Da_{2\text{-body}}$	$Da_{3\text{-body}}$
0.85	-0.65	363	0.0005	<< 1	<< 1
10.8	-0.65	295	0.001	<< 1	<< 1
32.3	-1.1	60	0.4	22	0.13
32.3	+1.1	25	1	56	0.33
43.1	0	24	1.1	61	0.37
86.1	0	12	2.1	117	0.7

mixing layer, near the nozzle exit (x/D=0.85, y/D=-0.65), only mixing but no reaction occurs as shown in Figs. 48 and 49. The temperature is about 1150 K which is lower than the vitiated air temperature (1250 K) but higher than the fuel stream temperature (545 K). Since only mixing but no chemical reaction takes place at this point, no intermediate OH radical is produced and the major species mole fractions are on the dashed curves. Here the turbulent mixing time is much less than the two-body reaction time ($Da_{2-body} << 1$). Thus, the flow approaches the limit of a homogenous, reacting mixture.

At the same radial position but 10 diameters farther downstream (x/D=10.8, y/D=-0.65), a little reaction occurs at the fuel-lean side. Figs. 50 and 51 show that most of the fluid is in a rich unignited condition. The small amount of OH is most likely due to local reaction (see Fig. 50b). The lack of pronounced reaction could be due to the high strain rate at this location. The turbulent mixing time is still rapid at this location (~1 μs) however, a wake or the shock wave interactions may cause some ignition to occur.

Farther downstream at x/D = 32.3, the mean temperature profile indicates that the mean temperatures at the positive side are higher than that at the negative side. At this axial location, the scatter plots for two relative radial positions (y/D=-1.1 and 1.1) are shown in Figs. from 52 to 55. The temperature scatter plot (Fig. 52a) shows that reaction occurs at this point, but the flame temperature is far below the equilibrium curve. Although reaction takes place at this position, superequilibrium OH is not observed, and most OH scatter points are below the
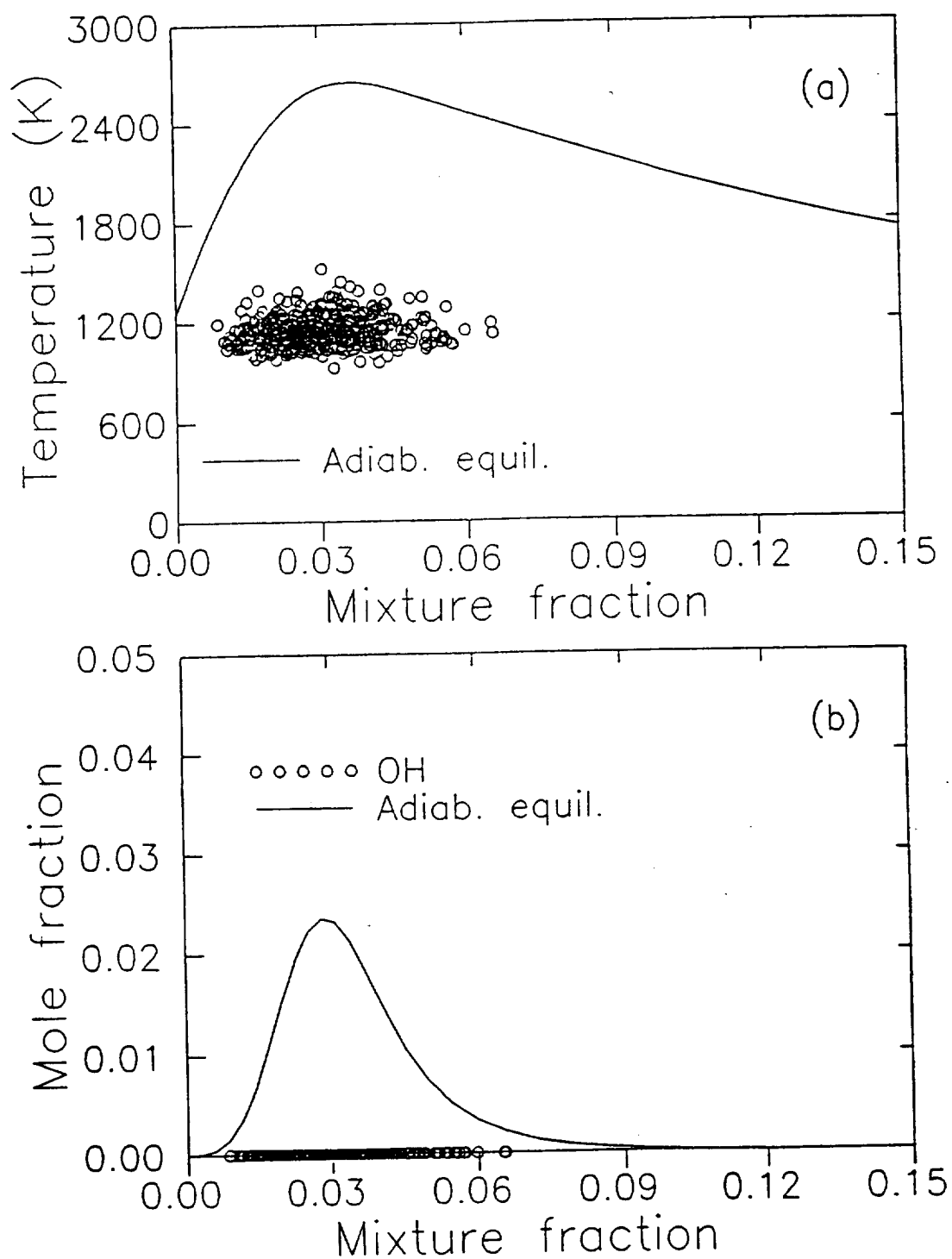
Fig. 48 Scatter plot of temperature and OH mole fraction at x/D = 0.85, y/D = -0.65.
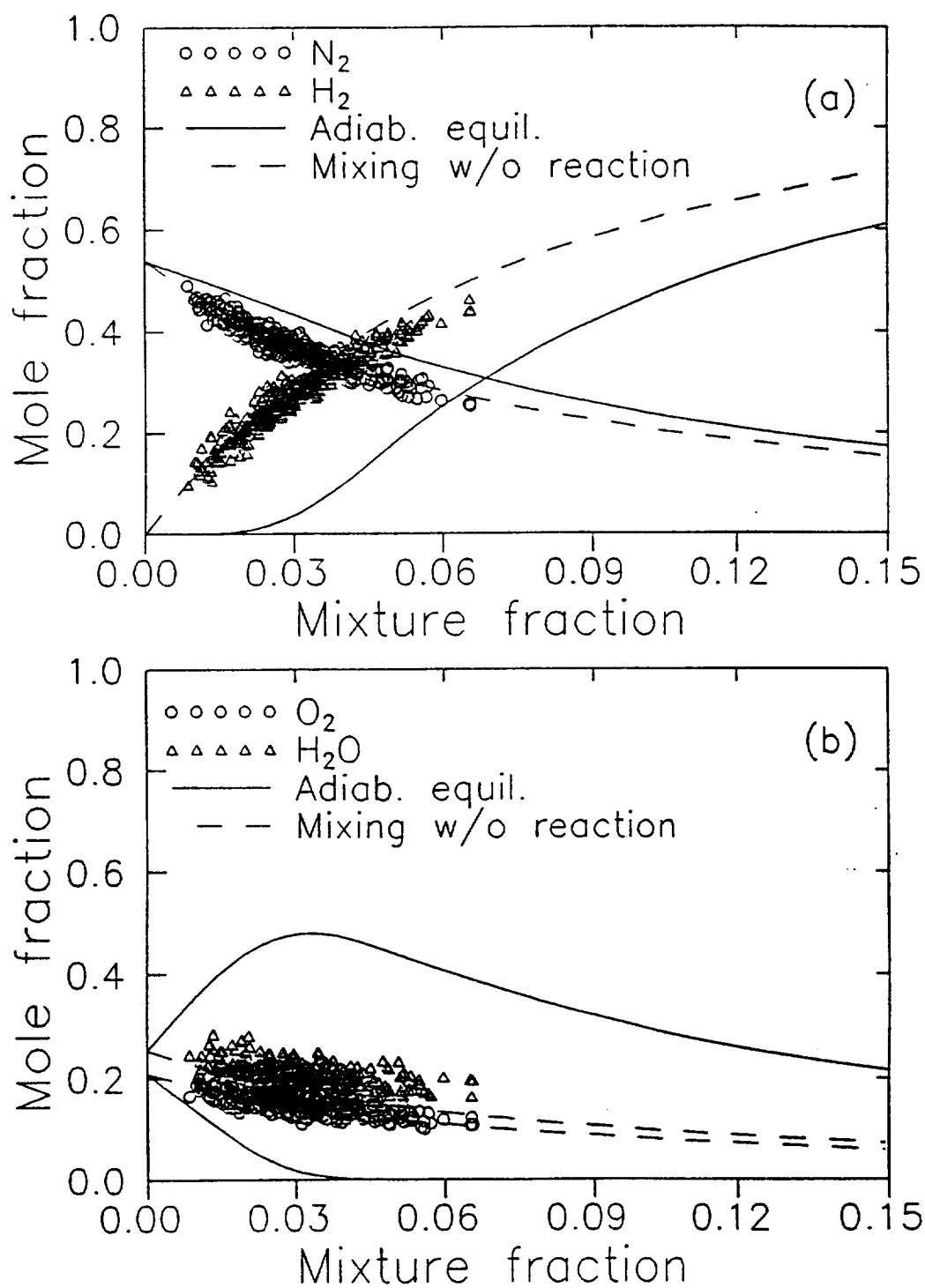
Fig. 49 Scatter plot of major species mole fractions at x/D = 0.85, y/D = -0.65.
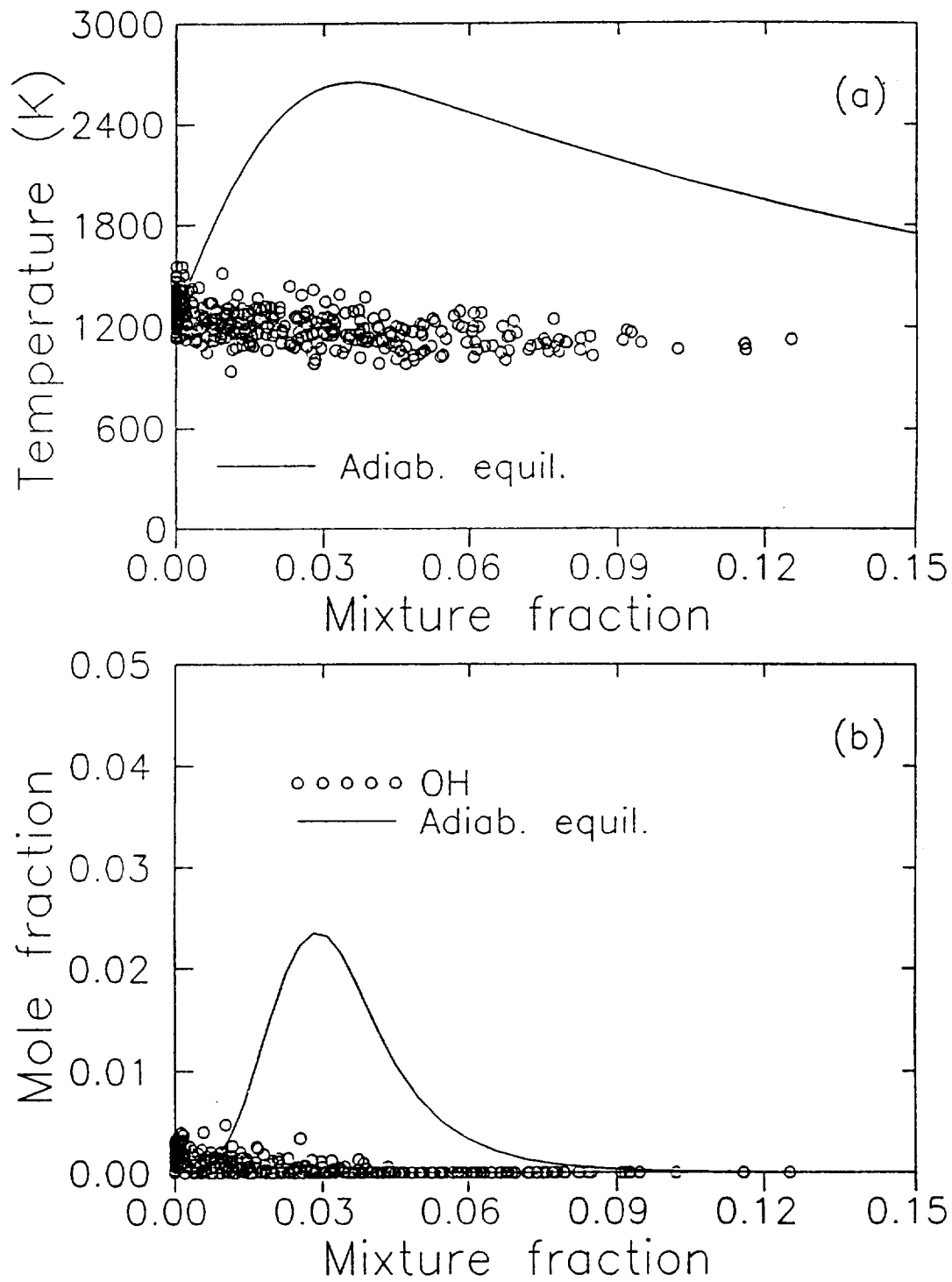
Fig. 50 Scatter plot of temperature and OH mole fraction at x/D = 10.8, y/D = -0.65.
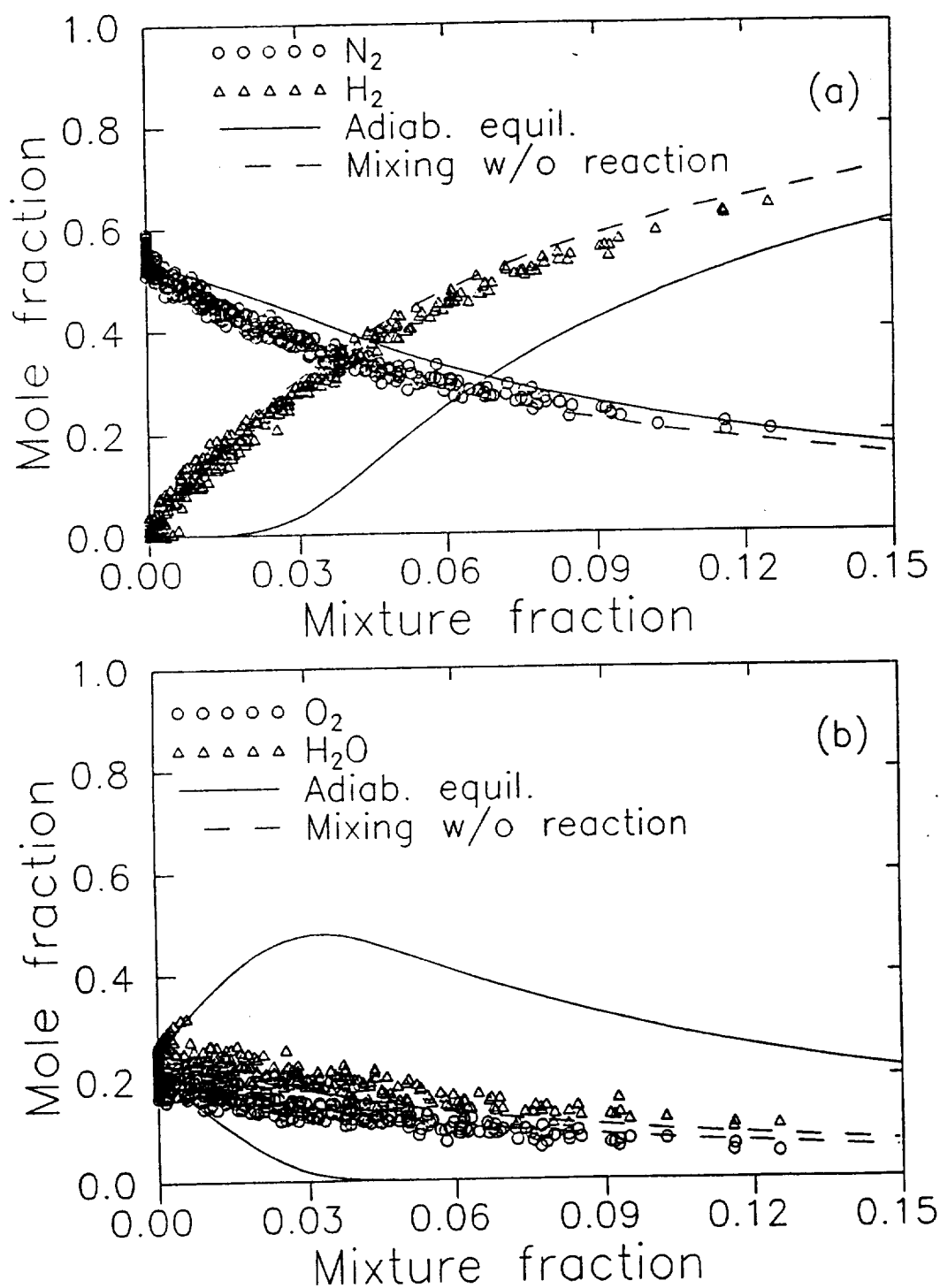
Fig. 51 Scatter plot of major species mole fraction at x/D = 10.8, y/D = -0.65.
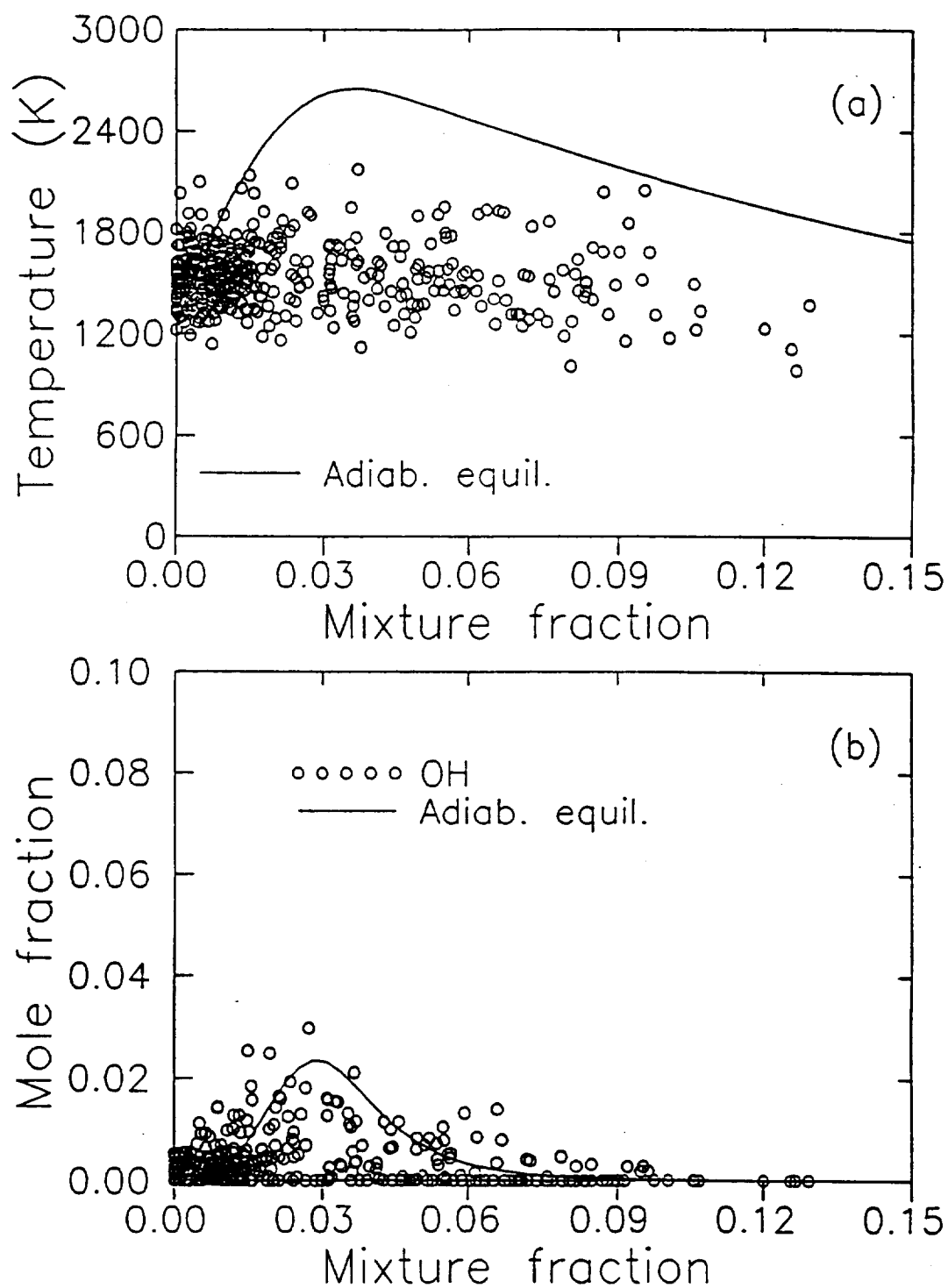
Fig. 52 Scatter plot of temperature and OH mole fraction at x/D = 32.3, y/D = - 1.1.
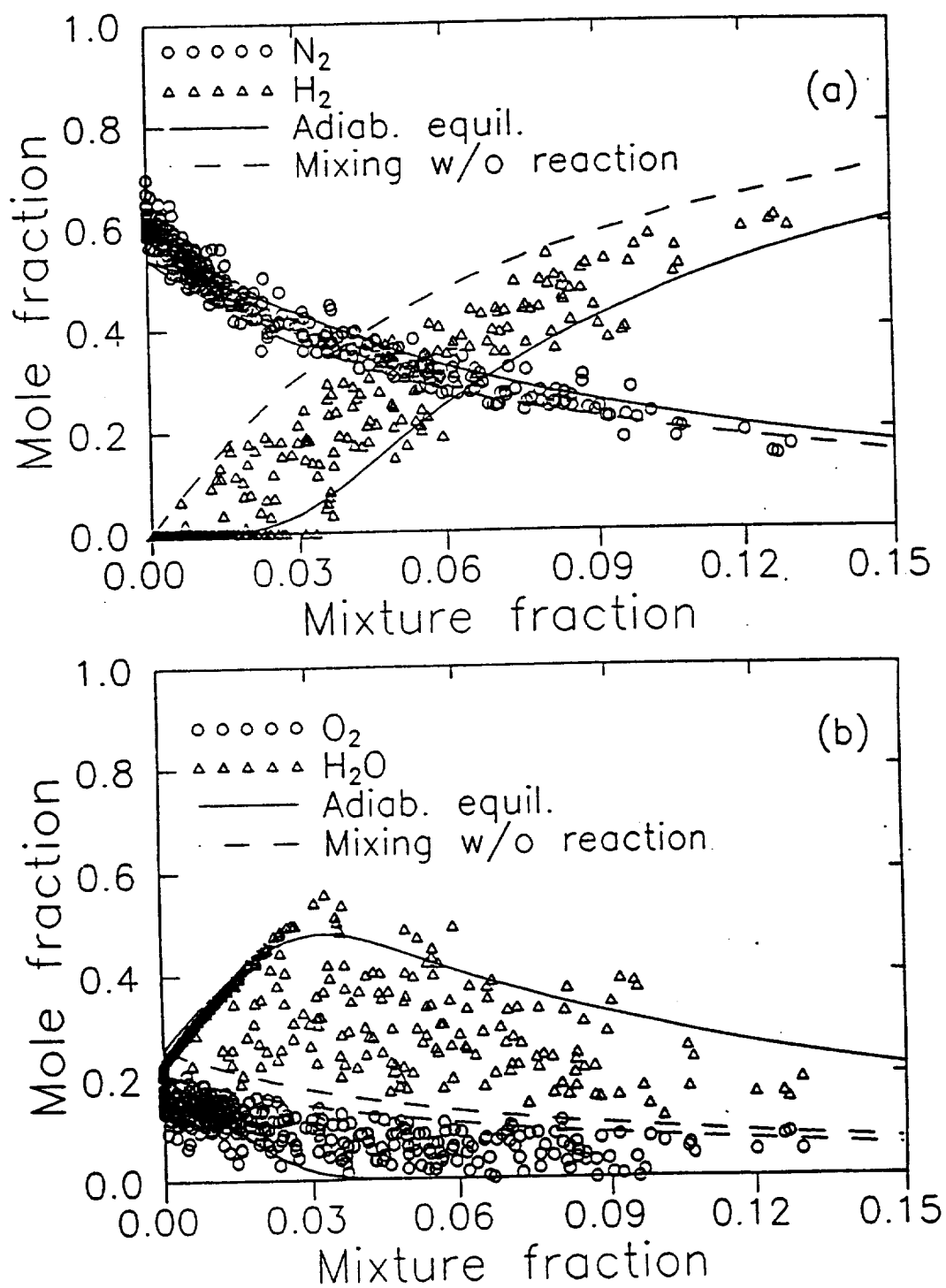
Fig. 53 Scatter plot of major species mole fractions at x/D = 32.3, y/D = -1.1.
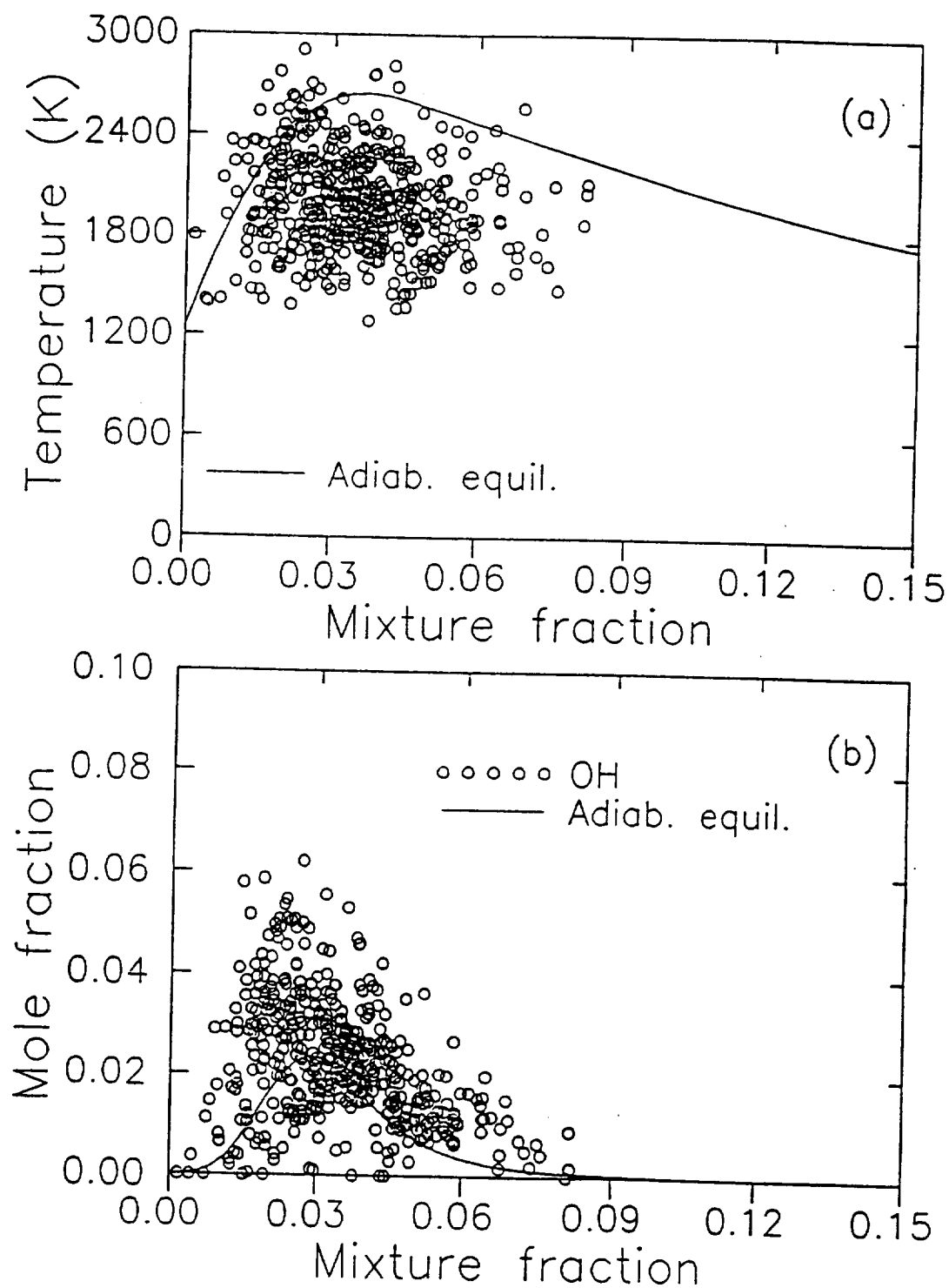
Fig. 54 Scatter plot of temperature and OH mole fraction at x/D = 32.3, y/D = 1.1.
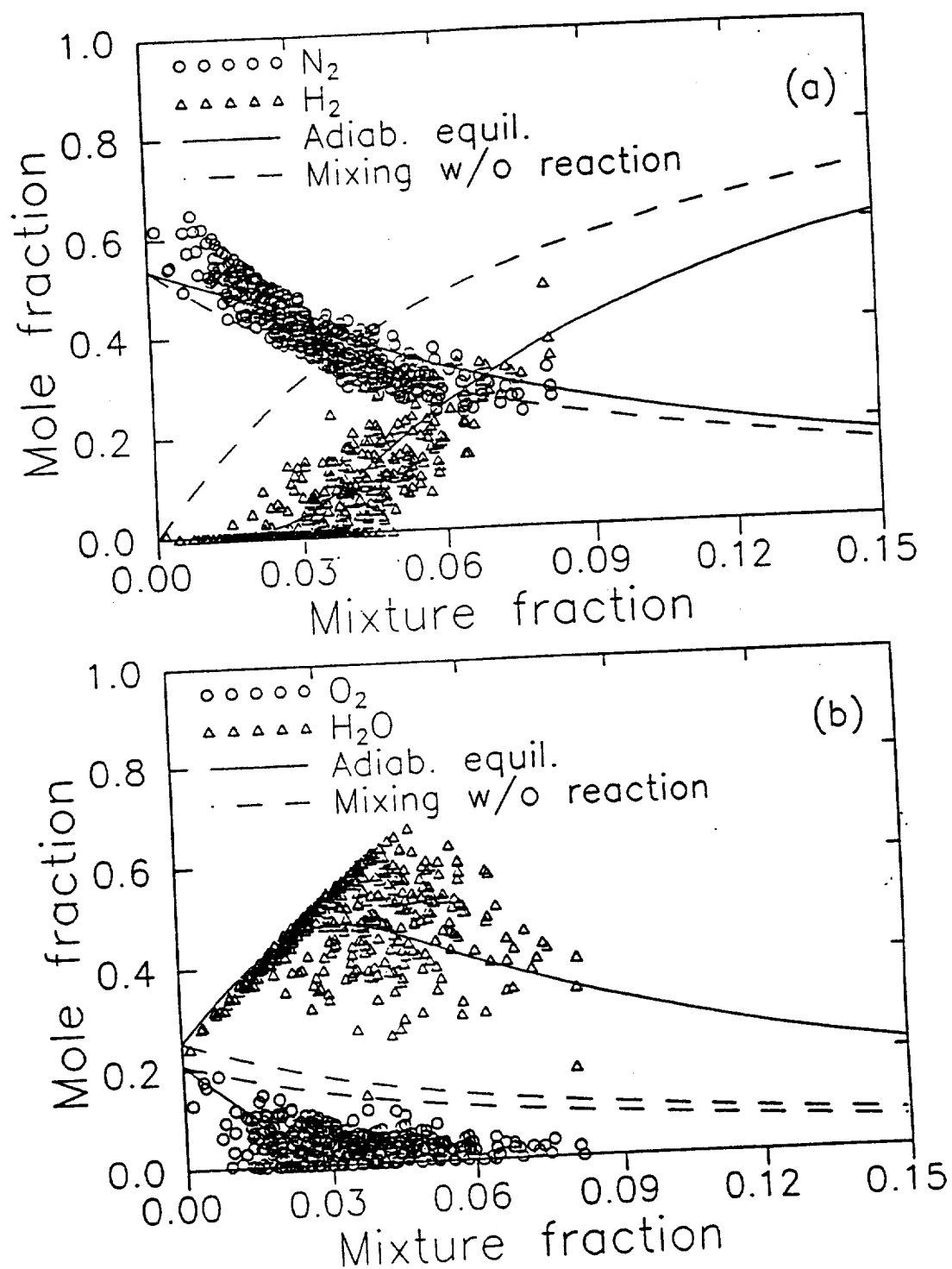
Fig. 55 Scatter plot of major species mole fractions at x/D = 32.3, y/D = 1.1.

equilibrium curve (see Fig. 52b). The scatter points of major species are between the equilibrium curve and the mixing without reaction curve (see Fig. 53). This suggests that flame extinction/ignition processes are occurring at this position. Another possible explanation is that spatial averaging across the steep temperature and species concentrations gradients is occurring because of the thin reaction zones.

At the positive side ($x/D = 32.3$, $y/D = 1.1$), due to more reaction, the flame temperature is higher than that at the negative side. More reaction is possibly due to the formation of a wake or shock wave interactions. The mean temperature is about 2000 K which is about 650 K less than the equilibrium temperature at the mean mixture fraction of 0.035 (see Fig. 54a). This lower mean temperature is possibly either due to flame extinction/ignition phenomena or due to spatial averaging of the thin reaction zones. Some scatter points above the equilibrium curve may be either due to experimental uncertainty or due to differential diffusion. Scatter points near but below the equilibrium curve are caused by the slow three-body recombination of OH radicals which depress the flame temperature below its equilibrium value.

Fig. 54b shows that slow three-body recombination reactions result in superequilibrium OH. The peak OH mole fraction is about 2.5 times the peak equilibrium value. This finding is similar to that in a subsonic lifted flame (see Chapter V). Explanation for sub-equilibrium OH is similar to that for temperature scatter points below the mean value. The major species mole fractions are on the equilibrium curve except N_2 (see Fig. 55). Excess N_2 from the ambient air has

diffused to this point and causes scatter points to deviate from the equilibrium curve. Comparing the major species concentration measurements to the subsonic flame measurements, higher fluctuations in supersonic flame are observed. This is due to higher total enthalpy fluctuations in a supersonic flame.

Farther downstream ($x/D=43.1$, $y/D=0$), similar scatter plots are shown in Figs. 56 and 57. At this location, the mean flame temperature is still up to ~400 K less than the adiabatic equilibrium temperature due to finite-rate chemistry effects. Explanations for departure of the scatter points from the equilibrium curve are similar to that for the location at $x/D = 32.3$, $y/D = 1.1$. Note that there is a small amount of unburnt H_2 in the flow (see Fig. 57a); therefore less H_2O is produced (see Fig. 57b).

Near the equilibrium zone ($x/D=86.1$), similar scatter plots are shown in Figs. 58 and 59. Since this is an open flame, ambient air can be entrained into the flame and affect the flame temperature and gas composition. The effects are more evident further downstream as the velocity decays. Fig. 58a shows that the mean scatter points are between the solid curve and the dashed curve. In Figs. 58 and 59, the solid curve is the usual adiabatic equilibrium condition which is calculated based on the nozzle exit conditions. The dashed curve is the adiabatic equilibrium condition for hydrogen burning with ambient air (296 K, 1 atm). Fig. 58b shows that the mean OH scatter points are on the solid curve. Although they are on one of the equilibrium curves, the actual equilibrium condition can not be determined because of the unknown amount of ambient air entrainment. However, if one imagines a
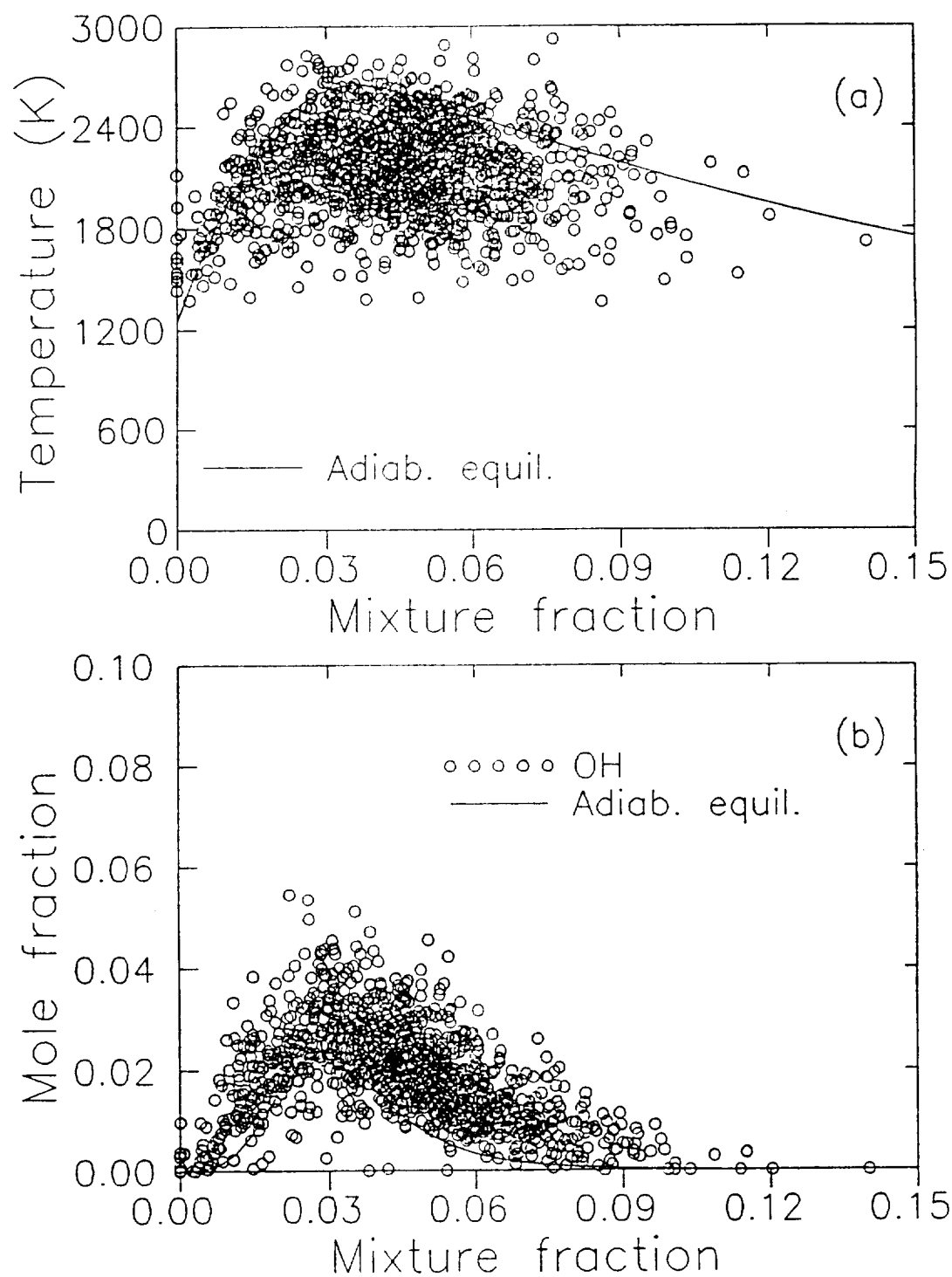
Fig. 56 Scatter plot of temperature and OH mole fraction at x/D = 43.1, y/D = 0.
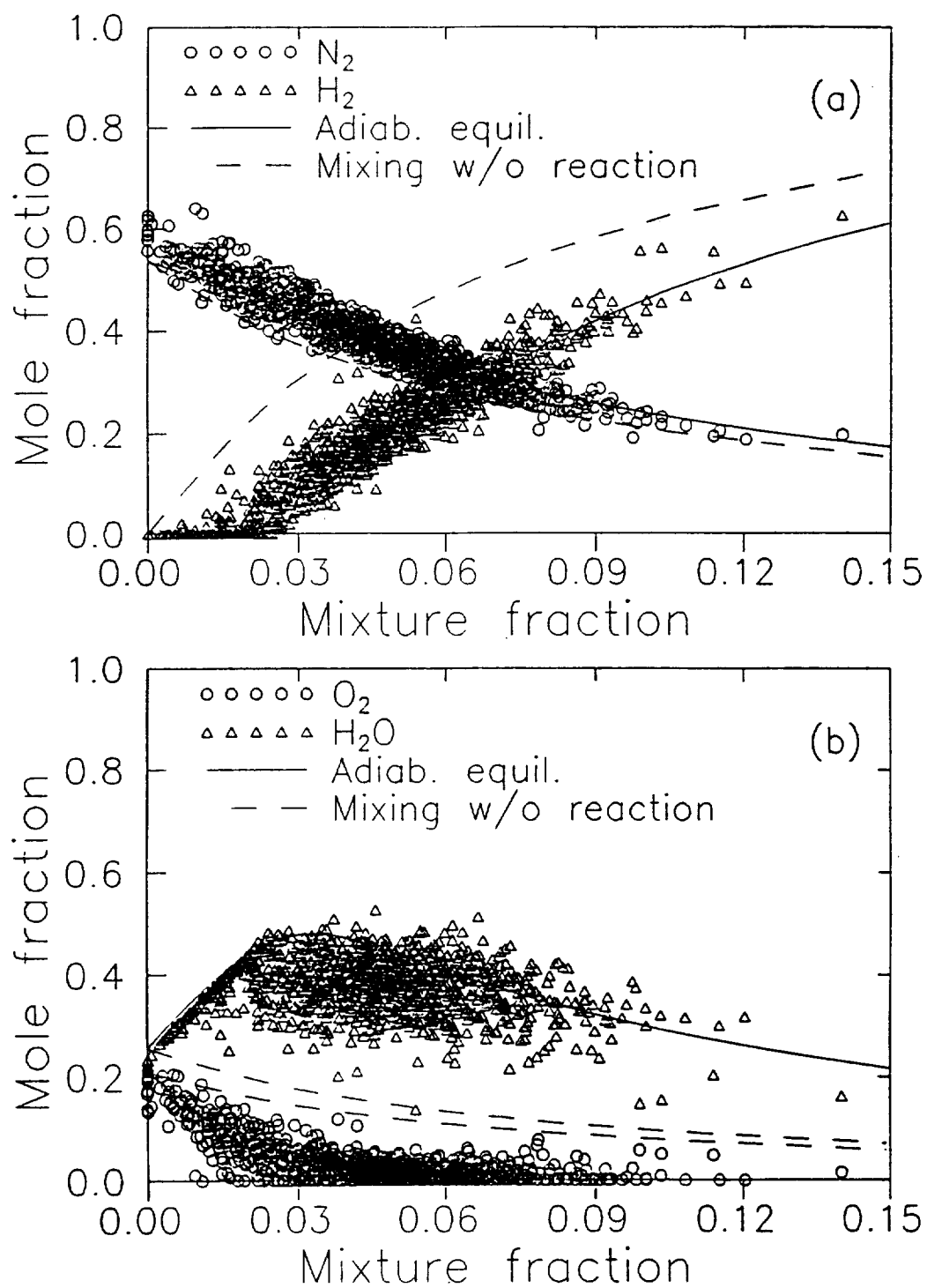
Fig. 57 Scatter plot of major species mole fractions at x/D = 43.1, y/D = 0.
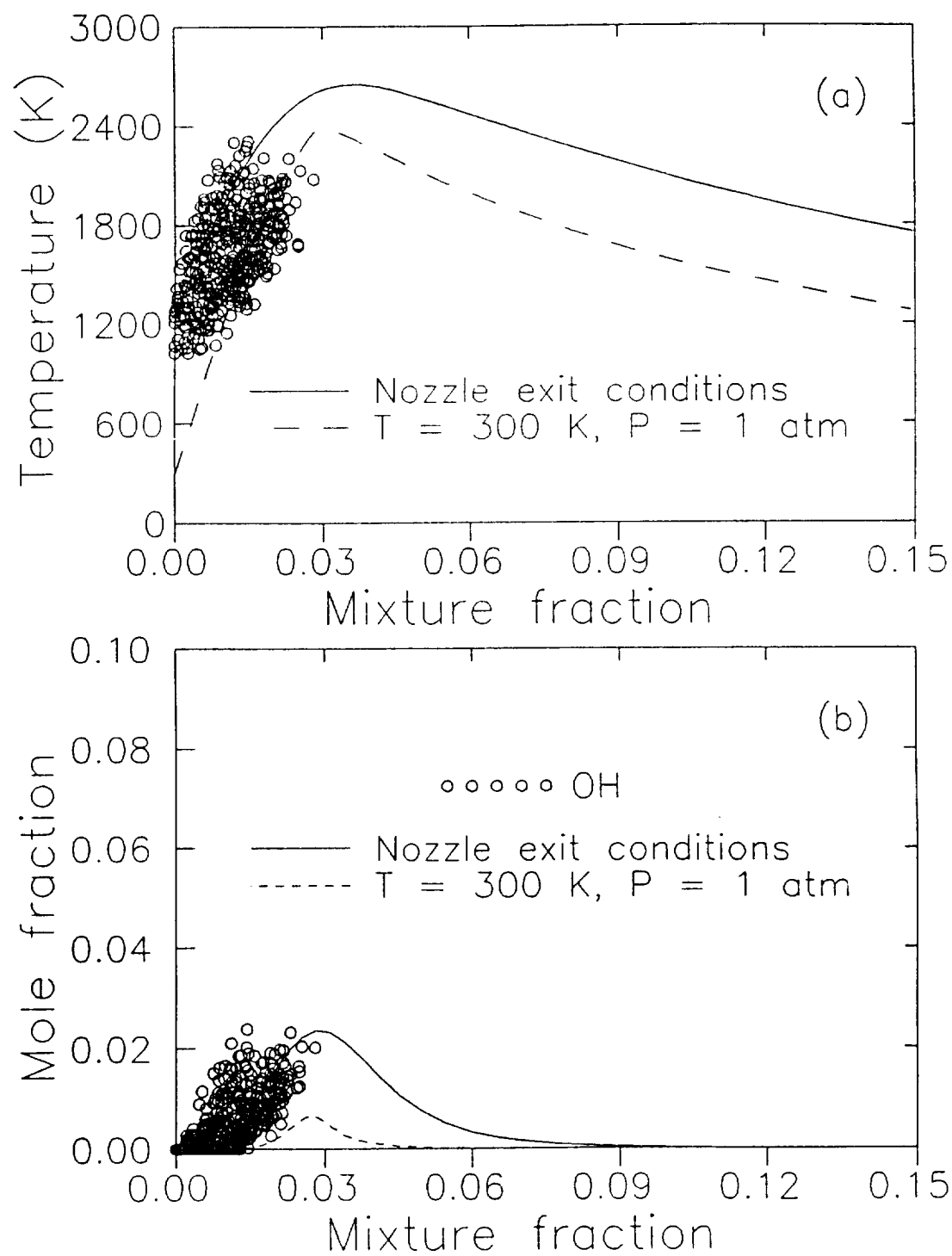
Fig. 58 Scatter plot of temperature and OH mole fraction at x/D = 86.1, y/D = 0.
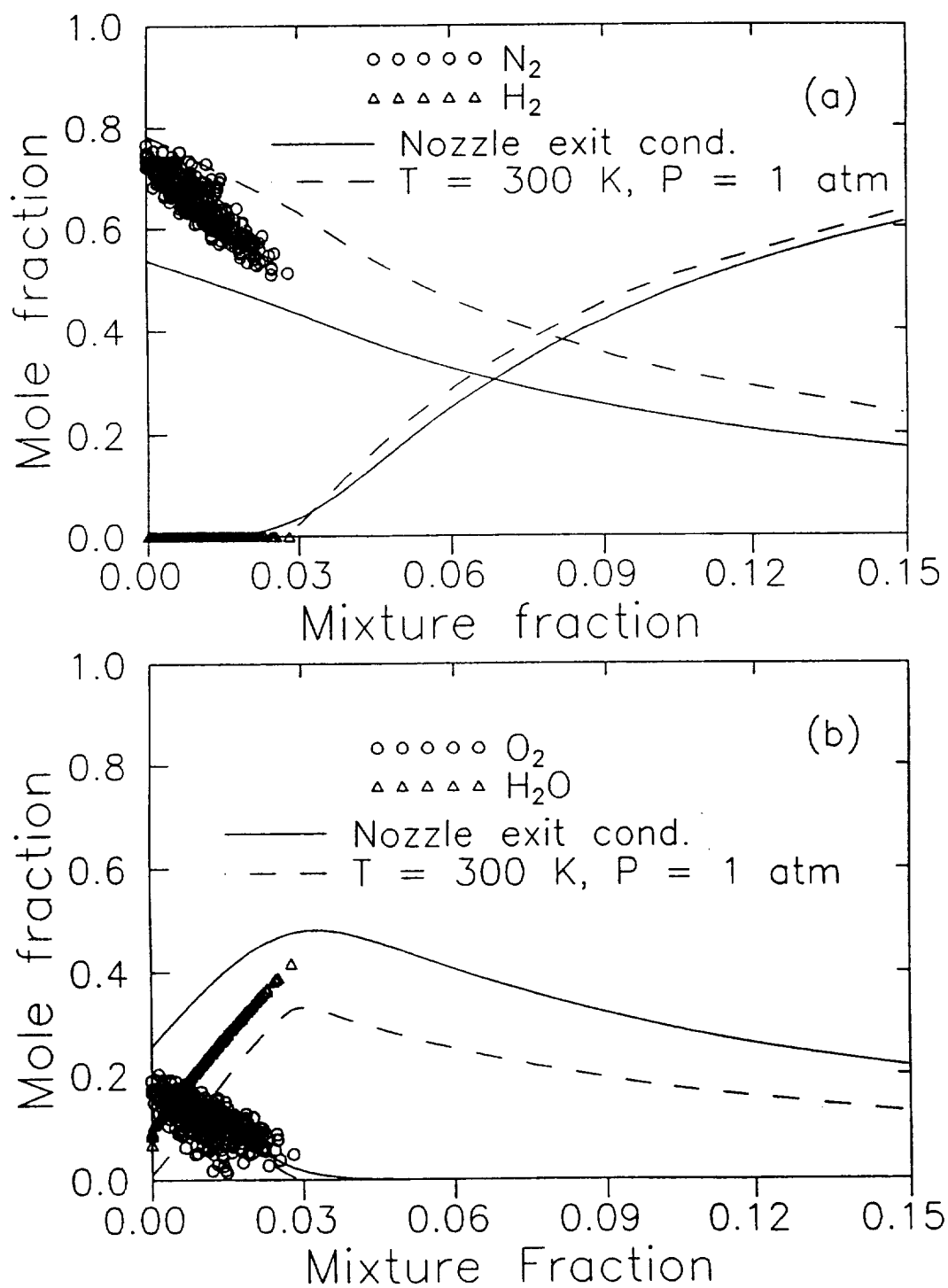
Fig. 59 Scatter plot of major species mole fractions at x/D = 86.1, y/D = 0.

curve passing through the mean temperature data (between the solid and dashed curves), then a corresponding equilibrium curve for OH will fall between the lines drawn in Fig. 58b. The OH data are then above this last equilibrium curve, which means that the equilibrium condition has not been achieved at this location. The calculated Damköhler number ($Da_{3-body} = 0.7$) is still less than unity and less than that in the equilibrium region of the subsonic flame ($Da_{3-body} = 2.3$). This also indicates that equilibrium condition is not achieved.

Fig. 59a shows that H_2 has burnt out and ambient air entrainment has increased the N_2 concentration. Fig. 59b indicates that O_2 is on the equilibrium curve because there are the same amounts of O_2 in the vitiated air stream and in the ambient air. The H_2O has the same trend as temperature and falls between the two equilibrium curves.

Vibrational Relaxation Time of N_2

For temperatures higher than 800 K, the present temperature measurements were made using the ratio of the N_2 Stokes to anti-Stokes signal. For this approach, a vibrational equilibrium Boltzmann distribution is assumed. In subsonic flames, the gas flow residence time is normally longer than the time required for nitrogen molecules to reach vibrational equilibrium. However, the gas flow residence time is short in supersonic flows. For example, the flow time at the first measurement location ($x/D = 0.85$) is ~1.4 μs in the vitiated air stream. The vibrational relaxation time of N_2 must be shorter than the gas flow residence time so that the N_2 molecules

are in equilibrium conditions and the vibrational temperature measurements are valid.

Vibrational relaxation of N_2 has been studied in shock tubes by a number of researchers (Blackman, 1956; Center and Newton, 1978; Kozlov et al., 1987; Kurian and Sreekanth, 1987). Blackman (1956) for example made shock-tube studies of vibrational relaxation in pure O_2 (800-3200 K) and pure N_2 (800-6000 K) using an optical interferometer. Kurian and Sreekanth (1987), using a laser schlieren technique, studied the vibrational relaxation of N_2 by H_2O in the temperature range 1300-3100 K behind incident shock waves. For N_2-N_2 molecular collisions (at T = 1250 K and P = 1 atm), each molecule requires ~700 μs and ~3.3 x 10^6 molecular collisions to reduce the "out-of-equilibrium" vibrational energy to $1/e$ of its initial value. This vibrational relaxation time of N_2 by N_2 (~700 μs) is much longer than the gas flow residence time at the first measurement location in this supersonic flow. This means that if this were a pure N_2 supersonic flow, the vibrational temperature measurements would not be valid.

Fortunately, the air is vitiated. The combustion product, H_2O, is an efficient catalyst in speeding up vibrational relaxation of N_2. Kurian and Sreekanth (1987) found the N_2-H_2O relaxation times to be best described by:

$$P\ \tau\ =\ \exp\ (11.3267\ T^{-1/3}\ -\ 1.7325) \tag{6-1}$$

where P is the pressure in atm, τ is the vibrational time in s, and T is the temperature in K. For the temperature of 1250 K and the assumed pressure of 1

atm, the vibrational relaxation time of N_2-H_2O is ~0.5 μs which is about 2.8 times shorter than the gas flow residence time (~1.4 μs). Therefore, the N_2 vibrational temperature measurements in this supersonic flow are valid even at the first measurement station in the air flow. The ideal gas law temperature must be computed in the fuel jet at this location.

CHAPTER VII

CONCLUSIONS AND FUTURE EFFORTS

Summary and Conclusions

A UV Raman scattering system which combines spontaneous Raman scattering with laser-induced predissociative fluorescence (LIPF) has been developed for flame diagnostics. This Raman system, using a narrowband KrF excimer laser, has several advantages over other Raman systems and laser-based techniques such as CARS. The inherent repetition rate and temporal resolution of the KrF laser are better than that of a flashlamp-pumped dye laser. Also, the spatial resolution is improved due to increased signal strength from the increased Raman cross section in the ultraviolet. The improved spatial resolution is about 2.5 and 10 times better than the dye laser system and the CARS system, respectively. For species concentration measurements, the UV Raman system with a single excimer laser can provide more major species measurements than the CARS system.

In addition to the above-mentioned advantages, about 5% broadband emission from the narrowband KrF excimer laser induces predissociative fluorescence (LIPF) of OH. This predissociative fluorescence allows quantitative minor species measurement of OH because the LIPF signal is not sensitive to collisional quenching.

To determine the optimal laser wavelength for reducing fluorescence

interferences, OH and O_2 fluorescence excitation spectra are obtained. The superposition of these fluorescence excitation spectra shows that the best combination of fluorescence reduction and separation of residual fluorescence from Raman signals is for a laser tuning to 248.623 nm. Various flame spectra indicate that some residual fluorescence from O_2 and OH interfere with the O_2 and H_2O Raman signals, respectively. This residual fluorescence is subtracted out from the O_2 and H_2O Raman signals by monitoring the O_2 fluorescence signal at 337.5 nm and the OH fluorescence signal at 297.5 nm. Although the OH fluorescence at 271.7 nm (near the H_2O Raman signal) is greatly reduced, the fluorescence signal at 297.5 nm is strong enough for quantitative OH concentration measurement.

The UV Raman system is calibrated with a flat-flame Hencken burner operated at several known equivalence ratios. The measured flame temperatures and measured flowrates are used to calculate equilibrium species concentrations. The measured temperatures, measured Raman signals, and calculated equilibrium species concentrations are used to obtain the calibration constants and bandwidth factors for vibrational temperature and species concentration measurements in turbulent reacting flows.

For Raman scattering measurement, the major contributor to the single-shot signal uncertainty is photon shot noise. The relative standard deviations of the single-shot measurements correspond well with estimated values based on the predicted shot noise. The calibration results are compared with adiabatic equilibrium values. The agreement of the calibration data with theoretical equilibrium data is

satisfactory.

Simultaneous measurements of temperature, major species (H_2, O_2, N_2, H_2O), and minor species (OH) are then made in a subsonic lifted turbulent hydrogen diffusion flame. Local mixture fraction is calculated from the Raman scattering measurement of major species concentrations for each laser shot. Mean and rms values are obtained from an ensemble of 1000 laser shots. Instantaneously measured temperature and species concentrations (expressed in terms of mole fractions) are compared with "infinite-rate" equilibrium conditions for locations in the lifted zone, slow three-body recombination zone, and equilibrium zone.

In the lifted zone ($x/D = 7$, $D = 2$ mm), mixing but no chemical reaction is observed in the center of the jet ($r/R_f = 0$). The temperature is essentially room temperature and the major species concentrations of O_2, N_2, and H_2 are in a premixed, rich, unignited condition. The nonreactive O_2 concentration has a N_2/O_2 ratio about the same as room air (3.76). No combustion product (H_2O) or intermediate OH radical is produced. The premixing of fuel and air found at this location is due to air entrainment upstream of the flame base. Since the turbulent mixing time (~ 15.6 μs) is much less than the two-body reaction time ($Da_{2\text{-body}} < < 1$), no combustion occurs even though the fuel and air are premixed to a flammable condition. The quantitative findings demonstrate that turbulent mixing affects chemical reaction and results in departure from the classical "fast chemistry" assumption.

In the lifted zone at the radial position $r/R_f = 2.17$, the turbulent mixing time

(~0.24 ms) is longer than the two-body reaction time (~18 μs) but is shorter than the three-body recombination time (~3 ms). Combustion takes place in an intermittent annular turbulent flame brush with strong finite-rate chemistry effects. Major species and temperature are found with nonequilibrium values. The OH radical exists both in subequilibrium and superequilibrium concentrations due to intermittency. The peak OH mole fraction is about 2 times the peak equilibrium value. The superequilibrium OH radical concentrations are due to slow three-body recombination reactions, as noted above.

In the slow three-body recombination zone (x/D = 50), major species concentrations are in partial equilibrium. Temperature and minor species concentrations have nonequilibrium values. A typical superequilibrium OH of 2-2.5 times the stoichiometric value is observed. The slow three-body recombination reactions lead to temperature depressions of about 150 K from the equilibrium temperature. In the equilibrium zone (x/D = 175), temperature, minor species, and major species are in equilibrium.

To study the complex turbulence-chemistry interactions in a supersonic reacting flow, UV Raman measurements are made in a Mach 2 jet flame located at NASA Langley Research Center. In this supersonic flow, the flame is lifted about 20 diameters above the nozzle. At x/D = 0.86, y/D = -0.65, mixing but no chemical reaction is found as the turbulent mixing rate is rapid compared to the two-body chemical reaction rate. Hence, neither combustion product (H_2O) nor intermediate radical (OH) is produced.

At $x/D = 10.8$, $y/D = -0.65$, a little reaction occurs. The reaction may be due to shock wave interactions or mixing of hot vitiated air that causes ignition to take place in the mixing layer. Significant reaction takes place farther downstream ($x/D > 20$), because both the residence time and the turbulent mixing time increase with streamwise distance. At $x/D = 86.1$, the major species concentrations are in a partial equilibrium condition but the minor species concentrations are in a nonequilibrium condition. The nonequilibrium OH radicals will decay toward equilibrium values farther downstream.

Comparing the subsonic with the supersonic lifted flame measurements, some differences are found. No chemical reaction is observed upstream of the subsonic lifted flame. Upstream of the supersonic lifted flame, due to shock interactions and mixing with pre-heated air, chemical reaction occurs at $x/D > 0.85$. Highly turbulent fluctuations in the supersonic flame, that lead to high fluctuations in the total enthalpy and the species concentrations, are observed. In the subsonic flame, which has no shocks, the Damköhler number formed using the large-eddy time scale and the two-body reaction time scale (Da_{2-body}) should be at least 10 for chemical reaction to occur. In the supersonic flame, which has shock interactions and mixing with hot vitiated air, some reaction occurs in the lifted region. To reach partial equilibrium, Da_{2-body} should be greater than 50 for both flames. For obtaining the equilibrium condition, the Damköhler number based on the large-eddy time scale and the three-body recombination reaction time scale (Da_{3-body}) should be greater than unity for both flames.

A complete measurement of temperature and multi-species concentrations can both allow a study of turbulence-chemistry interactions and provide information for the input and validation of combustion models. This successful application of the UV Raman scattering system to laboratory flames can be extended to the testing and performance evaluation of actual scramjet engines in engine testing facilities.

Future Work

In some combustion models, the fuel/air mixing process is modeled using assumed shaped PDFs of mixture fraction (f) and a reaction progress variable (q) to account for turbulence-chemistry interactions. A major assumption made in the model is that f and q are statistically independent. If this were so, the covariance of f and q and the correlation coefficient between f and q will be zero. This assumption needs to be validated experimentally. Since the Raman system provides simultaneous measurements of temperature, major species, and minor species concentrations, the mixture fraction (f) can be simultaneously determined from the major species measurements for each laser shot. Through reactions R1-R7 (see Chapter V), the mass fractions of O and H, and hence the reaction progress variable can be calculated by assuming that two-body reactions are in partial equilibrium. Therefore, the major assumption made in the model can be validated.

The measurement of hydrogen atoms (H) is generally made by a two-photon-excited fluorescence technique. If simultaneous measurements of temperature, major species, OH and H are possible, the OH measurement, using LIPF technique, can

be validated through the conservation of hydrogen atoms.

Several modifications to the Raman system will improve the signal strength and hence spatial resolution. By applying an anti-reflecting coating to the polarization rotator, the polarized light and hence the Raman signal can be increased. The MgF_2 laser windows are birefringent which reduces the laser's polarization. Replacement of the MgF_2 windows with CaF_2 windows could increase the vertically polarized light, resulting in better signal strength. The factory made primary Cassegrain mirrors which have ~50% reflectivity need to be re-coated to improve the reflectivity and the Raman signal strength. In addition, one may use a spherical mirror to reflect the laser beam back after it passed through the flame. This could improve the signal strength and hence spatial resolution.

The plano-convex focusing lens produces a non-uniform cross section, resulting in a non-uniform power distribution in the sample volume. This may cause photodissocation of water vapor and production of OH photofragements. To improve the uniformity of the focused laser beam, the plano-convex focusing lens will be replaced with two cylindrical focusing lenses that have different focusing lengths. These cylindrical lenses should produce a more uniform laser beam that will prevent photodissociation of water vapor.

Linewise Raman measurements rather than pointwise measurements can be made by using a two-dimensional CCD camera to measure the Stokes signals and a one-dimensional photodiode array for the anti-Stokes signal. This could provide information on the scalar dissipation rate in the turbulent flames. In addition, with

a two-dimensional CCD camera, information on the burning behavior of various flame structures can be obtained by the laser-induced predissociative fluorescence technique.

APPENDIX A

DATA REDUCTION PROGRAM

```c
#include"math.h"
#include"stdio.h"
#define NUMBER 500
FILE *in, *out;
main()
{
double T, ratio;
int counter = 1,i;
float data1,data2,data3,data4,data5,data6,data7,data8;
float O2_BCF, N2_BCF, H2O_BCF, H2_BCF, k7, k5;
float O2sig, N2sig, H2Osig, H2sig, OHsig, O2Fsig;
float H2_rot, O2F_O2, O2conc, N2conc, H2Oconc, H2conc, OHconc,
      O2Fconc, Mix_frac,H2_Boltz,QH2,Mix_O;
float Total_conc, O2molfrac, N2molfrac, H2Omolfrac,
      H2molfrac, OHmolfrac, Perf_Gas_T,x;
float totT=0.0,totMix_frac=0.0,totO2=0.0,totN2=0.0,totH2O=0.0,
      totH2=0.0,totOH=0.0,SQMix=0.0,SQT=0.0,avgT,avgMix,
      avgO2mol,avgN2mol,avgH2Omol,avgH2mol,avgOHmol,SumSQMix,
      SumSQT,SQavgT,SQavgMix,flucMix,flucT,rmsMix,rmsT;
float totO2con=0.0,totN2con=0.0,totH2Ocon=0.0,totH2con=0.0,
      totOHcon=0.0,avgO2conc,avgN2conc,avgH2Oconc,avgH2conc,
      avgOHconc;
float QO2conc=0.0,SQN2conc=0.0,SQH2Oconc=0.0,SQH2conc=0.0,
      SQOHconc=0.0,SQO2mol=0.0,SQN2mol=0.0,SQH2Omol=0.0,
      SQH2mol=0.0,SQOHmol=0.0,SumSQO2conc,SQavgO2conc,
      flucO2conc,rmsO2conc,SumSQN2conc,SQavgN2conc,flucN2conc,
      rmsN2conc,SumSQH2Oconc,SQavgH2Oconc,flucH2Oconc,
      rmsH2Oconc,SumSQH2conc,SQavgH2conc,flucH2conc,
      rmsH2conc,SumSQOHconc,SQavgOHconc,flucOHconc,rmsOHconc;
float SumSQO2mol,SQavgO2mol,flucO2mol,rmsO2mol,SumSQN2mol,
      SQavgN2mol,flucN2mol,rmsN2mol,SumSQH2Omol,SQavgH2Omol,
      flucH2Omol,rmsH2Omol,SumSQH2mol,SQavgH2mol,flucH2mol,
      rmsH2mol,SumSQOHmol,SQavgOHmol,flucOHmol,rmsOHmol;

float totPerf_Gas_T=0.0,SQPerfT=0.0,avgPT,SumSQPT,
      SQavgPT,flucPT,rmsPT;
char filename[15],ch;
float k1=1.0341363;
float k2=3.0462789;
float k3=0.7879641;
float k4=1.;
float k8=0.25;
float k9=0.01;
```

```
float k10=0.1874;


printf("What is the position?\n");
scanf("%f",&x);

printf("Enter the input filename\n");
scanf("%s",filename);
while ((in = fopen(filename,"r"))==NULL)
{
fclose(in);
printf("\n%s does not exist. Please reenter.",filename);
scanf("%s",filename);
}
printf("What is the single-shot output filename?");
scanf("%s",filename);
while((out = fopen(filename,"r"))!=NULL)
{
fclose(out);
printf("\n%s already exists. Please reenter.",filename);
scanf("%s",filename);
}
out = fopen(filename,"w");

while ((ch=fgetc(in))!='|');
fprintf(out,"|\n");
while(counter <= NUMBER)
 {
fscanf(in,"%f %f %f %f %f %f %f %f",&data1,&data2,&data3,&data4,
&data5,&data6,&data7,&data8);

  if(data8 <= 0.)data8=0.0025;
if ( data3/data8 <18.0994 && data8 >= 15.0 && data3 >25.0)
{
 ratio =(data3)/(data8);

 T = 3357.6/(log(ratio) + 1.3011217);

 k7=0.449592*exp(0.000631478*T);
 k11=0.00128888*exp(0.00281508*T);

 O2_BCF = 1.04585-0.00013618*T-1.26574e-7*T*T;
 N2_BCF = 1.0187-7.22248e-5*T-2.94867e-8*T*T;
```

```
H2O_BCF = 1.0034-1.13377e-5*T-1.79358e-8*T*T;
H2_BCF = 6.25742-0.00167201*T+1.61726e-7*T*T;


O2sig = (data2)/data1;
N2sig = (data3)/data1;
H2Osig =(data4)/data1;
H2sig = (data5)/data1;
OHsig = (data6*1.17)/data1;
O2Fsig =( data7)/data1;


H2sig = H2sig-O2Fsig*k10;
if(H2sig < = 0.0) H2sig=0.0;
QH2 = T/(2.0*87.5654);
H2_rot = H2sig*((33*exp(-2489.7/T)+13*exp(-3451.55/T))/QH2)*k7;


O2conc = (O2sig - O2Fsig*k8 - H2_rot)*k1*O2_BCF;
if(O2conc < 0.0)O2conc = 0.0;


N2conc = N2sig*k2*N2_BCF;
if(N2conc < 0.0)N2conc=0.0;


if(H2sig > = O2Fsig)
H2Oconc = (H2Osig - OHsig*k9 + H2sig*k11)*k3*H2O_BCF;
else
H2Oconc = (H2Osig - OHsig*k9)*k3*H2O_BCF;
if(H2Oconc < 0.0) H2Oconc =0.0;


H2conc = H2sig*k4*H2_BCF;
if(H2conc < 0.0) H2conc =0.0;


Total_conc = O2conc + N2conc + H2Oconc + H2conc;
Perf_Gas_T = 7.3402636e3/Total_conc;


O2molfrac = O2conc/Total_conc;
N2molfrac = N2conc/Total_conc;
H2Omolfrac = H2Oconc/Total_conc;
H2molfrac = H2conc/Total_conc;
Mix_frac = (H2conc*2.0 + H2Oconc*2.0)/(O2conc*32.0 +
N2conc*28.0 + H2Oconc*18.0 + H2conc*2.0);


Mix_O=1.0-((32.0*O2conc+16.0*H2Oconc)/(2.0*H2conc+32.0*O2conc+
28.0*N2conc+18.0*H2Oconc))/0.23309;
```

```
if(Mix_frac < 0.0283)
OHsig=OHsig-1.272*O2Fsig;
else if (Mix_frac < 0.0283 && Mix_frac > 0.0149)
OHsig=OHsig-1.48824*O2Fsig;
else
OHsig=OHsig;

if(OHsig > = 1.3248)
k5=1.05205*OHsig-1.47777;
else
k5=0.0089;
OHconc  =  k5*1.0e-2;
if(OHconc < = 0. || OHconc < 3.1782e-4)OHconc=0.0;
OHmolfrac = OHconc/Total_conc;

totT + = T;
totMix_frac + = Mix_frac;
totO2 + = O2molfrac;
totN2 + = N2molfrac;
totH2O + = H2Omolfrac;
totH2 + = H2molfrac;
totOH + = OHmolfrac;
totPerf_Gas_T + = Perf_Gas_T;

SQMix + = pow(Mix_frac,2.0);
SQT + = pow(T,2.0);
SQO2mol + = pow(O2molfrac,2.0);
SQN2mol + = pow(N2molfrac,2.0);
SQH2Omol + = pow(H2Omolfrac,2.0);
SQH2mol + = pow(H2molfrac,2.0);
SQOHmol + = pow(OHmolfrac,2.0);
SQPerfT + = pow(Perf_Gas_T,2.0);

fprintf(out,"%.5f %.5f %6.1f %.3f %.3f %.3f %.3f %.5f %6.1f\n",
        Mix_frac,Mix_O,T,O2molfrac,N2molfrac,H2Omolfrac,H2molfrac,
        OHmolfrac,Perf_Gas_T);
printf("counter= %d  T= %f\n",counter,T);
counter++;
}
else
{
 T=273.;
 Perf_Gas_T=300;
```

```
i=0;
while(abs(T-Perf_Gas_T)>20.)
{
T=Perf_Gas_T;

k7=0.449592*exp(0.000631478*T);
k11=0.00128888*exp(0.00281508*T);

O2_BCF  =  1.04585-0.00013618*T-1.26574e-7*T*T;
N2_BCF  =  1.0187-7.22248e-5*T-2.94867e-8*T*T;
H2O_BCF  =  1.0034-1.13377e-5*T-1.79358e-8*T*T;
H2_BCF  =  6.25742-0.00167201*T+1.61726e-7*T*T;

O2sig  =  (data2)/data1;
N2sig  =  (data3)/data1;
H2Osig  =(data4)/data1;
H2sig  =  (data5)/data1;
OHsig  =  (data6*1.17)/data1;
O2Fsig  =( data7)/data1;

H2sig  =  H2sig-O2Fsig*k10;
if(H2sig <= 0.0) H2sig=0.0;
QH2 = T/(2.0*87.5654);
H2_rot = H2sig*((33*exp(-2489.7/T)+13*exp(-3451.55/T))/QH2)*k7;

O2conc  =  (O2sig - O2Fsig*k8 - H2_rot)*k1*O2_BCF;
if(O2conc < 0.0)O2conc = 0.0;

N2conc  =  N2sig*k2*N2_BCF;
if(N2conc < 0.0)N2conc=0.0;

if(H2sig >= O2Fsig)
H2Oconc  =  (H2Osig - OHsig*k9 + H2sig*k11)*k3*H2O_BCF;
else
H2Oconc  = (H2Osig - OHsig*k9)*k3*H2O_BCF;
if(H2Oconc < 0.0) H2Oconc =0.0;

H2conc  =  H2sig*k4*H2_BCF;
if(H2conc < 0.0) H2conc =0.0;

Total_conc = O2conc + N2conc + H2Oconc + H2conc;
Perf_Gas_T = 7.3402636e3/Total_conc;
```

```
i=i+1;
if(i>500)break;
}
O2molfrac = O2conc/Total_conc;
N2molfrac = N2conc/Total_conc;
H2Omolfrac = H2Oconc/Total_conc;
H2molfrac = H2conc/Total_conc;

Mix_frac = (H2conc*2.0 + H2Oconc*2.0)/(O2conc*32.0 +
        N2conc*28.0 + H2Oconc*18.0 + H2conc*2.0);

Mix_O=1.0-((32.0*O2conc+16.0*H2Oconc)/(2.0*H2conc+32.0*O2conc+
        28.0*N2conc+18.0*H2Oconc))/0.23309;

if(Mix_frac <0.0283)
OHsig=OHsig-1.48824*O2Fsig;
else
OHsig=OHsig;

if(OHsig >= 1.3248)
k5=1.05205*OHsig-1.47777;
else
k5=0.0089;
OHconc = k5*1.0e-2;
if(OHconc <= 0. || OHconc < 3.1782e-4)OHconc=0.0;
OHmolfrac = OHconc/Total_conc;

totT += T;
totMix_frac += Mix_frac;
totO2 += O2molfrac;
totN2 += N2molfrac;
totH2O += H2Omolfrac;
totH2 += H2molfrac;
totOH += OHmolfrac;
totPerf_Gas_T += Perf_Gas_T;

SQMix += pow(Mix_frac,2.0);
SQT += pow(T,2.0);
SQO2mol += pow(O2molfrac,2.0);
SQN2mol += pow(N2molfrac,2.0);
SQH2Omol += pow(H2Omolfrac,2.0);
SQH2mol += pow(H2molfrac,2.0);
SQOHmol += pow(OHmolfrac,2.0);
```

```
SQPerfT + = pow(Perf_Gas_T,2.0);

fprintf(out,"%.5f %.5f %6.1f %.3f %.3f %.3f %.3f %.5f %6.1f\n",
    Mix_frac,Mix_O,T,O2molfrac,N2molfrac,H2Omolfrac,H2molfrac,
    OHmolfrac,Perf_Gas_T);

printf("counter= %d  Perf_Gas_T= %f\n",counter,Perf_Gas_T);
counter++;
}
}

avgT = totT/counter;
avgMix = totMix_frac/counter;
avgO2mol =totO2/counter;
avgN2mol = totN2/counter;
avgH2Omol = totH2O/counter;
avgH2mol = totH2/counter;
avgOHmol = totOH/counter;
avgPT = totPerf_Gas_T/counter;

SumSQMix = SQMix/counter;
SQavgMix =pow(avgMix,2.0);
flucMix = SumSQMix - SQavgMix;
rmsMix= pow(flucMix,0.5);

SumSQT = SQT/counter;
SQavgT = pow(avgT,2.0);
flucT = SumSQT - SQavgT;
rmsT =pow(flucT,0.5);

SumSQPT = SQPerfT/counter;
SQavgPT = pow(avgPT,2.0);
flucPT = SumSQPT - SQavgPT;
rmsPT = pow(flucPT,0.5);

SumSQO2mol = SQO2mol/counter;
SQavgO2mol = pow(avgO2mol,2.0);
flucO2mol = SumSQO2mol - SQavgO2mol;
rmsO2mol =pow(flucO2mol,0.5);

SumSQN2mol = SQN2mol/counter;
SQavgN2mol = pow(avgN2mol,2.0);
flucN2mol = SumSQN2mol - SQavgN2mol;
```

```
rmsN2mol  =pow(flucN2mol,0.5);

SumSQH2Omol = SQH2Omol/counter;
SQavgH2Omol = pow(avgH2Omol,2.0);
flucH2Omol = SumSQH2Omol - SQavgH2Omol;
rmsH2Omol =pow(flucH2Omol,0.5);

SumSQH2mol = SQH2mol/counter;
SQavgH2mol = pow(avgH2mol,2.0);
flucH2mol = SumSQH2mol - SQavgH2mol;
rmsH2mol =pow(flucH2mol,0.5);

SumSQOHmol = SQOHmol/counter;
SQavgOHmol = pow(avgOHmol,2.0);
flucOHmol = SumSQOHmol - SQavgOHmol;
rmsOHmol =pow(flucOHmol,0.5);
fprintf(out,"|");

printf("What is mole fraction output filename?");
scanf("%s",filename);
out = fopen(filename,"a");
fprintf(out,"%.2f %.5f %.5f %6.1f %6.1f %.4f %.4f %.4f %.4f
        %.4f %.4f %.4f %.4f %.5f %.5f %6.1f %6.1f\n",
        x,avgMix,rmsMix,avgT,rmsT,avgO2mol,rmsO2mol,
        avgN2mol,rmsN2mol,avgH2Omol,rmsH2Omol,avgH2mol,
        rmsH2mol,avgOHmol,rmsOHmol,avgPT,rmsPT);

printf("avgMix avgT avgO2 avgN2 avgH2O avgH2 avgOH rmsMix rmsT\n");
printf("%.5f %6.1f %.4f %.4f %.4f %.4f %.4f %.5f %6.1f\n",
        avgMix,avgT,avgO2mol,avgN2mol,avgH2Omol,avgH2mol,
        avgOHmol,rmsMix,rmsT);

fclose(in);
fclose(out);
}
```

APPENDIX B

SUPERSONIC FLAME EXPERIMENTAL DATA

x/D = 0.85
Mole fraction data.
T in degrees K.

y/D	f	rmsf	T	rmsT	O_2	$rmsO_2$	N_2	$rmsN_2$
-4.31	0.00000	0.00000	280.4	15.5	0.2146	0.0116	0.7582	0.0347
-4.09	0.00000	0.00000	294.6	18.9	0.2160	0.0116	0.7533	0.0347
-3.87	0.00000	0.00000	641.3	199.4	0.2289	0.0137	0.7222	0.0358
-3.66	0.00000	0.00008	1102.2	87.7	0.2100	0.0166	0.5971	0.0374
-3.44	0.00024	0.00064	1255.2	97.3	0.2007	0.0176	0.5548	0.0357
-3.01	0.00068	0.00129	1262.9	102.3	0.1975	0.0198	0.5416	0.0361
-2.80	0.00076	0.00131	1289.0	107.6	0.1926	0.0189	0.5418	0.0347
-2.58	0.00065	0.00122	1275.3	97.7	0.1940	0.0178	0.5415	0.0351
-2.37	0.00068	0.00116	1279.4	98.2	0.1922	0.0177	0.5419	0.0335
-2.15	0.00111	0.00156	1269.8	109.5	0.1885	0.0186	0.5358	0.0340
-1.94	0.00125	0.00156	1269.4	107.5	0.1875	0.0182	0.5354	0.0341
-1.72	0.00097	0.00136	1273.3	106.3	0.1871	0.0180	0.5393	0.0340
-1.51	0.00189	0.00190	1263.2	110.3	0.1831	0.0169	0.5269	0.0337
-1.29	0.00126	0.00166	1259.4	106.8	0.1865	0.0172	0.5344	0.0350
-1.08	0.00117	0.00154	1253.4	113.3	0.1893	0.0189	0.5344	0.0356
-0.86	0.00083	0.00133	1225.8	194.2	0.1859	0.0188	0.5456	0.0361
-0.65	0.02980	0.01028	1143.3	100.3	0.1507	0.0253	0.3683	0.0461
-0.43	0.70086	0.11747	860.9	91.5	0.0000	0.0000	0.0200	0.0131
-0.22	0.99510	0.04577	693.2	113.3	0.0000	0.0000	0.0001	0.0007
0.00	0.99753	0.04469	622.1	131.3	0.0000	0.0000	0.0000	0.0000
0.22	0.91041	0.10219	547.5	76.5	0.0003	0.0048	0.0073	0.0137
0.43	0.16347	0.04962	648.0	94.8	0.0917	0.0337	0.1384	0.0298
0.65	0.01090	0.00618	1252.8	221.4	0.1588	0.0262	0.4805	0.0524
0.86	0.00170	0.00190	1245.7	124.0	0.1897	0.0204	0.5244	0.0333
1.08	0.00191	0.00188	1316.4	126.8	0.1797	0.0195	0.5295	0.0335
1.29	0.00182	0.00195	1316.2	129.0	0.1822	0.0215	0.5309	0.0333
1.51	0.00177	0.00195	1317.9	125.3	0.1841	0.0198	0.5286	0.0336
1.72	0.00158	0.00193	1322.2	123.0	0.1881	0.0218	0.5291	0.0328
1.94	0.00114	0.00171	1301.8	123.3	0.1935	0.0242	0.5338	0.0333
2.15	0.00092	0.00149	1291.9	123.5	0.1967	0.0224	0.5349	0.0327
2.37	0.00076	0.00133	1306.3	118.1	0.1969	0.0241	0.5379	0.0340
2.58	0.00042	0.00103	1246.0	116.7	0.2094	0.0233	0.5367	0.0321
2.80	0.00036	0.00094	1241.9	118.9	0.2107	0.0237	0.5404	0.0333
3.01	0.00024	0.00071	1239.8	112.1	0.2092	0.0228	0.5474	0.0327
3.23	0.00009	0.00038	1234.8	118.4	0.2108	0.0220	0.5521	0.0333
3.44	0.00009	0.00036	1199.5	103.5	0.2120	0.0208	0.5511	0.0321
3.66	0.00000	0.00000	1014.7	87.7	0.2118	0.0162	0.6001	0.0349

y/D	f	rmsf	T	rmsT	O_2	$rmsO_2$	N_2	$rmsN_2$
3.87	0.00000	0.00000	481.9	167.9	0.2086	0.0127	0.7254	0.0351
4.09	0.00000	0.00000	310.2	19.1	0.2119	0.0119	0.7599	0.0349
4.31	0.00000	0.00000	298.1	16.1	0.2164	0.0118	0.7594	0.0348

x/D = 0.85

Mole fraction data.

y/D	H_2O	$rmsH_2O$	H_2	$rmsH_2$	OH	rmsOH
-4.31	0.0252	0.0028	0.0000	0.0001	0.0000	0.0000
-4.09	0.0286	0.0040	0.0000	0.0001	0.0000	0.0000
-3.87	0.0469	0.0142	0.0000	0.0001	0.0000	0.0000
-3.66	0.1909	0.0311	0.0000	0.0000	0.0000	0.0000
-3.44	0.2424	0.0340	0.0000	0.0004	0.0000	0.0000
-3.01	0.2588	0.0358	0.0000	0.0003	0.0000	0.0000
-2.80	0.2635	0.0329	0.0000	0.0002	0.0000	0.0000
-2.58	0.2624	0.0321	0.0000	0.0000	0.0000	0.0000
-2.37	0.2639	0.0308	0.0000	0.0004	0.0000	0.0000
-2.15	0.2737	0.0315	0.0000	0.0004	0.0000	0.0000
-1.94	0.2751	0.0335	0.0000	0.0000	0.0000	0.0000
-1.72	0.2716	0.0306	0.0000	0.0002	0.0000	0.0000
-1.51	0.2879	0.0312	0.0000	0.0005	0.0000	0.0000
-1.29	0.2770	0.0317	0.0000	0.0005	0.0000	0.0000
-1.08	0.2744	0.0322	0.0000	0.0002	0.0000	0.0000
-0.86	0.2665	0.0320	0.0000	0.0004	0.0000	0.0000
-0.65	0.2071	0.0261	0.2718	0.0678	0.0000	0.0000
-0.43	0.0194	0.0087	0.9586	0.0469	0.0000	0.0000
-0.22	0.0002	0.0006	0.9977	0.0446	0.0000	0.0000
0.00	0.0001	0.0003	0.9979	0.0446	0.0000	0.0000
0.22	0.0006	0.0019	0.9898	0.0484	0.0000	0.0000
0.43	0.0326	0.0101	0.7354	0.0658	0.0000	0.0000
0.65	0.2354	0.0330	0.1233	0.0502	0.0000	0.0000
0.86	0.2839	0.0326	0.0000	0.0005	0.0000	0.0000
1.08	0.2888	0.0307	0.0000	0.0002	0.0000	0.0000
1.29	0.2849	0.0342	0.0000	0.0000	0.0000	0.0000
1.51	0.2851	0.0332	0.0001	0.0019	0.0000	0.0000
1.72	0.2807	0.0343	0.0000	0.0000	0.0000	0.0000
1.94	0.2703	0.0375	0.0002	0.0023	0.0000	0.0000
2.15	0.2662	0.0344	0.0000	0.0000	0.0000	0.0000
2.37	0.2629	0.0334	0.0000	0.0000	0.0000	0.0000

x/D = 0.85

y/D	H$_2$O	rmsH$_2$O	H$_2$	rmsH$_2$	OH	rmsOH
2.58	0.2517	0.0333	0.0000	0.0000	0.0000	0.0000
2.80	0.2468	0.0345	0.0000	0.0000	0.0000	0.0000
3.01	0.2412	0.0336	0.0000	0.0000	0.0000	0.0000
3.23	0.2348	0.0302	0.0000	0.0000	0.0000	0.0000
3.44	0.2348	0.0303	0.0000	0.0000	0.0000	0.0000
3.66	0.1861	0.0253	0.0000	0.0000	0.0000	0.0000
3.87	0.0640	0.0114	0.0000	0.0000	0.0000	0.0000
4.09	0.0262	0.0032	0.0000	0.0002	0.0000	0.0000
4.31	0.0221	0.0025	0.0000	0.0002	0.0000	0.0000

x/D = 10.8

Mole fraction data.

y/D	f	rmsf	T	rmsT	O$_2$	rmsO$_2$	N$_2$	rmsN$_2$
-6.78	0.00000	0.00000	295.5	30.7	0.2157	0.0117	0.7605	0.0348
-6.46	0.00000	0.00000	297.5	39.4	0.2157	0.0118	0.7610	0.0348
-6.13	0.00000	0.00000	295.5	17.4	0.2156	0.0118	0.7606	0.0349
-5.81	0.00000	0.00000	298.1	50.1	0.2163	0.0121	0.7595	0.0349
-5.49	0.00000	0.00000	302.7	27.6	0.2167	0.0120	0.7581	0.0350
-5.17	0.00000	0.00000	321.4	66.8	0.2173	0.0124	0.7549	0.0355
-4.84	0.00000	0.00000	369.0	96.5	0.2187	0.0131	0.7456	0.0358
-4.52	0.00000	0.00000	460.6	144.2	0.2193	0.0133	0.7336	0.0368
-4.20	0.00000	0.00000	614.2	194.2	0.2160	0.0140	0.7189	0.0379
-3.87	0.00000	0.00000	809.7	157.6	0.2118	0.0145	0.6952	0.0394
-3.55	0.00000	0.00000	928.7	113.6	0.2094	0.0146	0.6647	0.0423
-3.23	0.00000	0.00000	1058.1	110.0	0.2041	0.0155	0.6201	0.0412
-2.91	0.00003	0.00019	1187.2	103.8	0.1957	0.0164	0.5822	0.0369
-2.58	0.00013	0.00040	1275.6	100.6	0.1940	0.0176	0.5562	0.0327
-2.26	0.00024	0.00058	1299.1	105.0	0.1950	0.0180	0.5468	0.0309
-1.94	0.00023	0.00058	1310.5	100.6	0.1941	0.0168	0.5471	0.0306
-1.61	0.00015	0.00045	1318.1	100.6	0.1926	0.0162	0.5511	0.0309
-1.29	0.00016	0.00049	1331.2	100.2	0.1912	0.0161	0.5509	0.0308
-0.97	0.00096	0.00469	1326.3	106.0	0.1901	0.0181	0.5452	0.0411
-0.65	0.02140	0.02815	1212.2	165.7	0.1620	0.0391	0.4425	0.1075
-0.32	0.12480	0.05100	840.0	307.5	0.0816	0.0271	0.1910	0.0750
0.00	0.22106	0.05209	555.8	240.2	0.0606	0.0214	0.1004	0.0312
0.32	0.20185	0.05025	713.1	353.8	0.0549	0.0226	0.1218	0.0379
0.65	0.08629	0.03558	1101.6	244.2	0.0825	0.0287	0.2603	0.0644

x/D = 10.8
Mole fraction data.

y/D	f	rmsf	T	rmsT	O_2	$rmsO_2$	N_2	$rmsN_2$
0.97	0.01633	0.01673	1309.8	129.3	0.1620	0.0344	0.4554	0.0759
1.29	0.00064	0.00249	1353.2	123.4	0.1968	0.0207	0.5428	0.0532
1.61	0.00012	0.00044	1354.4	141.2	0.2010	0.0221	0.5557	0.0304
1.94	0.00001	0.00011	1343.4	114.8	0.2062	0.0194	0.5642	0.0303
2.26	0.00001	0.00016	1318.2	112.7	0.2118	0.0205	0.5657	0.0306
2.58	0.00001	0.00013	1294.2	111.5	0.2178	0.0205	0.5655	0.0306
2.91	0.00000	0.00003	1267.4	108.9	0.2193	0.0208	0.5668	0.0308
3.23	0.00000	0.00007	1236.5	114.5	0.2227	0.0211	0.5691	0.0314
3.55	0.00000	0.00000	1167.7	110.9	0.2261	0.0199	0.5776	0.0332
3.87	0.00000	0.00000	1089.7	102.5	0.2237	0.0182	0.6009	0.0357
4.20	0.00000	0.00000	1001.4	99.7	0.2200	0.0165	0.6345	0.0397
4.52	0.00000	0.00000	885.1	120.3	0.2187	0.0157	0.6734	0.0397
4.84	0.00000	0.00000	731.2	179.0	0.2160	0.0137	0.7069	0.0388
5.17	0.00000	0.00000	569.2	180.6	0.2163	0.0138	0.7278	0.0375
5.49	0.00000	0.00000	437.6	122.2	0.2135	0.0132	0.7454	0.0372
5.81	0.00000	0.00000	357.8	63.0	0.2080	0.0132	0.7613	0.0368
6.13	0.00000	0.00000	325.8	51.2	0.2083	0.0130	0.7659	0.0361
6.46	0.00000	0.00000	311.5	20.5	0.2063	0.0128	0.7701	0.0358
6.78	0.00000	0.00000	309.5	18.7	0.2065	0.0128	0.7703	0.0358
7.10	0.00000	0.00000	310.1	52.6	0.2092	0.0136	0.7675	0.0359
7.43	0.00000	0.00000	305.1	17.3	0.2121	0.0134	0.7644	0.0357

x/D = 10.8
Mole fraction data.

y/D	H_2O	$rmsH_2O$	H_2	$rmsH_2$	OH	rmsOH
-6.78	0.0217	0.0025	0.0000	0.0000	0.0000	0.0000
-6.46	0.0213	0.0025	0.0000	0.0001	0.0000	0.0000
-6.13	0.0218	0.0024	0.0000	0.0000	0.0000	0.0000
-5.81	0.0223	0.0027	0.0000	0.0000	0.0000	0.0000
-5.49	0.0232	0.0040	0.0000	0.0000	0.0000	0.0000
-5.17	0.0256	0.0067	0.0000	0.0000	0.0000	0.0000
-4.84	0.0328	0.0117	0.0000	0.0000	0.0000	0.0000
-4.52	0.0451	0.0150	0.0000	0.0000	0.0000	0.0000
-4.20	0.0631	0.0210	0.0000	0.0000	0.0000	0.0000
-3.87	0.0910	0.0250	0.0000	0.0000	0.0000	0.0000

x/D = 10.8
Mole fraction data.

y/D	H_2O	rmsH_2O	H_2	rmsH_2	OH	rmsOH
-3.55	0.1239	0.0312	0.0000	0.0000	0.0000	0.0000
-3.23	0.1737	0.0331	0.0000	0.0000	0.0000	0.0000
-2.91	0.2197	0.0298	0.0000	0.0000	0.0003	0.0005
-2.58	0.2468	0.0261	0.0000	0.0000	0.0010	0.0010
-2.26	0.2547	0.0253	0.0000	0.0000	0.0014	0.0010
-1.94	0.2552	0.0241	0.0000	0.0000	0.0016	0.0010
-1.61	0.2525	0.0232	0.0000	0.0000	0.0017	0.0010
-1.29	0.2541	0.0226	0.0000	0.0000	0.0019	0.0010
-0.97	0.2527	0.0246	0.0081	0.0423	0.0018	0.0010
-0.65	0.2182	0.0485	0.1743	0.1847	0.0010	0.0010
-0.32	0.1049	0.0418	0.6204	0.1315	0.0001	0.0004
0.00	0.0551	0.0175	0.7820	0.0637	0.0000	0.0000
0.32	0.0620	0.0192	0.7593	0.0670	0.0000	0.0000
0.65	0.1259	0.0336	0.5294	0.1128	0.0000	0.0002
0.97	0.2158	0.0415	0.1641	0.1326	0.0007	0.0010
1.29	0.2520	0.0331	0.0049	0.0262	0.0015	0.0010
1.61	0.2397	0.0245	0.0000	0.0000	0.0017	0.0010
1.94	0.2259	0.0243	0.0000	0.0000	0.0017	0.0010
2.26	0.2191	0.0246	0.0000	0.0000	0.0015	0.0009
2.58	0.2134	0.0238	0.0000	0.0000	0.0014	0.0009
2.91	0.2109	0.0245	0.0000	0.0000	0.0010	0.0008
3.23	0.2055	0.0254	0.0000	0.0000	0.0007	0.0007
3.55	0.1940	0.0265	0.0000	0.0000	0.0003	0.0005
3.87	0.1734	0.0254	0.0000	0.0001	0.0000	0.0001
4.20	0.1436	0.0274	0.0000	0.0000	0.0000	0.0000
4.52	0.1059	0.0232	0.0000	0.0000	0.0000	0.0000
4.84	0.0751	0.0211	0.0000	0.0000	0.0000	0.0000
5.17	0.0539	0.0149	0.0000	0.0000	0.0000	0.0000
5.49	0.0391	0.0111	0.0000	0.0000	0.0000	0.0000
5.81	0.0287	0.0076	0.0000	0.0000	0.0000	0.0000
6.13	0.0238	0.0050	0.0000	0.0000	0.0000	0.0000
6.46	0.0216	0.0026	0.0000	0.0000	0.0000	0.0000
6.78	0.0213	0.0024	0.0000	0.0000	0.0000	0.0000
7.10	0.0213	0.0025	0.0000	0.0000	0.0000	0.0000
7.43	0.0214	0.0024	0.0000	0.0000	0.0000	0.0000

x/D = 21.5
Mole fraction data.

y/D	f	rmsf	T	rmsT	O_2	$rmsO_2$	N_2	$rmsN_2$
-9.04	0.00000	0.00000	316.4	23.3	0.2063	0.0113	0.7677	0.0357
-8.61	0.00000	0.00000	317.0	34.1	0.2053	0.0112	0.7685	0.0357
-8.18	0.00000	0.00000	336.4	100.0	0.2057	0.0120	0.7676	0.0364
-7.75	0.00000	0.00000	327.7	75.1	0.2051	0.0114	0.7681	0.0358
-7.32	0.00000	0.00000	341.0	97.5	0.2050	0.0117	0.7668	0.0361
-6.89	0.00001	0.00026	365.8	135.1	0.2036	0.0123	0.7658	0.0371
-6.46	0.00000	0.00000	390.8	155.0	0.2036	0.0121	0.7639	0.0364
-6.03	0.00000	0.00000	481.5	219.2	0.2027	0.0124	0.7576	0.0378
-5.60	0.00000	0.00000	588.4	247.6	0.1998	0.0127	0.7519	0.0395
-5.17	0.00000	0.00000	689.9	240.9	0.1972	0.0138	0.7445	0.0410
-4.74	0.00000	0.00000	835.3	206.8	0.1936	0.0140	0.7279	0.0440
-4.31	0.00000	0.00000	948.0	178.1	0.1900	0.0146	0.7095	0.0473
-3.87	0.00000	0.00000	1058.5	149.7	0.1857	0.0151	0.6888	0.0499
-3.44	0.00001	0.00013	1176.1	172.6	0.1799	0.0154	0.6623	0.0532
-3.01	0.00006	0.00035	1269.4	168.0	0.1751	0.0168	0.6385	0.0543
-2.58	0.00031	0.00097	1400.6	203.8	0.1668	0.0198	0.6179	0.0550
-2.15	0.00052	0.00116	1474.7	165.0	0.1600	0.0185	0.6039	0.0503
-1.72	0.00093	0.00150	1511.2	153.2	0.1566	0.0171	0.5919	0.0502
-1.29	0.00075	0.00171	1545.8	147.8	0.1551	0.0173	0.5993	0.0450
-0.86	0.01660	0.03246	1542.7	179.7	0.1403	0.0418	0.4813	0.1045
-0.43	0.06303	0.05039	1375.0	288.9	0.0872	0.0487	0.3658	0.1445
0.00	0.09688	0.04070	1364.1	372.2	0.0505	0.0378	0.2696	0.0794
0.43	0.05444	0.03458	1670.9	312.2	0.0550	0.0342	0.3765	0.1298
0.86	0.03215	0.02542	1917.3	271.6	0.0812	0.0454	0.4202	0.0965
1.29	0.01405	0.01031	1910.5	209.6	0.1131	0.0414	0.5005	0.0647
1.72	0.00884	0.00511	1807.8	188.3	0.1386	0.0155	0.5238	0.0544
2.15	0.00129	0.00194	1760.1	184.0	0.1256	0.0155	0.6127	0.0457
2.58	0.00060	0.00121	1715.0	209.5	0.1329	0.0158	0.6212	0.0455
3.01	0.00036	0.00099	1658.5	198.5	0.1436	0.0169	0.6267	0.0483
3.44	0.00010	0.00045	1551.4	224.1	0.1547	0.0178	0.6362	0.0498
3.87	0.00004	0.00035	1413.2	194.7	0.1689	0.0189	0.6520	0.0558
4.31	0.00000	0.00002	1290.9	177.6	0.1769	0.0192	0.6721	0.0556
4.74	0.00004	0.00171	1168.8	170.2	0.1849	0.0161	0.6963	0.0513
5.17	0.00000	0.00000	970.4	160.3	0.1919	0.0155	0.7389	0.0483
5.60	0.00000	0.00000	882.3	192.1	0.1927	0.0131	0.7512	0.0476
6.03	0.00000	0.00000	777.3	228.4	0.1957	0.0133	0.7594	0.0464
6.46	0.00000	0.00000	669.7	253.5	0.1985	0.0133	0.7637	0.0438
6.89	0.00000	0.00000	579.4	248.3	0.1989	0.0131	0.7702	0.0394

x/D = 21.5
Mole fraction data.

y/D	f	rmsf	T	rmsT	O_2	$rmsO_2$	N_2	$rmsN_2$
7.32	0.00000	0.00000	499.4	231.5	0.2002	0.0126	0.7729	0.0371
7.75	0.00000	0.00000	459.5	211.1	0.2005	0.0124	0.7749	0.0360
8.18	0.00000	0.00000	459.9	213.0	0.1975	0.0125	0.7800	0.0360
8.61	0.00000	0.00000	469.2	218.8	0.1943	0.0120	0.7821	0.0361
9.04	0.00000	0.00000	440.7	203.9	0.1952	0.0120	0.7817	0.0361
9.47	0.00000	0.00000	453.3	208.5	0.1939	0.0119	0.7828	0.0362

x/D = 21.5
Mole fraction data.

y/D	H_2O	$rmsH_2O$	H_2	$rmsH_2$	OH	rmsOH
-9.04	0.0240	0.0069	0.0000	0.0000	0.0000	0.0000
-8.61	0.0242	0.0072	0.0000	0.0000	0.0000	0.0000
-8.18	0.0243	0.0074	0.0000	0.0000	0.0000	0.0000
-7.75	0.0248	0.0075	0.0000	0.0000	0.0000	0.0000
-7.32	0.0261	0.0083	0.0000	0.0000	0.0000	0.0000
-6.89	0.0282	0.0100	0.0000	0.0000	0.0000	0.0000
-6.46	0.0305	0.0125	0.0000	0.0000	0.0000	0.0000
-6.03	0.0377	0.0179	0.0000	0.0000	0.0000	0.0000
-5.60	0.0463	0.0226	0.0000	0.0000	0.0000	0.0000
-5.17	0.0564	0.0270	0.0000	0.0000	0.0000	0.0000
-4.74	0.0764	0.0340	0.0000	0.0000	0.0000	0.0000
-4.31	0.0985	0.0405	0.0000	0.0000	0.0000	0.0000
-3.87	0.1235	0.0446	0.0000	0.0000	0.0000	0.0000
-3.44	0.1558	0.0502	0.0000	0.0000	0.0000	0.0000
-3.01	0.1844	0.0542	0.0000	0.0000	0.0000	0.0000
-2.58	0.2132	0.0541	0.0000	0.0000	0.0001	0.0004
-2.15	0.2339	0.0499	0.0000	0.0000	0.0003	0.0005
-1.72	0.2491	0.0479	0.0000	0.0000	0.0004	0.0006
-1.29	0.2436	0.0459	0.0008	0.0117	0.0007	0.0008
-0.86	0.2715	0.0673	0.0734	0.1671	0.0015	0.0021
-0.43	0.1579	0.0679	0.3878	0.2427	0.0005	0.0013
0.00	0.1358	0.0602	0.5415	0.1401	0.0005	0.0021
0.43	0.2205	0.0962	0.3436	0.1898	0.0036	0.0053
0.86	0.3691	0.1006	0.1151	0.1597	0.0125	0.0098
1.29	0.3631	0.0729	0.0119	0.0547	0.0109	0.0076
1.72	0.3306	0.0567	0.0002	0.0033	0.0049	0.0034

x/D = 21.5
Mole fraction data.

y/D	H_2O	rmsH_2O	H_2	rmsH_2	OH	rmsOH
2.15	0.2589	0.0459	0.0000	0.0000	0.0022	0.0015
2.58	0.2422	0.0431	0.0000	0.0000	0.0018	0.0015
3.01	0.2279	0.0449	0.0000	0.0000	0.0013	0.0013
3.44	0.2064	0.0462	0.0000	0.0000	0.0007	0.0011
3.87	0.1783	0.0485	0.0000	0.0000	0.0002	0.0006
4.31	0.1490	0.0430	0.0000	0.0000	0.0000	0.0003
4.74	0.1180	0.0392	0.0003	0.0001	0.0000	0.0002
5.17	0.0687	0.0261	0.0000	0.0000	0.0000	0.0000
5.60	0.0541	0.0205	0.0000	0.0000	0.0000	0.0000
6.03	0.0444	0.0179	0.0000	0.0000	0.0000	0.0000
6.46	0.0358	0.0135	0.0000	0.0000	0.0000	0.0000
6.89	0.0289	0.0098	0.0000	0.0000	0.0000	0.0000
7.32	0.0250	0.0070	0.0000	0.0000	0.0000	0.0000
7.75	0.0226	0.0050	0.0000	0.0000	0.0000	0.0000
8.18	0.0219	0.0041	0.0000	0.0000	0.0000	0.0000
8.61	0.0216	0.0037	0.0000	0.0000	0.0000	0.0000
9.04	0.0211	0.0035	0.0000	0.0000	0.0000	0.0000
9.47	0.0214	0.0036	0.0000	0.0000	0.0000	0.0000

x/D = 32.3
Mole fraction data.

y/D	f	rmsf	T	rmsT	O_2	rmsO_2	N_2	rmsN_2
-10.76	0.00000	0.00000	330.5	37.8	0.2313	0.0117	0.7352	0.0352
-10.22	0.00000	0.00000	330.8	74.5	0.2333	0.0145	0.7372	0.0370
-9.69	0.00000	0.00000	340.2	88.3	0.2328	0.0145	0.7368	0.0368
-9.15	0.00000	0.00000	351.0	95.7	0.2317	0.0142	0.7361	0.0370
-8.61	0.00000	0.00000	377.1	130.5	0.2297	0.0160	0.7366	0.0375
-8.07	0.00000	0.00000	424.3	166.9	0.2270	0.0176	0.7351	0.0383
-7.53	0.00000	0.00000	502.6	218.3	0.2215	0.0197	0.7343	0.0392
-7.00	0.00000	0.00000	567.5	232.8	0.2163	0.0209	0.7331	0.0407
-6.46	0.00000	0.00000	653.9	234.8	0.2110	0.0216	0.7312	0.0417
-5.92	0.00000	0.00000	736.4	229.1	0.2046	0.0216	0.7272	0.0428
-5.38	0.00000	0.00000	819.1	208.1	0.1996	0.0196	0.7212	0.0432
-4.84	0.00000	0.00000	915.6	189.4	0.1919	0.0204	0.7135	0.0450
-4.31	0.00000	0.00000	985.9	165.8	0.1864	0.0177	0.7006	0.0479
-3.77	0.00001	0.00016	1102.4	158.5	0.1756	0.0187	0.6741	0.0528

x/D = 32.3
Mole fraction data.

y/D	f	rmsf	T	rmsT	O_2	$rmsO_2$	N_2	$rmsN_2$
-3.23	0.00016	0.00074	1201.0	156.9	0.1642	0.0198	0.6503	0.0560
-2.69	0.00054	0.00161	1307.7	164.4	0.1517	0.0206	0.6246	0.0562
-2.15	0.00096	0.00188	1402.5	165.8	0.1426	0.0209	0.5850	0.0579
-1.61	0.00819	0.01090	1510.0	181.6	0.1291	0.0311	0.5455	0.0693
-1.08	0.02374	0.02774	1543.0	225.7	0.1156	0.0448	0.4692	0.0820
-0.54	0.04577	0.03445	1702.9	251.5	0.0830	0.0516	0.3791	0.0835
0.00	0.05969	0.02886	1759.6	363.9	0.0507	0.0583	0.3168	0.0913
0.54	0.04728	0.01989	1954.1	397.6	0.0462	0.0560	0.3453	0.0837
1.08	0.03497	0.01488	2001.7	350.7	0.0420	0.0537	0.3965	0.0891
1.61	0.02344	0.01242	1945.5	304.3	0.0649	0.0477	0.4585	0.0855
2.15	0.01382	0.00956	1797.9	271.9	0.1009	0.0439	0.5126	0.0802
2.69	0.00846	0.00587	1689.2	207.8	0.1266	0.0333	0.5441	0.0579
3.23	0.00630	0.00515	1615.2	219.5	0.1407	0.0341	0.5822	0.0603
3.77	0.00085	0.00174	1537.3	198.9	0.1475	0.0271	0.6202	0.0485
4.31	0.00021	0.00088	1422.5	235.0	0.1543	0.0272	0.6423	0.0454
4.84	0.00002	0.00027	1312.1	177.8	0.1674	0.0212	0.6635	0.0441
5.38	0.00000	0.00000	1198.9	156.5	0.1782	0.0190	0.6843	0.0431
5.92	0.00002	0.00089	1103.3	150.5	0.1856	0.0170	0.7043	0.0429
6.46	0.00000	0.00000	1030.4	141.1	0.1896	0.0167	0.7184	0.0420
7.00	0.00000	0.00000	946.5	164.7	0.1941	0.0178	0.7339	0.0423
7.53	0.00000	0.00000	851.2	202.0	0.1980	0.0172	0.7441	0.0424
8.07	0.00000	0.00000	779.7	227.5	0.1981	0.0181	0.7540	0.0415
8.61	0.00000	0.00000	697.8	247.1	0.2026	0.0200	0.7568	0.0407
9.15	0.00000	0.00000	590.5	245.6	0.2098	0.0206	0.7568	0.0403
9.69	0.00000	0.00000	530.9	236.3	0.2098	0.0200	0.7602	0.0403
10.22	0.00000	0.00000	450.7	208.7	0.2175	0.0194	0.7559	0.0395
10.76	0.00000	0.00000	436.8	200.4	0.2146	0.0178	0.7601	0.0389
11.30	0.00000	0.00000	418.0	184.0	0.2128	0.0172	0.7625	0.0388
11.84	0.00000	0.00000	414.2	194.8	0.2138	0.0187	0.7615	0.0389
12.38	0.00000	0.00000	425.2	191.9	0.2104	0.0176	0.7651	0.0389

x/D = 32.3
Mole fraction data.

y/D	H$_2$O	rmsH$_2$O	H$_2$	rmsH$_2$	OH	rmsOH
-10.76	0.0313	0.0048	0.0000	0.0000	0.0000	0.0000
-10.22	0.0272	0.0084	0.0000	0.0000	0.0000	0.0000
-9.69	0.0282	0.0087	0.0000	0.0000	0.0000	0.0000
-9.15	0.0300	0.0100	0.0000	0.0000	0.0000	0.0000
-8.61	0.0315	0.0126	0.0000	0.0000	0.0000	0.0000
-8.07	0.0357	0.0144	0.0000	0.0000	0.0000	0.0000
-7.53	0.0419	0.0176	0.0001	0.0013	0.0000	0.0001
-7.00	0.0484	0.0202	0.0000	0.0000	0.0000	0.0000
-6.46	0.0556	0.0240	0.0000	0.0000	0.0000	0.0000
-5.92	0.0659	0.0277	0.0000	0.0000	0.0000	0.0000
-5.38	0.0770	0.0300	0.0000	0.0000	0.0000	0.0000
-4.84	0.0924	0.0335	0.0000	0.0000	0.0000	0.0004
-4.31	0.1108	0.0396	0.0000	0.0000	0.0000	0.0000
-3.77	0.1480	0.0490	0.0000	0.0000	0.0000	0.0002
-3.23	0.1831	0.0568	0.0000	0.0000	0.0001	0.0004
-2.69	0.2206	0.0567	0.0005	0.0108	0.0004	0.0007
-2.15	0.2606	0.0581	0.0000	0.0000	0.0009	0.0012
-1.61	0.3005	0.0671	0.0118	0.0611	0.0025	0.0033
-1.08	0.3119	0.0797	0.0980	0.1644	0.0032	0.0042
-0.54	0.3166	0.1047	0.2160	0.1930	0.0048	0.0063
0.00	0.3618	0.1117	0.2619	0.1631	0.0069	0.0079
0.54	0.4304	0.1169	0.1618	0.1326	0.0158	0.0117
1.08	0.4738	0.0932	0.0631	0.0908	0.0225	0.0138
1.61	0.4408	0.0925	0.0166	0.0456	0.0187	0.0140
2.15	0.3725	0.0902	0.0023	0.0163	0.0097	0.0100
2.69	0.3243	0.0647	0.0001	0.0050	0.0045	0.0053
3.23	0.2980	0.0657	0.0000	0.0000	0.0027	0.0028
3.77	0.2387	0.0543	0.0000	0.0000	0.0018	0.0019
4.31	0.2001	0.0520	0.0000	0.0000	0.0011	0.0028
4.84	0.1681	0.0472	0.0000	0.0000	0.0004	0.0021
5.38	0.1352	0.0417	0.0000	0.0000	0.0001	0.0003
5.92	0.1094	0.0357	0.0002	0.0077	0.0000	0.0003
6.46	0.0898	0.0308	0.0000	0.0000	0.0000	0.0000
7.00	0.0696	0.0233	0.0001	0.0021	0.0000	0.0004
7.53	0.0557	0.0221	0.0000	0.0000	0.0000	0.0000
8.07	0.0457	0.0181	0.0000	0.0000	0.0000	0.0000
8.61	0.0383	0.0147	0.0000	0.0000	0.0000	0.0000
9.15	0.0312	0.0113	0.0000	0.0000	0.0000	0.0000

x/D = 32.3
Mole fraction data.

y/D	H_2O	$rmsH_2O$	H_2	$rmsH_2$	OH	rmsOH
9.69	0.0278	0.0093	0.0000	0.0000	0.0000	0.0000
10.22	0.0244	0.0067	0.0000	0.0000	0.0000	0.0000
10.76	0.0232	0.0054	0.0000	0.0000	0.0000	0.0000
11.30	0.0225	0.0049	0.0000	0.0000	0.0000	0.0000
11.84	0.0224	0.0063	0.0001	0.0018	0.0000	0.0005
12.38	0.0222	0.0044	0.0000	0.0000	0.0000	0.0000

x/D = 43.1
Mole fraction data.

y/D	f	rmsf	T	rmsT	O_2	$rmsO_2$	N_2	$rmsN_2$
-12.27	0.00000	0.00000	469.6	210.0	0.1839	0.0119	0.7912	0.0370
-11.62	0.00000	0.00000	510.4	227.5	0.1858	0.0131	0.7868	0.0380
-10.98	0.00000	0.00000	547.6	237.1	0.1889	0.0135	0.7812	0.0377
-10.33	0.00000	0.00000	609.1	249.2	0.1907	0.0139	0.7762	0.0377
-9.69	0.00000	0.00000	698.5	237.8	0.1913	0.0133	0.7707	0.0383
-9.04	0.00000	0.00000	763.8	215.9	0.1928	0.0132	0.7628	0.0387
-8.39	0.00000	0.00000	810.1	202.5	0.1929	0.0130	0.7571	0.0388
-7.75	0.00000	0.00000	871.8	168.3	0.1918	0.0130	0.7509	0.0396
-7.10	0.00000	0.00000	928.0	144.9	0.1916	0.0133	0.7421	0.0405
-6.46	0.00000	0.00000	990.2	144.3	0.1909	0.0139	0.7289	0.0410
-5.81	0.00000	0.00007	1062.7	155.4	0.1885	0.0147	0.7152	0.0422
-5.17	0.00000	0.00000	1146.3	156.7	0.1846	0.0152	0.7008	0.0440
-4.52	0.00000	0.00000	1238.0	156.4	0.1801	0.0153	0.6809	0.0454
-3.87	0.00006	0.00097	1328.8	170.6	0.1752	0.0179	0.6605	0.0487
-3.23	0.00055	0.00319	1424.7	197.4	0.1649	0.0261	0.6371	0.0519
-2.58	0.00258	0.00859	1533.9	210.1	0.1505	0.0377	0.6104	0.0626
-1.94	0.01383	0.01198	1683.4	290.0	0.1392	0.0599	0.5094	0.0760
-1.29	0.02338	0.01537	1824.0	342.4	0.1043	0.0625	0.4580	0.0811
-0.65	0.03916	0.01841	2069.3	403.3	0.0561	0.0654	0.3985	0.0941
0.00	0.04593	0.02087	2214.1	371.7	0.0337	0.0715	0.3841	0.1085
0.65	0.04360	0.01676	2303.8	433.4	0.0430	0.0665	0.3771	0.0999
1.29	0.01922	0.01265	2161.8	372.8	0.0872	0.0625	0.4763	0.0779
1.94	0.01037	0.00829	1891.7	336.8	0.1411	0.0618	0.5072	0.0570
2.58	0.00503	0.00598	1679.7	264.0	0.1510	0.0437	0.6053	0.0501
3.23	0.00012	0.00103	1547.2	235.4	0.1608	0.0275	0.6324	0.0451
3.87	0.00003	0.00048	1417.0	197.3	0.1739	0.0198	0.6532	0.0446

x/D = 43.1
Mole fraction data.

y/D	f	rmsf	T	rmsT	O_2	$rmsO_2$	N_2	$rmsN_2$
4.52	0.00000	0.00000	1300.7	178.6	0.1808	0.0178	0.6716	0.0440
5.17	0.00000	0.00000	1207.2	165.1	0.1862	0.0152	0.6867	0.0432
5.81	0.00000	0.00000	1127.4	163.1	0.1891	0.0155	0.7020	0.0420
6.46	0.00001	0.00035	1060.4	145.3	0.1913	0.0148	0.7170	0.0415
7.10	0.00000	0.00000	993.0	154.5	0.1923	0.0142	0.7282	0.0413
7.75	0.00000	0.00000	939.4	165.1	0.1923	0.0135	0.7402	0.0408
8.39	0.00000	0.00000	883.5	177.2	0.1916	0.0130	0.7480	0.0404
9.04	0.00000	0.00000	828.4	187.0	0.1900	0.0134	0.7576	0.0402
9.69	0.00000	0.00000	778.0	208.1	0.1887	0.0135	0.7663	0.0396
10.33	0.00000	0.00000	717.2	229.5	0.1882	0.0129	0.7711	0.0389
10.98	0.00000	0.00000	653.8	239.9	0.1898	0.0127	0.7738	0.0381
11.62	0.00000	0.00000	596.0	240.5	0.1887	0.0124	0.7806	0.0378
12.27	0.00000	0.00000	536.4	231.5	0.1855	0.0123	0.7857	0.0375

x/D = 43.1
Mole fraction data.

y/D	H_2O	$rmsH_2O$	H_2	$rmsH_2$	OH	rmsOH
-12.27	0.0229	0.0060	0.0000	0.0000	0.0000	0.0000
-11.62	0.0254	0.0082	0.0000	0.0001	0.0000	0.0000
-10.98	0.0279	0.0091	0.0000	0.0000	0.0000	0.0000
-10.33	0.0310	0.0097	0.0001	0.0000	0.0000	0.0003
-9.69	0.0361	0.0127	0.0000	0.0000	0.0000	0.0000
-9.04	0.0423	0.0155	0.0000	0.0000	0.0000	0.0000
-8.39	0.0480	0.0173	0.0000	0.0000	0.0000	0.0000
-7.75	0.0553	0.0199	0.0000	0.0000	0.0000	0.0000
-7.10	0.0644	0.0222	0.0000	0.0000	0.0000	0.0000
-6.46	0.0781	0.0255	0.0000	0.0000	0.0000	0.0000
-5.81	0.0943	0.0312	0.0000	0.0000	0.0000	0.0002
-5.17	0.1126	0.0346	0.0000	0.0000	0.0000	0.0001
-4.52	0.1369	0.0372	0.0000	0.0000	0.0000	0.0003
-3.87	0.1633	0.0426	0.0002	0.0042	0.0003	0.0012
-3.23	0.1928	0.0506	0.0024	0.0185	0.0008	0.0025
-2.58	0.2227	0.0581	0.0137	0.0553	0.0019	0.0041
-1.94	0.2980	0.0615	0.0460	0.0819	0.0054	0.0076
-1.29	0.3522	0.0655	0.0751	0.1103	0.0097	0.0094

x/D = 43.1
Mole fraction data.

y/D	H$_2$O	rmsH$_2$O	H$_2$	rmsH$_2$	OH	rmsOH
-0.65	0.3656	0.0704	0.1614	0.1193	0.0163	0.0113
0.00	0.3801	0.0796	0.2008	0.1268	0.0206	0.0125
0.65	0.3921	0.0876	0.1597	0.1166	0.0262	0.0139
1.29	0.3936	0.0851	0.0503	0.0513	0.0219	0.0111
1.94	0.3375	0.0775	0.0023	0.0164	0.0099	0.0100
2.58	0.2808	0.0625	0.0015	0.0157	0.0030	0.0061
3.23	0.2038	0.0443	0.0001	0.0022	0.0009	0.0022
3.87	0.1720	0.0406	0.0000	0.0000	0.0003	0.0009
4.52	0.1455	0.0384	0.0000	0.0000	0.0001	0.0003
5.17	0.1266	0.0362	0.0000	0.0000	0.0000	0.0002
5.81	0.1068	0.0305	0.0001	0.0001	0.0000	0.0005
6.46	0.0910	0.0290	0.0002	0.0000	0.0000	0.0000
7.10	0.0776	0.0249	0.0000	0.0000	0.0000	0.0000
7.75	0.0669	0.0228	0.0001	0.0003	0.0000	0.0000
8.39	0.0584	0.0189	0.0000	0.0000	0.0000	0.0000
9.04	0.0504	0.0168	0.0000	0.0000	0.0000	0.0000
9.69	0.0430	0.0140	0.0000	0.0000	0.0000	0.0000
10.33	0.0387	0.0128	0.0000	0.0000	0.0000	0.0000
10.98	0.0344	0.0114	0.0000	0.0000	0.0000	0.0000
11.62	0.0302	0.0093	0.0000	0.0000	0.0000	0.0000
12.27	0.0267	0.0075	0.0000	0.0000	0.0000	0.0000

x/D = 64.7
Mole fraction data.

y/D	f	rmsf	T	rmsT	O$_2$	rmsO$_2$	N$_2$	rmsN$_2$
-13.78	0.00000	0.00000	393.8	153.3	0.2173	0.0163	0.7492	0.0364
-12.92	0.00000	0.00000	409.6	157.0	0.2153	0.0170	0.7487	0.0370
-12.05	0.00000	0.00000	460.0	192.3	0.2123	0.0190	0.7476	0.0375
-11.19	0.00000	0.00000	511.0	213.2	0.2070	0.0204	0.7477	0.0383
-10.33	0.00000	0.00000	590.8	239.6	0.2010	0.0223	0.7464	0.0394
-9.47	0.00000	0.00000	695.4	243.2	0.2088	0.0216	0.7290	0.0406
-8.61	0.00000	0.00001	780.8	232.9	0.2027	0.0208	0.7242	0.0435
-7.75	0.00003	0.00044	868.1	232.6	0.1953	0.0228	0.7161	0.0465
-6.89	0.00001	0.00014	945.1	206.7	0.1892	0.0206	0.7086	0.0482
-6.03	0.00024	0.00155	1032.9	207.3	0.1814	0.0239	0.6955	0.0540
-5.17	0.00041	0.00182	1134.6	227.4	0.1700	0.0279	0.6812	0.0571

x/D = 64.7
Mole fraction data.

y/D	f	rmsf	T	rmsT	O_2	$rmsO_2$	N_2	$rmsN_2$
-4.31	0.00144	0.00402	1269.7	263.1	0.1529	0.0357	0.6607	0.0658
-3.44	0.00353	0.00580	1436.6	308.5	0.1315	0.0430	0.6336	0.0744
-2.58	0.00648	0.00784	1629.2	373.0	0.1051	0.0486	0.6083	0.0804
-1.72	0.01177	0.00903	1816.5	396.3	0.0809	0.0534	0.5862	0.0896
-0.86	0.01358	0.01022	2000.9	428.4	0.0567	0.0590	0.5640	0.0905
0.00	0.01743	0.01189	2093.6	434.2	0.0518	0.0646	0.5076	0.0904
0.86	0.01335	0.01000	2064.8	426.9	0.0528	0.0593	0.5688	0.0884
1.72	0.01026	0.00849	1840.2	402.2	0.0828	0.0540	0.5958	0.0839
2.58	0.00473	0.00698	1640.9	367.0	0.1128	0.0493	0.6227	0.0728
3.44	0.00180	0.00428	1436.9	267.9	0.1379	0.0391	0.6486	0.0620
4.31	0.00043	0.00185	1287.6	223.6	0.1630	0.0277	0.6745	0.0560
5.17	0.00012	0.00093	1186.3	193.2	0.1736	0.0235	0.6884	0.0506
6.03	0.00002	0.00025	1104.4	179.0	0.1811	0.0202	0.7090	0.0472
6.89	0.00001	0.00019	1032.7	175.2	0.1869	0.0190	0.7198	0.0423
7.75	0.00000	0.00000	960.1	176.4	0.1916	0.0177	0.7306	0.0425
8.61	0.00000	0.00000	923.2	182.5	0.1945	0.0184	0.7380	0.0410
9.47	0.00000	0.00000	839.4	214.2	0.2015	0.0192	0.7442	0.0394
10.33	0.00000	0.00000	768.3	232.0	0.2048	0.0204	0.7484	0.0383
11.19	0.00000	0.00000	677.5	249.3	0.2102	0.0214	0.7495	0.0384
12.05	0.00000	0.00000	653.1	249.4	0.2105	0.0210	0.7530	0.0383
12.92	0.00000	0.00000	556.4	239.8	0.2177	0.0211	0.7509	0.0380
13.78	0.00000	0.00000	531.7	232.5	0.2180	0.0204	0.7530	0.0380

x/D = 64.7
Mole fraction data.

y/D	H_2O	$rmsH_2O$	H_2	$rmsH_2$	OH	rmsOH
-13.78	0.0315	0.0137	0.0000	0.0000	0.0000	0.0000
-12.92	0.0341	0.0145	0.0000	0.0000	0.0000	0.0000
-12.05	0.0381	0.0167	0.0000	0.0000	0.0000	0.0000
-11.19	0.0433	0.0218	0.0000	0.0000	0.0000	0.0000
-10.33	0.0505	0.0255	0.0000	0.0000	0.0000	0.0000
-9.47	0.0602	0.0293	0.0000	0.0000	0.0000	0.0000
-8.61	0.0711	0.0356	0.0000	0.0000	0.0000	0.0000
-7.75	0.0866	0.0446	0.0000	0.0000	0.0000	0.0000
-6.89	0.1002	0.0467	0.0000	0.0000	0.0000	0.0000
-6.03	0.1210	0.0597	0.0000	0.0000	0.0001	0.0006

x/D = 64.7
Mole fraction data.

y/D	H_2O	$rmsH_2O$	H_2	$rmsH_2$	OH	rmsOH
-5.17	0.1464	0.0659	0.0000	0.0000	0.0003	0.0015
-4.31	0.1834	0.0827	0.0000	0.0007	0.0010	0.0035
-3.44	0.2303	0.0959	0.0001	0.0029	0.0024	0.0053
-2.58	0.2780	0.1020	0.0009	0.0078	0.0056	0.0079
-1.72	0.3363	0.1062	0.0029	0.0169	0.0114	0.0138
-0.86	0.3573	0.1100	0.0047	0.0217	0.0153	0.0169
0.00	0.3938	0.1134	0.0054	0.0238	0.0209	0.0185
0.86	0.3579	0.1043	0.0026	0.0164	0.0158	0.0147
1.72	0.3252	0.1012	0.0006	0.0070	0.0105	0.0118
2.58	0.2579	0.0942	0.0000	0.0011	0.0046	0.0089
3.44	0.2042	0.0804	0.0000	0.0010	0.0015	0.0049
4.31	0.1602	0.0615	0.0000	0.0000	0.0004	0.0026
5.17	0.1359	0.0512	0.0000	0.0000	0.0001	0.0006
6.03	0.1078	0.0427	0.0000	0.0000	0.0000	0.0003
6.89	0.0913	0.0353	0.0000	0.0000	0.0000	0.0002
7.75	0.0758	0.0321	0.0000	0.0000	0.0000	0.0000
8.61	0.0655	0.0279	0.0000	0.0000	0.0000	0.0000
9.47	0.0523	0.0222	0.0000	0.0000	0.0000	0.0000
10.33	0.0448	0.0171	0.0000	0.0000	0.0000	0.0000
11.19	0.0382	0.0153	0.0000	0.0000	0.0000	0.0000
12.05	0.0345	0.0142	0.0000	0.0000	0.0000	0.0000
12.92	0.0294	0.0113	0.0000	0.0000	0.0000	0.0000
13.78	0.0271	0.0110	0.0000	0.0000	0.0000	0.0000

x/D = 86.1
Mole fraction data.

y/D	f	rmsf	T	rmsT	O_2	$rmsO_2$	N_2	$rmsN_2$
-13.99	0.00000	0.00000	687.3	231.2	0.2075	0.0196	0.7488	0.0380
-12.92	0.00000	0.00000	765.9	229.4	0.2017	0.0198	0.7463	0.0390
-11.84	0.00000	0.00000	809.6	214.3	0.2000	0.0190	0.7433	0.0391
-10.76	0.00000	0.00000	888.3	209.5	0.1939	0.0206	0.7369	0.0410
-9.69	0.00000	0.00003	949.6	206.6	0.1890	0.0210	0.7330	0.0419
-8.61	0.00000	0.00000	1021.9	170.0	0.1822	0.0196	0.7252	0.0443
-7.53	0.00005	0.00048	1069.7	203.7	0.1774	0.0230	0.7175	0.0473
-6.46	0.00018	0.00108	1174.7	222.0	0.1663	0.0272	0.7054	0.0518
-5.38	0.00035	0.00144	1260.9	251.7	0.1568	0.0316	0.6922	0.0525

x/D = 86.1
Mole fraction data.

y/D	f	rmsf	T	rmsT	O_2	$rmsO_2$	N_2	$rmsN_2$
-4.31	0.00074	0.00214	1350.3	271.0	0.1460	0.0347	0.6818	0.0565
-3.23	0.00172	0.00352	1461.6	310.6	0.1316	0.0399	0.6621	0.0638
-2.15	0.00283	0.00417	1579.6	308.1	0.1169	0.0393	0.6448	0.0641
-1.08	0.00716	0.00520	1658.3	339.1	0.1092	0.0432	0.6423	0.0621
0.00	0.01140	0.00612	1653.8	337.4	0.1115	0.0408	0.6416	0.0621
1.08	0.00639	0.00481	1561.1	313.1	0.1240	0.0407	0.6497	0.0578
2.15	0.00134	0.00331	1470.0	300.6	0.1386	0.0389	0.6642	0.0591
3.23	0.00051	0.00164	1326.2	253.3	0.1551	0.0309	0.6783	0.0552
4.31	0.00012	0.00063	1243.5	229.6	0.1662	0.0263	0.6924	0.0525
5.38	0.00008	0.00057	1154.9	197.6	0.1759	0.0225	0.7043	0.0484
6.46	0.00001	0.00021	1080.7	197.5	0.1826	0.0213	0.7159	0.0459
7.53	0.00000	0.00000	1008.1	168.5	0.1893	0.0188	0.7269	0.0431
8.61	0.00000	0.00000	959.0	175.4	0.1925	0.0178	0.7348	0.0418
9.69	0.00000	0.00000	905.6	198.7	0.1959	0.0180	0.7411	0.0407
10.76	0.00000	0.00000	852.6	197.6	0.1980	0.0179	0.7465	0.0398
11.84	0.00000	0.00000	801.0	212.2	0.2020	0.0188	0.7488	0.0393
12.92	0.00000	0.00000	746.2	231.3	0.2000	0.0173	0.7575	0.0388
13.99	0.00000	0.00000	701.8	242.6	0.2021	0.0188	0.7596	0.0389

x/D = 86.1
Mole fraction data.

y/D	H_2O	$rmsH_2O$	H_2	$rmsH_2$	OH	rmsOH
-13.99	0.0417	0.0168	0.0000	0.0000	0.0000	0.0000
-12.92	0.0500	0.0219	0.0000	0.0000	0.0000	0.0000
-11.84	0.0548	0.0233	0.0000	0.0000	0.0000	0.0000
-10.76	0.0672	0.0311	0.0000	0.0000	0.0000	0.0001
-9.69	0.0760	0.0330	0.0000	0.0000	0.0000	0.0001
-8.61	0.0906	0.0378	0.0000	0.0000	0.0000	0.0002
-7.53	0.1030	0.0474	0.0000	0.0000	0.0002	0.0007
-6.46	0.1257	0.0569	0.0000	0.0000	0.0006	0.0022
-5.38	0.1478	0.0600	0.0000	0.0000	0.0012	0.0035
-4.31	0.1678	0.0682	0.0000	0.0000	0.0023	0.0046
-3.23	0.2005	0.0771	0.0000	0.0000	0.0038	0.0061
-2.15	0.2305	0.0762	0.0000	0.0000	0.0058	0.0072
-1.08	0.2392	0.0729	0.0001	0.0025	0.0072	0.0088
0.00	0.2376	0.0718	0.0000	0.0008	0.0072	0.0128

x/D = 86.1
Mole fraction data.

y/D	H$_2$O	rmsH$_2$O	H$_2$	rmsH$_2$	OH	rmsOH
1.08	0.2195	0.0687	0.0000	0.0000	0.0048	0.0067
2.15	0.1920	0.0721	0.0000	0.0000	0.0031	0.0058
3.23	0.1632	0.0633	0.0000	0.0000	0.0014	0.0035
4.31	0.1388	0.0547	0.0001	0.0013	0.0005	0.0017
5.38	0.1176	0.0478	0.0000	0.0000	0.0002	0.0008
6.46	0.0993	0.0424	0.0000	0.0000	0.0001	0.0007
7.53	0.0818	0.0356	0.0000	0.0000	0.0000	0.0001
8.61	0.0707	0.0292	0.0000	0.0000	0.0000	0.0001
9.69	0.0610	0.0264	0.0000	0.0000	0.0000	0.0002
10.76	0.0535	0.0216	0.0000	0.0000	0.0000	0.0000
11.84	0.0472	0.0184	0.0000	0.0000	0.0000	0.0000
12.92	0.0405	0.0165	0.0000	0.0000	0.0000	0.0000
13.99	0.0362	0.0156	0.0001	0.0020	0.0000	0.0004

REFERENCES

Alessandretti, G. C. and P. Violino, (1983), "Thermometry by CARS in an Automobile Engine," J. Phys. D: Appl. Phys., Vol. 16, pp. 1583-1594.

Alfa Products, (1988), Ultrapure n-Butyl Acetate (99+%), Purchased in 1988 from Alfa Products, 152 Andover St. Danvers, Mass., 01923.

Andresen, P., G. Meijer, H. Schluter, H. Voges, A. Koch, W. Hentschel, W. Oppermann, and E. Rothe, (1990), "Fluorescence Imaging Inside an Internal Combustion Engine Using Tunable Excimer Lasers," Applied Optics, Vol. 29, pp. 2392-2404.

Antcliff, R. R., O. Jarrett, Jr. R. C. Rogers, and T. VanOverbeck, (1986), "Multispecies CARS Measurements in Turbulent Combustion," Presented at the 23rd JANNAF Combustion Meeting, Hampton, Virginia.

Barlow, R. S., R. W. Dibble, and D. C. Fourguette, (1989), "Departure from Chemical Equilibrium in a Lifted Hydrogen Flame," AIAA Paper No. 89-2525.

Barlow, R. S., R. W. Dibble, J. Y. Chen, and R. P. Lucht, (1990), "Effect of Damköhler Number on Superequilibrium OH Concentration in Turbulent Nonpremixed Jet Flames," Combustion and Flame, Vol. 82, pp. 235-251.

Bass, A. M. and H. P. Broida, (1953), "A Spectrophotometric Atlas of the $^2\Sigma^+$-$^2\pi$ Transition of OH," National Bureau of Standard Circular 541.

Batchelor, G. K. (1959), "Small-scale Variation of Convected Quantities Like Temperature in Turbulent Fluid," J. Fluid Mech., Vol. 5, pp. 113-139.

Beach, Jr. H. L. (1972), "Supersonic Mixing and Combustion of a Hydrogen Jet in a Coaxial High-Temperature Test Gas," AIAA Paper No. 72-1179.

Becker, H. A. and D. Liang, (1978), "Visible Length of Vertical Free Turbulent Diffusion Flames," Combustion and Flame, Vol. 32, pp. 115-137.

Bedue, R., P. Gastebois, R. Bailly, M. Pealat, and J. P. Taran, (1984), "CARS Measurements in a Simulated Turbomachine Combustor," Combustion and Flame, Vol. 57, pp. 141-153.

Bilger, R. W. and R. E. Beck, (1975), "Further Experiments on Turbulent Jet Diffusion Flames," Fifteenth Symposium (International) on Combustion, The Combustion Institute, Pittsburgh, PA, pp. 541-552.

Bilger, R. W. (1982), "Molecular Transport Effects in Turbulent Diffusion Flames at Moderate Reynolds Number," AIAA Journal, Vol. 20, pp. 962-970.

Blackman, V. H. (1956), "Vibrational Relaxation in Oxygen and Nitrogen," J. Fluid Mech., Vol. 1, pp. 61-85.

Bowling, J. M. (1988), Temperature, Density, and Concentration in a Hydrogen-Air Flame by Excimer Induced Raman Scattering, Master Thesis, Vanderbilt University, Nashville, Tennessee.

Broadwell, J. E., W. J. A. Dahm, and M. G. Mungal, (1984), "Blowout of Turbulent Diffusion Flames," Twentieth Symposium (International) on Combustion, The Combustion Institute, Pittsburgh, PA, pp. 303-310.

Cattolica, R. J. (1982), "OH Radical Nonequilibrium in Methane-Air Flat Flames," Combustion and Flame, Vol. 44, pp. 43-59.

Center, R. E. and J. F. Newton, (1978), "Vibrational Relaxation of N_2 by H_2O," J. Chem. Phys., Vol. 68, pp. 3327-3333.

Chen, C. J. and W. Rodi, (1980), Vertical Turbulent Buoyant Jets, A Review of Experimental Data, Pergamon Press, New York.

Chen, J. Y. (1987), "Second-Order Conditional Modeling of Turbulent Nonpremixed Flames with a Composite PDF," Combustion and Flame, Vol. 69, pp. 1-36.

Chen, J. Y., F. C. Gouldin, and J. L. Lumley, (1987), "Second-Order Modeling of a Turbulent Nonpremixed H_2-Air Jet Flame with Intermittency and Conditional Averaging," Combustion Science and Technology, Vol. 53, pp. 235-257.

Chen, T. H. and L. P. Goss, (1989a), "Flame Lifting and Flame/Flow Interactions of Jet Diffusion Flames," AIAA Paper No. 89-0156.

Chen, T. H. and L. P. Goss, (1989b), "Propagation and Fractals of Turbulent Jet Diffusion Flames," AIAA Paper No. 89-2524.

Chen, T. H., L. P. Goss, D. Talley, and D. Mikolaitis, (1989), "Stabilization Zone Structure in Jet Diffusion Flames from Liftoff to Blowout," AIAA Paper No. 89-0153.

Chen, T. H. and L. P. Goss, (1990), "Characterization of Turbulent Jet Diffusion Flames: Results of Planar Imaging Techniques," AIAA Paper No. 90-0159.

Chen, T. H., D. D. Trump, and L. P. Goss, (1990), "Conditional Velocity Measurements at the Base of Turbulent, Lifted Jet Flames," AIAA Paper No. 90-2725.

Dibble, R. W., W. Kollmann, and R. W. Schefer, (1984), "Conserved Scalar Fluxes Measured in a Turbulent Nonpremixed Flame by Combined Laser Doppler Velocimetry and Laser Raman Scattering," Combustion and Flame, Vol. 55, pp. 307-321.

Dibble, R. W., A. R. Masri, and R. W. Bilger, (1987), "The Spontaneous Raman Scattering Technique Applied to Nonpremixed Flames of Methane," Combustion and Flame, Vol. 67, pp. 189-206.

Dieke, G. H. and H. M. Crosswhite, (1962), "The Ultraviolet Bands of OH Fundamental Data," J. Quant. Spectrosc. Radiat. Transfer, Vol. 2, pp. 97-199.

Drake, M. C., M. Lapp, C. M. Penney, S. Warshaw, and B. W. Gerhold, (1981), "Measurements of Temperature and Concentration Fluctuations in Turbulent Diffusion Flames Using Pulsed Raman Spectroscopy," Eighteenth Symposium (International) on Combustion, The Combustion Institute, Pittsburgh, PA, pp. 1521-1531.

Drake, M. C., R. W. Bilger, and S. H. Starner, (1982a), "Raman Measurements and Conserved Scalar Modeling in Turbulent Diffusion Flames," Nineteenth Symposium (International) on Combustion, The Combustion Institute, Pittsburgh, PA, pp. 459-467.

Drake, M. C., M. Lapp, and C. M. Penney, (1982b), "Use of the Vibrational Raman Effect for Gas Temperature Measurements," Temperature: Its Measurement and Control in Science and Industry, J. F. Schooley, ed., Vol. 5, New York: American Institute of Physics, pp. 631-638.

Drake, M. C., R. W. Pitz, M. Lapp, C. P. Fenimore, R. P. Lucht, D. W. Sweeney, and N. M. Laurendeau, (1984), "Measurements of Superequilibrium Hydroxyl Concentrations in Turbulent Nonpremixed Flames Using Saturated Fluorescence," Twentieth Symposium (International) on Combustion, The Combustion Institute, Pittsburgh, PA, pp. 327-335.

Drake, M. C., R. W. Pitz, and M. Lapp, (1986), "Laser Measurements on Nonpremixed H_2-Air Flames for Assessment of Turbulent Combustion

Models," AIAA Journal, Vol. 24, pp. 905-917.

Eckbreth, A. C., G. M. Dobbs, J. H. Stufflebeam, and P. A. Tellex, (1984), "CARS Temperature and Species Measurements in Augmented Jet Engine Exhausts," Applied Optics, Vol. 23, pp. 1328-1339.

Eckbreth, A. C. (1988), Laser Diagnostics for Combustion Temperature and Species, Energy and Engineering Science Series, A. K. Gupta and D. G. Lilley, ed., Vol. 7, Cambridge, Massachusetts, Abacus Press.

Eickhoff, H., B. Lenze, and W. Leuckel, (1984), "Experimental Investigation on the Stabilization Mechanism of Jet Diffusion Flames," Twentieth Symposium (International) on Combustion, The Combustion Institute, Pittsburgh, PA, pp. 311-318.

Ferri, A., P. A. Libby, and V. Zakkay, (1962), "Theoretical and Experimental Investigation of Supersonic Combustion," ARL 62-467, Aeronautical Research Laboratories; also Third ICAS Congress, Aug. 27-31, 1962, Stockholm, Sweden; also PIBAL Report 713, AD 291712, Sept. 1962, Polytechnic Inst. of Brooklyn.

Fletcher, D. G. and R. L. McKenzie, (1991), "Simultaneous Measurements of Temperature and Density in Air Flows Using UV Laser Spectroscopy," AIAA Paper No. 91-0458.

Garland, N. L. and D. R. Crosley, (1986), "On the Collisional Quenching of Electronically Excited OH, NH and CH in Flames," Twenty-first Symposium (International) on Combustion, The Combustion Institute, Pittsburgh, PA, pp. 1693-1702.

German, K. R., (1975), "Radiative and Predissociative Lifetimes of the $v' = 0, 1,$ and 2 Levels of the $A^2\Sigma^+$ State of OH and OD," The Journal of Chemical Physics, Vol. 63, pp. 5252-5255.

Glarborg, P., J. A. Miller, and R. J. Kee, (1986), "Kinetic Modeling and Sensitivity Analysis of Nitrogen Oxide Formation in Well-Stirred Reactor," Combustion and Flame, Vol. 65, pp. 177-202.

Goulard, R., A. M. Mellor, and R. W. Bilger, (1976), "Combustion Measurements in Air Breathing Propulsion Engines. Survey and Research Needs," Combustion Science and Technology, Vol. 14, pp. 195-219.

Gross, K. P. and R. L. McKenzie, (1985), "Measurement of Fluctuating Temperatures

in a Supersonic Turbulent Flow Using Laser-induced Fluorescence," AIAA Journal, Vol. 23, pp. 1932-1936.

Gutheil, E. and F. A. Williams, (1989), "Numerical and Asymptotic Investigation of Structures of Hydrogen-Air Diffusion Flames," Presented at the Fall Meeting of the Western States Section/The Combustion Institute, WSS/CI 89-109. Also, (1990), "A Numerical and Asymptotic Investigation of Structures of Hydrogen-Air Diffusion Flames at Pressures and Temperatures of High-Speed Combustion," Presented at Twenty-third Symposium (International) on Combustion, The Combustion Institute.

Hartfield, R. J., J. D. Abbitt, and J. C. McDaniel, (1989), "Injectant Mole Fraction Imaging in Compressible Mixing Flows Using Planar Laser-induced Iodine Fluorescence," Optics Letter, Vol. 14, pp. 850-852.

Herzberg, G. (1950), Molecular Spectra and Molecular Structure - Part I: Spectra of Diatomic Molecules, 2nd ed., D. Van Nostrand Company, Inc., Princeton, New Jersey, Chapter 2, Section 2(e) and 2(f).

Hillard, M. E. Jr., W. W. Hunter, Jr., J. F. Meyers, and W. V. Feller, (1975), "Simultaneous Raman and Laser Velocimeter Measurements," AIAA J., Vol. 12, pp. 1445-1447.

Hiller, B. and R. K. Hanson, (1988), "Simultaneous Planar Measurements of Velocity and Pressure Fields in Gas Flows Using Laser-induced Fluorescence," Applied Optics, Vol. 27, pp. 33-48.

Janicka, J. and W. Kollmann, (1979), "A Two-Variable Formalism for the Treatment of Chemical Reactions in Turbulent H_2-Air Diffusion Flames," Seventeenth Symposium (International) on Combustion, The Combustion Institute, Pittsburgh, PA, pp. 421-430.

Jarrett, Jr. O., A. D. Cutler, R. R. Antcliff, T. Chitsomboon, C. L. Dancy, and J. A. Wang, (1988), "Measurements of Temperature, Density, and Velocity in Supersonic Reacting Flow for CFD Code Validation," Presented at the 25th JANNAF Combustion Meeting, Huntsville, Alabama.

Jarrett, Jr. O., (1990), Private Communication.

Kalghatgi, G. T. (1984), "Lift-off Heights and Visible Lengths of Vertical Turbulent Jet Diffusion Flames in Still Air," Combustion Science and Technology, Vol. 41, pp. 17-29.

Kee, R. J., J. A. Miller, and T. H. Jefferson, (1980), "CHEMKIN: A General Purpose Problem-Independent Transportable, Fortran Chemical Kinetics Code Package," Sandia Report, SAND 80-8003.

Kobayashi, T., M. Konishi, M. Ohtaka, S. Taki, M. Ueda, K. Kagawa, and H. Inaba, (1987), "Application of UV and VUV Excimer Lasers in Combustion Measurements Using Enhanced Raman Scattering," Laser Diagnostics and Modeling of Combustion, K. Iinumu, T. Asanuma, T. Ohsawa, and J. Doi, ed., Springer-Verlag, Berlin, pp. 133-140.

Kolmogorov, A. N. (1941), "Local Structure of Turbulence in an Incompressible Viscous Fluid at Very High Reynolds Numbers," Dokl. Akad. Nauk SSSR, Vol. 30, p. 299. Reprinted in: Usp. Fiz. Nauk, Vol. 93, pp. 476-481, (1967). Translated into English in: Sov. Phys. Usp., Vol. 10, pp. 734-736. (1968).

Kozlov, P. V., S. A. Losev, and V. A. Pavlov, (1987), "Determination of the Vibrational Relaxation time of Nitrogen in a Shock Wave by Coherent anti-Stokes Raman Spectroscopy," Sov. Phys. Tech. Phys., Vol. 32, pp. 1235-1237.

Kurian, J. and A. K. Sreekanth, (1987), "Laser Schlieren Study of Vibrational Relaxation of N_2 by H_2O," Chemical Physics, Vol. 114, pp. 295-303.

Lapp, M., C. M. Penney, and J. A. Asher, (1973), "Application of Light Scattering Techniques for Measurements of Density, Temperature, and Velocity in Gasdynamics," General Electric Co. Schenectady, New York, NTIS, AD-759575.

Lapp, M., M. C. Drake, C. M. Penney, R. W. Pitz, and S. Correa, (1983), "Turbulent Combustion Experiments and Modeling," General Electric Co. Schenectady, New York, NTIS, DE84-002806.

Larsen, R. J. and M. L. Marx, (1986), An Introduction to Mathematical Statistics and Its Applications, 2nd ed. Prentice-Hall, Englewood Cliffs, New Jersey 07632. p. 175, 199.

Laufer, G. and R. L. McKenzie, (1988), "Temperature Measurements in Hypersonic Air Flows Using Laser-induced O_2 Fluorescence," AIAA Paper No. 88-4679.

Laurendeau, N. M. (1988), "Temperature Measurements by Light Scattering Method," J. Prog. Energy Comb. Sci., Vol. 14, p. 147.

Lederman, S. (1974), "The Use of Laser Raman Diagnostics in Flow Fields and Combustion," J. Prog. Energy Comb. Sci., Vol. 3, pp. 1-34.

Lezberg, E. A. and L. C. Franciscus, (1963), "Effects of Exhaust Nozzle Recombination on Hypersonic Ramjet Performance: I. Experimental Measurements," AIAA Journal, Vol. 1, pp. 2071-2076.

Long, M. B., D. C. Fourguette, M. C. Escoda, (1983), "Instantaneous Ramanography of a Turbulent Diffusion Flame," Optics Letter, Vol. 8, pp. 244-246.

Magre, P. and R. W. Dibble, (1988), "Finite Chemical Kinetic Effects in a Subsonic Turbulent Hydrogen Flame," Combustion and Flame, Vol. 73, pp. 195-206.

Mansour, M. S., R. W. Bilger, and R. W. Dibble, (1990), "Spatial-Averaging Effects in Raman/Rayleigh Measurements in a Turbulent Flame," Combustion and Flame, Vol. 82, pp. 411-425.

Masri, A. R., R. W. Bilger, and R. W. Dibble, (1987a), "Fluorescence Interference with Raman Measurements in Nonpremixed Flames of Methane," Combustion and Flame, Vol. 68, pp. 109-119.

Masri, A. R., R. W. Bilger, and R. W. Dibble, (1987b), "Turbulent Nonpremixed Flames of Methane near Extinction: Mean Structure from Raman Measurements," Combustion and Flame, Vol. 71, pp. 245-266.

Masri, A. R., R. W. Bilger, and R. W. Dibble, (1987c), "Turbulent Nonpremixed Flames of Methane near Extinction: Probability Density Functions," Combustion and Flame, Vol. 73, pp. 261-285.

Miake-Lye, R. C. and J. A. Hammer, (1988), "Lifted Turbulent Jet Flames: A Stability Criterion Based on the Jet Large-Scale Structure," Twenty-second Symposium (International) on Combustion, The Combustion Institute, Pittsburgh, PA, pp. 817-824.

Miles, R., C. Cohen, J. Connors, P. Howard, S. Huang, E. Markovitz, and G. Russell, (1987), "Velocity Measurements by Vibrational Tagging and Fluorescent Probing of Oxygen," Optics Letter, Vol. 12, pp. 861-863.

Miller, P. L. and P. E. Dimotakis, (1991), "Stochastic Geometric Properties of Scalar Interfaces in Turbulent Jets," Phys. Fluids A: American Institute of Phys., Vol. 3, pp. 168-177.

Mungal, M. G. and C. E. Frieler, (1988), " The Effects of Damköhler Number in a Turbulent Shear layer," Combustion and Flame, Vol. 71, pp. 23-34.

Northam, G. B. and G. Y. Anderson, (1986), "Supersonic Combustion Ramjet

Research at Langley," AIAA Paper No. 86-0159.

Paul, P. H., M. P. Lee, and R. K. Hanson, (1989), "Molecular Velocity Imaging of Supersonic Flows Using Pulsed Planar Laser-induced Fluorescence of NO," Optics Letter, Vol. 14, pp. 417-419.

Peters, N. and F. A. Williams, (1983), "Liftoff Characteristics of Turbulent Jet Diffusion Flames," AIAA Journal, Vol. 21, pp. 423-429.

Peters, N. (1984), "Partially Premixed Diffusion Flamelets in Non-Premixed Turbulent Combustion," Twentieth Symposium (International) on Combustion, The Combustion Institute, Pittsburgh, PA, pp. 353-360.

Pitts, W. M. (1988), "Assessment of Theories for the Behavior and Blowout of Lifted Turbulent Jet Diffusion Flames," Twenty-second Symposium (International) on Combustion, The Combustion Institute, Pittsburgh, PA, pp. 809-816.

Pitts, W. M. (1989), "Importance of Isothermal Mixing Processes to the Understanding of Lift-Off and Blowout of Turbulent Jet Diffusion Flames," Combustion and Flame, Vol. 76, pp. 197-212.

Pitz, R. W. and M. C. Drake, (1986), "Intermittency and Conditional Averaging in a Turbulent Nonpremixed Flame by Raman Scattering," AIAA Journal, Vol. 24, pp. 815-822.

Pitz, R. W., J. A. Wehrmeyer, J. M. Bowling, and T. S. Cheng, (1990), "Single Pulse Vibrational Raman Scattering by a Broadband KrF Excimer Laser in a Hydrogen-Air Flame," Applied Optics, Vol. 29, pp. 2325-2332.

Placzek, G and E. Teller, (1933), Z. Physik, Vol. 81, p. 209.

Reynolds, W. C. (1986), "The Element Potential Method for Chemical Equilibrium Analysis: Implementation in the Interactive Program STANJAN," Department of Mechanical Engineering, Stanford University.

Schefer, R. W. and R. W. Dibble, (1985), "Simultaneous Measurements of Velocity and Density in a Turbulent Nonpremixed Flame," AIAA J., Vol. 23, pp. 1070-1078.

Schefer R. W., M. Namazian and J. Kelly, (1988), "Structural Characteristics of Lifted Turbulent-Jet Flames," Twenty-second Symposium (International) on Combustion, The Combustion Institute, Pittsburgh, PA, pp. 833-842.

Scholefield, D. A. and J. E. Garside, (1949), "The Structure and Stability of Diffusion Flames," Third Symposium on Combustion, Flame, and Explosion Phenomena, The Williams and Wilkins Company, Baltimore, Maryland, pp. 102-110.

Sciopt Enterprises, (1988), OPTEC II/87 PC Program, Purchased in 1989 from Sciopt Enterprises, P. O. Box 20637, San Jose, CA 95160.

Sink M. L. and A. D. Bandrauk, (1980), "Theoretical Analysis of the Predissociation of the $A^2\Sigma^+$ State of OH," J. Chem. Phys., Vol. 73, pp. 4451-4459.

Starner, S. H. and R. W. Bilger, (1980), "LDA Measurements in a Turbulent Diffusion Flames," Combustion Science and Technology, Vol. 21, pp. 259-276.

Vanquickenborne, L. and A. van Tiggelen, (1966) "The Stabilization Mechanism of Lifted Diffusion Flames," Combustion and Flame, Vol. 10, pp. 59-69.

Villasenor, R., J. Y. Chen, and R. W. Pitz, (1990), "Modeling Ideally Expanded Supersonic Turbulent Jet Flows with Nonpremixed H_2-Air Combustion," AIAA Paper No. 90-0640.

Villasenor, R., J. Y. Chen, and R. W. Pitz, (1991), "Interaction Between Chemical Reaction and Turbulence in Supersonic Nonpremixed H_2-Air Combustion," AIAA Paper No. 91-0375.

Wang, C. C. and L. I. Davis, (1974), "Measurement of Hydroxyl Concentrations in Air Using a Tunable uv Laser Beam," Phys. Rev. Lett., Vol. 32, p. 349.

Wehrmeyer, J. A. (1990), UV Raman Scattering for Flame Diagnostics Using a KrF Excimer Laser, Ph.D. Thesis, Vanderbilt University, Nashville, Tennessee.

REPORT DOCUMENTATION PAGE

Public reporting burden for this collection of information is estimated to average 1 hour per response, including the time for reviewing instructions, searching existing data sources, gathering and maintaining the data needed, and completing and reviewing the collection of information. Send comments regarding this burden estimate or any other aspect of this collection of information, including suggestions for reducing this burden, to Washington Headquarters Services, Directorate for Information Operations and Reports, 1215 Jefferson Davis Highway, Suite 1204, Arlington, VA 22202-4302, and to the Office of Management and Budget, Paperwork Reduction Project (0704-0188), Washington, DC 20503.

1. AGENCY USE ONLY (Leave blank)	2. REPORT DATE	3. REPORT TYPE AND DATES COVERED
	December 1991	Contractor Report

4. TITLE AND SUBTITLE

Laser Raman Diagnostics in Subsonic and Supersonic Turbulent Jet Diffusion Flames

5. FUNDING NUMBERS

G NAG1-770

WU 505-62-40-01

6. AUTHOR(S)

T. S. Cheng

J. A. Wehrmeyer
R. W. Pitz

7. PERFORMING ORGANIZATION NAME(S) AND ADDRESS(ES)

Vanderbilt University
Department of Mechanical Engineering
Nashville, TN 37235

8. PERFORMING ORGANIZATION REPORT NUMBER

9. SPONSORING/MONITORING AGENCY NAME(S) AND ADDRESS(ES)

NASA Langley Research Center
Hampton, VA 23665-5225

10. SPONSORING/MONITORING AGENCY REPORT NUMBER

NASA CR-189544

11. SUPPLEMENTARY NOTES
Langley
Technical Monitor - G. Burton Northam
Dr. T. S. Cheng Thesis Research

Data Files stored at Langley
Jarrett - Directory
Pitz - SubDirectory

12a. DISTRIBUTION/AVAILABILITY STATEMENT

Unclassified - Unlimited

Subject Category 12

12b. DISTRIBUTION CODE

13. ABSTRACT (Maximum 200 words)

UV spontaneous vibrational Raman scattering combined with laser-induced pre-dissociative fluorescence (LIPF) is developed for temperature and multi-species concentration measurements. Simultaneous measurements of temperature, major species (H_2, O_2, N_2, H_2O), and minor species (OH) concentrations are made with a "single" narrowband KrF excimer laser in subsonic and supersonic lifted turbulent hydrogen-air diffusion flames.

The UV Raman system was calibrated with a flat-flame diffusion burner operated at several known equivalence ratios. Temperature mensurements made by the ratio of Stokes/anti-Stokes signal.

14. SUBJECT TERMS
Raman Scattering
Subsonic Combustion
Supersonic Combustion

CFD Validation

15. NUMBER OF PAGES
191

16. PRICE CODE
A09

17. SECURITY CLASSIFICATION OF REPORT	18. SECURITY CLASSIFICATION OF THIS PAGE	19. SECURITY CLASSIFICATION OF ABSTRACT	20. LIMITATION OF ABSTRACT
Unclassified	Unclassified		